Cell-type specific cholinergic modulation of the cortex

by

Naiyan Chen

B.Eng., Biomedical Engineering, Imperial College London (2006)

SUBMITTED TO THE COMPUTATIONAL AND SYSTEMS BIOLOGY PROGRAM IN PARTIAL FULFILLMENT OF THE REQUIREMENTS FOR THE DEGREE OF DOCTORATE OF PHILOSOPHY IN COMPUTATIONAL AND SYSTEMS BIOLOGY AT THE MASSACHUSETTS INSTITUTE OF TECHNOLOGY

SEPTEMBER 2013

Author .....

Naiyan Chen
Computational and Systems Biology Program
July 29 2013

Certified by .....

Mriganka Sur, PhD
Paul E. Newton Professor of Neuroscience
Thesis Supervisor

Accepted by.....

Christopher B. Burge, PhD
Professor of Biology and Biological Engineering
Director, Computational and Systems Biology Graduate Program

Cell-type specific cholinergic modulation of the cortex

by

Naiyan Chen

SUBMITTED TO THE COMPUTATIONAL AND SYSTEMS BIOLOGY PROGRAM
IN PARTIAL FULFILLMENT OF THE REQUIREMENTS FOR THE DEGREE OF
DOCTORATE OF PHILOSOPHY IN COMPUTATIONAL AND SYSTEMS BIOLOGY
AT THE MASSACHUSETTS INSTITUTE OF TECHNOLOGY

SEPTEMBER 2013

Abstract

The cholinergic innervation of the neocortex by afferent fibers originating in the nucleus basalis (NB) of the basal forebrain is implicated in modulating diverse neocortical functions including information processing, cortical plasticity, arousal and attention. To understand the physiological basis of these brain functions during cholinergic modulation, it is critical to identify the cortical circuit elements involved and define how their interactions contribute to cortical network dynamics. In this thesis, I present evidence showing how specific neuronal and glial cell types can be differentially modulated by acetylcholine (Ach), resulting in dynamic functional interactions during ACh-modulated information processing and cortical plasticity. Chapter 2 identifies somatostatin-expressing neurons as a dominant player in driving decorrelation and information processing through its intimate interactions with parvalbumin-expressing and pyramidal neurons. Chapter 3 highlights astrocytes and their interactions with pyramidal neurons as important drives for stimulus-specific cortical plasticity during cholinergic modulation. This is one of the earliest works that has mapped the functional role of distinct cell-types and their interactions to specific brain functions modulated by ACh, thereby setting the foundation for future studies to manipulate these specific functional interactions in both normal and diseased brains.

Thesis Supervisor: Mriganka Sur, PhD
Title: Paul E. Newton Professor of Neuroscience

Thesis Committee:
Guoping Feng, PhD, Mehmet Fatih Yanik, PhD, Peter So, PhD, Philip Haydon, PhD

Acknowledgements

*Mama, for her loving support, encouragement, understanding and unwavering belief that kept me going during the darkest days. This would not have been possible without her. Papa, for being the first to teach me math and science and for planting the seed of knowledge in me. My brother, Naizhen for engaging me intellectually. Dr. Martyn Boutelle, Dr. Mauricio Barahona and especially Prof. John Lever, my dearest teachers at Imperial College for going out of their way to support my graduate school dream. My friends, Shaoying, Cathelline, Agnes, Beijia, Lumine+Oliver, Lek, Yifeng, Prasit, Shireen, Yoong Keok, Mornin+Bingjie, Raga, Manzhi, Claus, Geoffrey, Juanjuan, Liz, Ikue for all the lovely adventures. CSBi 2007 classmates, Yuanyuan, Michelle, Albert, Tracy and Jonathan for walking the grad school journey together. Dr. Bruce Tidor and Dr. Chris Burge, Darlene Ray, Bonnie Whang and Jacqueline Carota for the great CSBi vision and administrative support. Members of Sur lab, especially Sami El Boustani, Caroline Runyan, Michael Goard, Travis Emery, Chuong Le, Jorge Castro, Eleana Ricci, Jonathan Woodson and Vardhan Dani. I will also like to specially thank Jitendra Sharma for his kind encouragement and for the insightful discussion on planning my scientific career. My thesis committee, Dr. Guoping Feng for sharing his invaluable advice and insights on the scientific career, Dr. Peter So and Dr. Fatih Yanik for making themselves available for scientific discussions. Dr. Philip Haydon for his invaluable presence at my thesis defense. Dr. Ed Boyden, Dr. Ken McCarthy, Dr. Aimei Yang, Holly Robertson, Dr. Abhishek Banerjee, Dr. Jeremy Petravicz for sharing resources for my thesis work. The Singapore A*STAR National Science Graduate Fellowship for their generous funding.*

There are two scientists who have been instrumental in my scientific growth. My immense gratitude to Hiroki Sugihara, whose intellect, patience, positivity, curious mind, tireless persistence and camaraderie made the acetylcholine journey an unforgettable experience. My neuroscience efforts will not have been possible without my advisor, Mriganka Sur whose open-mindedness, intelligence, creativity, unwaning enthusiasm, optimism and support have been a great source of motivation for my graduate studies.

Table of Contents

Chapter 1: Introduction

Our conscious experience is one of the most familiar yet also most mysterious aspect of our lives (*1*). Philosophers and theologists have attempted to comprehend the nature of consciousness since the 1500s. Their understanding is further extended in the 1970s by psychologists and neuroscientists who have characterized consciousness as arousal, vigilance, mental experience and selective attention. More recently, it has been further elucidated that these behavioral correlates of our conscious experience can be driven and modulated by the cholinergic system in our brains (2). Specifically, the cholinergic innervation of the neocortex by afferent fibers originating in the nucleus basalis (NB) of the basal forebrain (3) was found to be implicated in the modulation of diverse functions spanning consciousness and learning, including arousal (4), attention (5), information processing (6) and cortical plasticity (7, 8).

It is well known that the NB neurons can alter their activity (*9*) in a task- and stimulus-dependent manner to release acetylcholine (ACh) to the cortex across multiple timescales (*10*). It is however unclear how the released ACh can modulate rapid and dynamic changes in task demands and inputs across different brain functions. Despite increasing *ex vivo* immunohistochemistry, pharmacological and electrophysiological evidence of multiple cell types being activated by ACh in distinct species and brain regions, several questions still remain unresolved: What are the cortical cell-types involved and how do they interact during cholinergic

modulation *in vivo*? Are the roles of ACh-responsive cell-types and their functional interactions preserved across different brain functions? If not, how do their roles and functional dynamics change? This thesis attempts to address these questions by focusing on two functions found implicated in cholinergic modulation: information processing and cortical plasticity. The experiments in this thesis employ the use of transgenic mice that allow targeted recording of genetically defined cell classes both *in vivo* and *ex vivo* using both calcium imaging and electrophysiology. A combination of optogenetics, pharmacology and knockout mice approaches was also used to dissect the functional interactions among the distinct cell classes.

Chapter one provides an overview on what has been known about the organization of the basal forebrain cholinergic system, properties of ACh and its receptors as well as that of cholinergic modulation of information processing, plasticity and of different cell types. A description of the visual pathway, used as a model system in my thesis, is also included. Chapter two lays out evidence on how a specific inhibitory microcircuit that is differentially modulated by ACh can enhance information processing and alter brain states in the visual cortex. Chapter three describes how cholinergic activation of a special subtype of glial cell known as astrocytes and their interactions with excitatory neurons can surprisingly play a dominant role in driving stimulus-specific plasticity in the visual cortex. Chapter four offers concluding thoughts on the implications of a functional circuit that dynamically changes across different cholinergic modulated brain functions.

1.1. Organization of the basal forebrain cholinergic system

Two major groups of cholinergic neurons exist and they lie in the basal forebrain and brainstem. The basal forebrain cholinergic group is located within the medial septal nucleus, vertical and horizontal limb nuclei of the diagonal band of Broca as well as the nucleus basalis (NB) magnocellularies (also known as nucleus basalis of Meynert). On the other hand, the brain stem cholinergic group is found in the pedunculopontine tegmental nucleus and the laterodorsal pontine tegmentum. The basal cholinergic neurons innervate the neocortex, cingulate cortex, hippocampus, basolateral amygdala and olfactory bulb while those in the brainstem innervate mainly the thalamus (*11*).

In this thesis, we focus on the visual cortex as a model system where majority of the cholinergic projections it receives originate from the NB (**Fig. 1**). The distribution of the cholinergic axons in the neocortex has been known to be diffuse (*12, 13*) and vary in density across the cortical layers (*14-17*). Cholinergic neurotransmission is traditionally believed to be volumetric where ACh spills into the extracellular space to stimulate distant extrasynaptic cholinergic receptors. Recent evidence however contradicts the volume transmission hypothesis by suggesting that wired transmission through classical synapses can also exist (*18*). In addition, contrary to the traditional belief that ACh release is tonic and slow-changing, there has been increasing evidence that seem to support phasic ACh signaling where transient release of ACh at the time scale of seconds can occur in attentional tasks (*10, 18-20*).

1.2. Properties of acetylcholine and its receptors

ACh binds to two classes of receptors: metabotropic muscarinic receptors (mAChRs) and ionotropic nicotinic receptors (nAChRs) (*21*), named based on their differential sensitivity to muscarine and nicotine.

The mAChRs can be further subdivided into five different subtypes (*22*) where M_1, M_3, M_5 activation is characterized by phosphatidyl inositol hydrolysis through G-proteins-mediated activation of phospholipase while M_2 and M_4 activation leads to inhibition of adenylyl cyclase activity via G protein G_i or G_o. Distributions of M_1- M_5 are inhomogeneous across species, brain regions, layers (*23-27*) and in subcellular structures (*28*).

The nAChRs are composed of ligand binding subunits ($\alpha2 - \alpha8$) and structural subunits ($\beta2 - \beta4$) (*29*). Multiple combinations can create a diversity of receptor subtypes with different physiological functions. The subtypes can also be classified based on their sensitivity to the toxin α-bungarotoxin where high and low affinity nAChRs are α-bungarotoxin-insensitive and sensitive respectively (*30*). High and low affinity nAChRs are dense in middle cortical layers and cortical layers I and VI respectively (*31*). nAChRs have been found to occur in pyramidal, spiny stellate cells and inhibitory neurons, sometimes with co-expression of mAChRs (*32*).

1.3. Cholinergic modulation of information processing

A wealth of studies using NB lesion, NB electrical stimulation and pharmacology have presented rich evidence in support of cholinergic modulation in the detection, selection and processing of stimuli, particularly during attention.

Some of the earliest revealing evidence on the role of ACh in information processing came from NB lesion studies. In these studies, selective excitotoxic lesions of the NB neurons were performed by injecting excitatory amino acid agonists or immunotoxin into the NB (*33*). Animals with their NB neurons impaired by this method showed reduced attentional functions (*34-38*) and stimulus processing abilities (*39*) as reflected by lower accuracy and longer latencies in their response to attentional tasks. Pharmacological studies using cholinergic receptor agonists and antagonists as well as with cholinesterase inhibitors to enhance or suppress cholinergic action have provided further understanding at the biochemistry level. Particularly, researchers have demonstrated that both nicotinic and muscarinic receptors can mediate the change in performance during cholinergic modulation of sensory processing (*40-43*) and attentional (*5, 44-46*) tasks.

The advent of single/multi- unit recording allows unprecedented understanding of cholinergic modulation of information processing at a single neuronal level. These studies typically involve recording of the spike responses of a population of single units before, during and after local iontophoretic application of ACh or electrical stimulation of the NB. These studies have shown

that cholinergic modulation can affect contrast gain (*47*), orientation and direction selectivity (*5, 48-51*), spatial integration (*52*), receptive field size (*53, 54*) and attention (*5*).

More recently, similar studies performed with more elegant analysis has also revealed that ACh can enhance information processing through interneuronal decorrelation (*6, 55*), particularly during execution of attentional tasks (*56, 57*).

1.4. Cholinergic modulation of brain states

Several studies have shown that the cholinergic system can control cortical states. Cholinergic output in the cortex have been observed to co-vary with brain state changes (*58*) while increased NB neuronal firing have been found to occur during cortical desynchronization (*59, 60*). The causal relationship between the cholinergic system and cortical states are further established in the following studies: Lesions of the NB leads to increased low-frequency local field potential power (*61*) while electrical and optogenetic stimulation of the basal forebrain or cholinergic projections to the cortex induces mAChR-mediated cortical desynchronization (*9, 62*). This ACh-induced desynchronization is similar to that observed during normal physiological changes such as that observed during tail pinch of animals (*62*).

1.5. Cholinergic modulation of plasticity

One of the earliest studies that show that ACh can induce long-lasting changes in the excitability of neurons is performed by pairing ACh iontophoresis with intracellular depolarization of cortical neurons in awake cats (*63*). A subsequent study shows that co-application of ACh or muscarinic agonists with glutamate can induce a prolonged increase in response to glutamate in somatosensory cortical neurons (*64, 65*).

When the application of ACh or NB electrical stimulation is paired with sensory stimulation in the somatosensory (*64, 66-71*) and auditory cortex (*53, 54, 72-75*), prolonged changes in responses are also observed. It is shown in these studies that cholinergic antagonists cannot reverse the prolonged changes, thereby confirming that the induction but not maintenance of prolonged changes require ACh (*67*). It is worth mentioning that the cortical plasticity can occur at both single cell and cortical map levels (*8, 53, 54, 76, 77*).

1.6. Cholinergic modulation of distinct cell types

Multiple cortical cell types have been found to be responsive to ACh. These cells have complex functional interactions as supported by observations of both hyperpolarizing and depolarizing responses in excitatory (*78-81*) and different subtypes of inhibitory neurons (*81-83*) across distinct neocortical layers in multiple species. A recent study also reveals that ACh can elicit facilitatory and suppressive responses in non fast-spiking (FS) and FS cortical interneurons

respectively(*81*). In the hippocampus, the circuitry of cholinergic modulation also include astrocytes (*84, 85*), which have been discovered to be ACh-responsive (*86-88*).

The functional interactions between these ACh-responsive cortical cell types and how they contribute to the ACh-modulated brain functions remain to be investigated.

1.7. Model system

The visual pathway in mice is used as a model system in my thesis work (**Fig. 2**). Visual responses in the primary visual cortex are evoked by presentation of visual stimuli to the eyes of anesthetized mice. The cholinergic projections from the nucleus basalis are stimulated to induce acetylcholine release to the visual cortex, where visual responses are recorded before and after cholinergic stimulation.

1.8. Figures

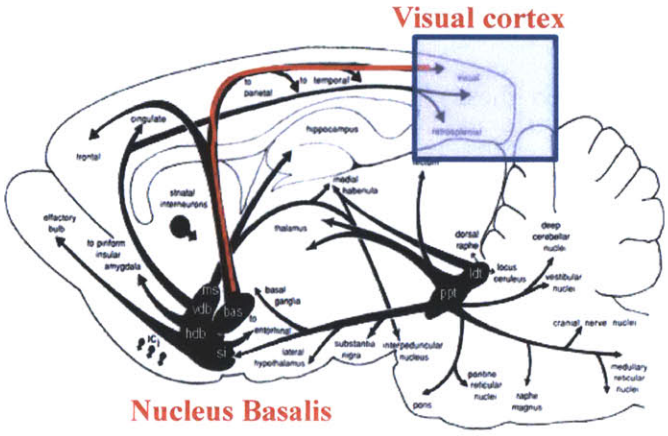

Fig. 1. Schematic showing the afferent cholinergic projection (red line) from the nucleus basalis to visual cortex (*11*).

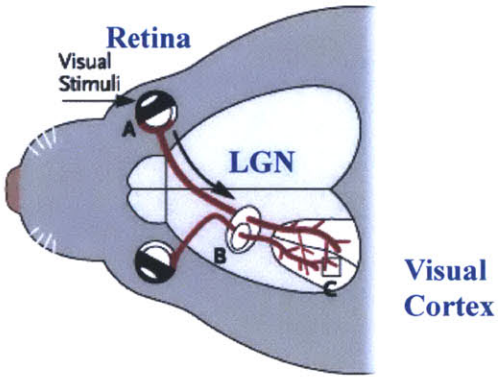

Fig. 2. Schematic showing the visual pathway in mice

1.9. References

1. M. Velmans, S. Schneider, *The Blackwell companion to consciousness.* (Wiley-Blackwell, 2008).
2. E. Perry, M. Walker, J. Grace, R. Perry, Acetylcholine in mind: a neurotransmitter correlate of consciousness? *Trends in Neurosciences* 22, 273 (1999).
3. C. A. Kitt, C. Höhmann, J. T. Coyle, D. L. Price, Cholinergic innervation of mouse forebrain structures. *The Journal of Comparative Neurology* 341, 117 (1994).
4. J. W. Phillis, Acetylcholine release from the cerebral cortex: Its role in cortical arousal. *Brain Research* 7, 378 (1968).
5. J. L. Herrero *et al.*, Acetylcholine contributes through muscarinic receptors to attentional modulation in V1. *Nature* 454, 1110 (2008).
6. M. Goard, Y. Dan, Basal forebrain activation enhances cortical coding of natural scenes. *Nat Neurosci* 12, 1444 (2009).
7. M. F. Bear, W. Singer, Modulation of visual cortical plasticity by acetylcholine and noradrenaline. *Nature* 320, 172 (1986).
8. R. C. Froemke, M. M. Merzenich, C. E. Schreiner, A synaptic memory trace for cortical receptive field plasticity. *Nature* 450, 425 (2007).
9. R. Metherate, C. Cox, J. Ashe, Cellular bases of neocortical activation: modulation of neural oscillations by the nucleus basalis and endogenous acetylcholine. *The Journal of Neuroscience* 12, 4701 (1992).
10. V. Parikh, R. Kozak, V. Martinez, M. Sarter, Prefrontal acetylcholine release controls cue detection on multiple timescales. *Neuron* 56, 141 (2007).
11. B. J. Everitt, T. W. Robbins, Central cholinergic systems and cognition. *Annual review of psychology* 48, 649 (1997).
12. D. Rye, B. Wainer, M. Mesulam, E. Mufson, C. Saper, Cortical projections arising from the basal forebrain: a study of cholinergic and noncholinergic components employing combined retrograde tracing and immunohistochemical localization of choline acetyltransferase. *Neuroscience* 13, 627 (1984).
13. F. Eckenstein, R. Baughman, J. Quinn, An anatomical study of cholinergic innervation in rat cerebral cortex. *Neuroscience* 25, 457 (1988).
14. A. Lysakowski, B. Wainer, G. Bruce, L. Hersh, An atlas of the regional and laminar distribution of choline acetyltransferase immunoreactivity in rat cerebral cortex. *Neuroscience* 28, 291 (1989).
15. K. Satoh, D. Armstrong, H. Fibiger, A comparison of the distribution of central cholinergic neurons as demonstrated by acetylcholinesterase pharmacohistochemistry and choline acetyltransferase immunohistochemistry. *Brain research bulletin* 11, 693 (1983).
16. M. Mesulam, L. B. Hersh, D. C. Mash, C. Geula, Differential cholinergic innervation within functional subdivisions of the human cerebral cortex: a choline acetyltransferase study. *Journal of Comparative Neurology* 318, 316 (1992).
17. M. A. Raghanti *et al.*, Cholinergic innervation of the frontal cortex: differences among humans, chimpanzees, and macaque monkeys. *Journal of Comparative Neurology* 506, 409 (2008).
18. M. Sarter, V. Parikh, W. M. Howe, Phasic acetylcholine release and the volume transmission hypothesis: time to move on. *Nature Reviews Neuroscience* 10, 383 (2009).
19. V. Parikh, M. Sarter, Cholinergic Mediation of Attention. *Annals of the New York Academy of Sciences* 1129, 225 (2008).

20. V. Parikh, K. Man, M. W. Decker, M. Sarter, Glutamatergic contributions to nicotinic acetylcholine receptor agonist-evoked cholinergic transients in the prefrontal cortex. *The Journal of Neuroscience* 28, 3769 (2008).
21. J. R. Cooper, F. E. Bloom, R. H. Roth, *The biochemical basis of neuropharmacology*. (Oxford University Press, USA, 2003).
22. T. I. Bonner, N. Buckley, A. Young, M. Brann, Identification of a family of muscarinic acetylcholine receptor genes. *Science* 237, 527 (1987).
23. N. Buckley, T. Bonner, M. Brann, Localization of a family of muscarinic receptor mRNAs in rat brain. *The Journal of Neuroscience* 8, 4646 (December 1, 1988, 1988).
24. M. S. Lidow, D. W. Gallager, P. Rakic, P. S. Goldman-Rakic, Regional differences in the distribution of muscarinic cholinergic receptors in the macaque cerebral cortex. *Journal of Comparative Neurology* 289, 247 (1989).
25. R. Schliebs, C. Walch, M. Stewart, Laminar pattern of cholinergic and adrenergic receptors in rat visual cortex using quantitative receptor autoradiography. *Journal für Hirnforschung* 30, 303 (1989).
26. K. Zilles *et al.*, in *Central Cholinergic Synaptic Transmission*. (Springer, 1989), pp. 212-228.
27. G. Prusky, M. Cynader, The distribution of M< sub> 1</sub> and M< sub> 2</sub> muscarinic acetylcholine receptor subtypes in the developing cat visual cortex. *Developmental Brain Research* 56, 1 (1990).
28. L. Mrzljak, A. I. Levey, P. S. Goldman-Rakic, Association of m1 and m2 muscarinic receptor proteins with asymmetric synapses in the primate cerebral cortex: morphological evidence for cholinergic modulation of excitatory neurotransmission. *Proceedings of the National Academy of Sciences* 90, 5194 (1993).
29. P. B. Sargent, The diversity of neuronal nicotinic acetylcholine receptors. *Annual review of neuroscience* 16, 403 (1993).
30. Q. Gu, Neuromodulatory transmitter systems in the cortex and their role in cortical plasticity. *Neuroscience* 111, 815 (2002).
31. P. Clarke, R. D. Schwartz, S. M. Paul, C. B. Pert, A. Pert, Nicotinic binding in rat brain: autoradiographic comparison of [3H] acetylcholine,[3H] nicotine, and [125I]-alpha-bungarotoxin. *The Journal of Neuroscience* 5, 1307 (1985).
32. K. Zilles *et al.*, Distribution of cholinergic receptors in the rat and human neocortex. *EXS* 57, 212 (1989).
33. G. L. Wenk, The Nucleus Basalis Magnocellularis Cholinergic System: One Hundred Years of Progress. *Neurobiology of Learning and Memory* 67, 85 (1997).
34. J. L. Muir, K. J. Page, D. Sirinathsinghji, T. W. Robbins, B. J. Everitt, Excitotoxic lesions of basal forebrain cholinergic neurons: effects on learning, memory and attention. *Behavioural brain research* 57, 123 (1993).
35. M. L. Voytko *et al.*, Basal forebrain lesions in monkeys disrupt attention but not learning and memory [published erratum appears in J Neurosci 1995 Mar; 15 (3): following table of contents]. *The Journal of Neuroscience* 14, 167 (1994).
36. T. W. Robbins *et al.*, Comparative effects of ibotenic acid- and quisqualic acid-induced lesions of the substantia innominata on attentional function in the rat: further implications for the role of the cholinergic neurons of the nucleus basalis in cognitive processes. *Behavioural brain research* 35, 221 (1989).
37. J. Turchi, M. Sarter, Cortical acetylcholine and processing capacity: effects of cortical cholinergic deafferentation on crossmodal divided attention in rats. *Cognitive Brain Research* 6, 147 (1997).

38. J. McGaughy, J. W. Dalley, C. H. Morrison, B. J. Everitt, T. W. Robbins, Selective Behavioral and Neurochemical Effects of Cholinergic Lesions Produced by Intrabasalis Infusions of 192 IgG-Saporin on Attentional Performance in a Five-Choice Serial Reaction Time Task. *The Journal of Neuroscience* 22, 1905 (March 1, 2002, 2002).
39. A. Chiba, D. Bucci, P. Holland, M. Gallagher, Basal forebrain cholinergic lesions disrupt increments but not decrements in conditioned stimulus processing. *The Journal of Neuroscience* 15, 7315 (November 1, 1995, 1995).
40. C. Hutchison, P. Nathan, L. Mrazek, C. Stough, Cholinergic modulation of speed of early information processing: the effect of donepezil on inspection time. *Psychopharmacology* 155, 440 (2001/06/01, 2001).
41. C. Stough *et al.*, Effects of nicotine on perceptual speed. *Psychopharmacology* 119, 305 (1995).
42. C. Stough, Nicotine and information processing: Recent studies. *Brain topography today. Amsterdam: Elsevier*, 799 (1998).
43. J. Thompson, C. Stough, D. Ames, C. Ritchie, P. Nathan, Effects of the nicotinic antagonist mecamylamine on inspection time. *Psychopharmacology* 150, 117 (2000).
44. M. Bauer *et al.*, Cholinergic Enhancement of Visual Attention and Neural Oscillations in the Human Brain. *Current Biology* 22, 397 (2012).
45. R. Thienel *et al.*, Muscarinic antagonist effects on executive control of attention. *The International Journal of Neuropsychopharmacology* 12, 1307 (2009).
46. M. L. Furey, P. Pietrini, J. V. Haxby, W. C. Drevets, Selective effects of cholinergic modulation on task performance during selective attention. *Neuropsychopharmacology* 33, 913 (2007).
47. A. A. Disney, C. Aoki, M. J. Hawken, Gain Modulation by Nicotine in Macaque V1. *Neuron* 56, 701 (2007).
48. A. M. Sillito, J. A. Kemp, Cholinergic modulation of the functional organization of the cat visual cortex. *Brain research* 289, 143 (1983).
49. W. Singer, Acetylcholine-induced inhibition in the cat visual cortex is mediated by a GABAergic mechanism. *Brain research* 487, 335 (1989).
50. H. Sato, Y. Hata, H. Masui, T. Tsumoto, A functional role of cholinergic innervation to neurons in the cat visual cortex. *Journal of Neurophysiology* 58, 765 (1987).
51. A. Thiele, J. L. Herrero, C. Distler, K.-P. Hoffmann, Contribution of Cholinergic and GABAergic Mechanisms to Direction Tuning, Discriminability, Response Reliability, and Neuronal Rate Correlations in Macaque Middle Temporal Area. *The Journal of Neuroscience* 32, 16602 (November 21, 2012, 2012).
52. M. J. Roberts *et al.*, Acetylcholine Dynamically Controls Spatial Integration in Marmoset Primary Visual Cortex. *Journal of Neurophysiology* 93, 2062 (April 1, 2005, 2005).
53. M. P. Kilgard, M. M. Merzenich, Cortical Map Reorganization Enabled by Nucleus Basalis Activity. *Science* 279, 1714 (March 13, 1998, 1998).
54. J. S. Bakin, N. M. Weinberger, Induction of a physiological memory in the cerebral cortex by stimulation of the nucleus basalis. *Proceedings of the National Academy of Sciences* 93, 11219 (October 1, 1996, 1996).
55. A. Thiele, Optimizing brain processing. *Nature neuroscience* 12, 1359 (2009).
56. M. R. Cohen, J. H. R. Maunsell, Attention improves performance primarily by reducing interneuronal correlations. *Nat Neurosci* 12, 1594 (2009).
57. J. F. Mitchell, K. A. Sundberg, J. H. Reynolds, Spatial Attention Decorrelates Intrinsic Activity Fluctuations in Macaque Area V4. *Neuron* 63, 879 (2009).
58. F. Marrosu *et al.*, Microdialysis measurement of cortical and hippocampal acetylcholine release during sleep-wake cycle in freely moving cats. *Brain Research* 671, 329 (1995).

59. I. D. Manns, A. Alonso, B. E. Jones, Discharge properties of juxtacellularly labeled and immunohistochemically identified cholinergic basal forebrain neurons recorded in association with the electroencephalogram in anesthetized rats. *The Journal of Neuroscience* 20, 1505 (2000).
60. A. Duque, B. Balatoni, L. Detari, L. Zaborszky, EEG correlation of the discharge properties of identified neurons in the basal forebrain. *Journal of Neurophysiology* 84, 1627 (2000).
61. G. Buzsáki *et al.*, Nucleus basalis and thalamic control of neocortical activity in the freely moving rat. *The Journal of Neuroscience* 8, 4007 (1988).
62. A. Kalmbach, T. Hedrick, J. Waters, Selective optogenetic stimulation of cholinergic axons in neocortex. *Journal of Neurophysiology* 107, 2008 (April 1, 2012, 2012).
63. C. D. Woody, B. E. Swartz, E. Gruen, Effects of acetylcholine and cyclic GMP on input resistance of cortical neurons in awake cats. *Brain research* 158, 373 (1978).
64. R. Metherate, N. Tremblay, R. W. Dykes, Acetylcholine permits long-term enhancement of neuronal responsiveness in cat primary somatosensory cortex. *Neuroscience* 22, 75 (1987).
65. Y. Lin, J. W. Phillis, Muscarinic agonist-mediated induction of long-term potentiation in rat cerebral cortex. *Brain research* 551, 342 (1991).
66. J. P. Donoghue, K. L. Carroll, Cholinergic modulation of sensory responses in rat primary somatic sensory cortex. *Brain research* 408, 367 (1987).
67. Y. Lamour, P. Dutar, A. Jobert, R. Dykes, An iontophoretic study of single somatosensory neurons in rat granular cortex serving the limbs: a laminar analysis of glutamate and acetylcholine effects on receptive-field properties. *Journal of Neurophysiology* 60, 725 (1988).
68. D. Rasmusson, R. Dykes, Long-term enhancement of evoked potentials in cat somatosensory cortex produced by co-activation of the basal forebrain and cutaneous receptors. *Experimental Brain Research* 70, 276 (1988).
69. N. Tremblay, R. A. Warren, R. W. Dykes, Electrophysiological studies of acetylcholine and the role of the basal forebrain in the somatosensory cortex of the cat. II. Cortical neurons excited by somatic stimuli. *Journal of Neurophysiology* 64, 1212 (1990).
70. N. Tremblay, R. A. Warren, R. W. Dykes, Electrophysiological studies of acetylcholine and the role of the basal forebrain in the somatosensory cortex of the cat. I. Cortical neurons excited by glutamate. *Journal of Neurophysiology* 64, 1199 (1990).
71. M. A. Howard III, D. J. Simons, Physiologic effects of nucleus basalis magnocellularis stimulation on rat barrel cortex neurons. *Experimental Brain Research* 102, 21 (1994).
72. M. P. Kilgard, M. M. Merzenich, Plasticity of temporal information processing in the primary auditory cortex. *Nat Neurosci* 1, 727 (1998).
73. M. P. Kilgard *et al.*, Sensory Input Directs Spatial and Temporal Plasticity in Primary Auditory Cortex. *Journal of Neurophysiology* 86, 326 (July 1, 2001, 2001).
74. J. M. Edeline, B. Hars, C. Maho, E. Hennevin, Transient and prolonged facilitation of tone-evoked responses induced by basal forebrain stimulations in the rat auditory cortex. *Experimental Brain Research* 97, 373 (1994).
75. M. A. Dimyan, N. M. Weinberger, Basal forebrain stimulation induces discriminative receptive field plasticity in the auditory cortex. *Behavioral neuroscience* 113, 691 (1999).
76. A. C. Puckett, P. K. Pandya, R. Moucha, W. Dai, M. P. Kilgard, Plasticity in the Rat Posterior Auditory Field Following Nucleus Basalis Stimulation. *Journal of Neurophysiology* 98, 253 (July 1, 2007, 2007).
77. S. Bao, E. F. Chang, J. D. Davis, K. T. Gobeske, M. M. Merzenich, Progressive Degradation and Subsequent Refinement of Acoustic Representations in the Adult Auditory Cortex. *The Journal of Neuroscience* 23, 10765 (November 26, 2003, 2003).

78. A. T. Gulledge, G. J. Stuart, Cholinergic Inhibition of Neocortical Pyramidal Neurons. *J. Neurosci.* 25, 10308 (2005).
79. D. A. McCormick, D. A. Prince, Mechanisms of action of acetylcholine in the guinea-pig cerebral cortex in vitro. *The Journal of Physiology* 375, 169 (1986).
80. A. Bandrowski, S. Moore, J. Ashe, Cholinergic synaptic potentials in the supragranular layers of auditory cortex. *Synapse* 41, 118 (2001).
81. S. Arroyo, C. Bennett, D. Aziz, S. P. Brown, S. Hestrin, Prolonged Disynaptic Inhibition in the Cortex Mediated by Slow, Non-α7 Nicotinic Excitation of a Specific Subset of Cortical Interneurons. *The Journal of Neuroscience* 32, 3859 (March 14, 2012, 2012).
82. Z. Xiang, J. R. Huguenard, D. A. Prince, Cholinergic Switching Within Neocortical Inhibitory Networks. *Science* 281, 985 (1998).
83. Y. Kawaguchi, Selective Cholinergic Modulation of Cortical GABAergic Cell Subtypes. *J Neurophysiol* 78, 1743 (1997).
84. P. G. Haydon, Glia: listening and talking to the synapse. *Nat Rev Neurosci* 2, 185 (2001).
85. M. Nedergaard, B. Ransom, S. A. Goldman, New roles for astrocytes: Redefining the functional architecture of the brain. *Trends in Neurosciences* 26, 523 (2003).
86. M. K. Shelton, K. D. McCarthy, Hippocampal Astrocytes Exhibit Ca2+ -Elevating Muscarinic Cholinergic and Histaminergic Receptors In Situ. *Journal of Neurochemistry* 74, 555 (2000).
87. A. Araque, E. D. Martin, G. Perea, J. I. Arellano, W. Buno, Synaptically Released Acetylcholine Evokes Ca2+ Elevations in Astrocytes in Hippocampal Slices. *J. Neurosci.* 22, 2443 (2002).
88. G. Perea, A. Araque, Properties of Synaptically Evoked Astrocyte Calcium Signal Reveal Synaptic Information Processing by Astrocytes. *J. Neurosci.* 25, 2192 (2005).

Chapter 2: Differential cholinergic modulation of a specific inhibitory microcircuit drives acetylcholine-induced changes in temporal dynamics of cortical activity

Naiyan Chen*, Hiroki Sugihara*,
Sami El Boustani, Mriganka Sur †

* Equal contribution

This chapter is presented as the draft prepared for publication submission.

N.C., H.S. and M.S. designed research
N.C., H.S. conducted and analyzed *in vivo* experiments.
N.C. conducted and analyzed *ex vivo* experiments.
S.E.B., H.S., N.C. performed computational simulations.
N.C., M.S. and H.S. wrote the paper.

Chapter 2: Differential cholinergic modulation of a specific inhibitory microcircuit drives acetylcholine-induced changes in temporal dynamics of cortical activity

Cholinergic modulation of the cortex is a powerful system for enhancement of information processing and dynamic modulation of brain states. The cellular circuit that underlies such neuromodulation, however, remains unresolved. Here we show that stimulation of cholinergic inputs to the visual cortex specifically and differentially drives a unique microcircuit: cholinergic inputs facilitate somatostatin-expressing inhibitory neurons (SOM) and via these, inhibit parvalbumin-expressing inhibitory neurons (PV) and inhibit/disinhibit excitatory pyramidal neurons. This is accompanied by robust desynchronization of local field potentials and strong decorrelation of visual responses between neurons. Using optogenetics to selectively block the responses of SOM neurons, we show that direct cholinergic activation of SOM neurons is necessary to drive both desynchronization and decorrelation. Computational simulations show that SOM-induced direct inhibition and indirect PV disinhibition are both necessary for decorrelation between pyramidal neurons. Together, these findings demonstrate a mechanistic basis of temporal representations in cortical populations, and the powerful role of specific inhibitory-excitatory circuits in actively shaping the dynamics of neuronal activity.

2.1. Introduction

Cholinergic innervation of the neocortex by afferent axons originating in the nucleus basalis (NB) of the basal forebrain(*1*) is a fundamental mechanism for modulating cortical sensory processing at both the level of brain states(*2*) and the temporal dynamics of neurons(*3*). Specifically, acetylcholine (ACh) can induce a highly desynchronized state as measured by the field potential activity of neuronal populations(*2*), accompanied by prominent decorrelation between the spike activity of individual neurons(*3, 4*); these related phenomena(*5*) are proposed to enhance information processing in alert, active and attentive conditions(*6-10*). Although recent computational studies have suggested inhibitory neurons can drive decorrelation and sparse coding in the cortex(*11, 12*) and experimental evidence shows that inhibitory neuronal activity correlates with(*13*) and can induce(*14, 15*) specific neuronal activity patterns, the cellular and circuit mechanisms that underlie the desynchronization and decorrelation observed during cortical cholinergic modulation remain unresolved. Specifically, many key questions remain open: Is ACh-induced desynchronization and decorrelation driven by inhibitory neurons? If so, which subtypes of inhibitory neurons are responsible, and how do their functional interaction with each other and other cell types in the circuit lead to brain state and neuronal spike correlation changes?

2.2. Results

2.2.1. *In vivo* optogenetic stimulation of ChAT-ChR2 expressing axons induces desynchronization of local field potentials and drives neuronal decorrelation in V1

We addressed these questions in the superficial layers of primary visual cortex (V1) in adult mice. ACh release *in vivo* was induced by photostimulation (473 nm, 1s, 20 Hz, 10 ms pulses, ~ 10 mW/mm^2) of channelrhodopsin-expressing cholinergic axons from the basal forebrain, in V1 of ChAT-ChR2 transgenic mice(*16*) (**Fig. 1A**). The effect of cholinergic activity was tested by measuring the local field potential (LFP) in V1 (*17*). Indeed, we observed that photostimulation of ChAT-ChR2 axons induced robust desynchronization of the LFP, similar to that induced by electrical stimulation of the nucleus basalis(*18*) (**Fig. 1B-1C, 1D**: post-stimulation decrease of low frequency events (<10 Hz, $P < 0.005$, paired t-test. Detailed numbers for all figures in Supplementary Table 1 and 2), increase of high frequency events (10 – 100 Hz, $P < 0.0005$, paired t-test).

One of the ways ACh(*3*) and attention(*7*) have been proposed to enhance the representation of information is through decorrelation between neurons, but the mechanisms underlying such decorrelation remain unresolved. We next examined whether activation of neocortical cholinergic axons can induce decorrelation by measuring the activity of single units with an array of multiple electrodes (**Fig. 1E**), in response to both natural movies and gratings of random orientation. Indeed, we observed a significant decorrelation between cortical neurons upon photostimulation (**Fig. 1F**) at the level of single units (**Fig. 1G**, $P << 0.0001$, paired t-test,

comparing the correlation coefficients before and after photostimulation; **Supplementary Fig. 1A**) and population of units (**Fig. 1H:** $P = 0.0001$, paired t-test, comparing population averaged correlation coefficients across animals before and after photostimulation; **Supplementary Fig. 1B**, see Supplementary Methods: *In vivo* single unit data analysis).

2.2.2. *In vivo* optogenetic stimulation of ChAT-ChR2 expressing axons evokes specific response signatures in SOM, PV and PYR neurons

To deconstruct the circuit that underlies ACh-induced LFP desynchronization and neuronal decorrelation, we performed *in vivo* cell-attached recordings from identified RFP-labeled SOM neurons (labeled with viral injection of a floxed RFP construct in V1 of ChAT-ChR2-SOM-cre mice, **Fig 2A-C**) and PV neurons (similarly labeled in ChAT-ChR2-PV-cre mice, **Fig 2D-F**), as well as *in vivo* recording of putative pyramidal (PYR) neuron single units (in ChAT-ChR2 mice, **Fig. 2G-I**) within the superficial layers of V1. Neuron types were also distinguished by their spike shape (**Supplementary Fig. 2A**; Supplementary Methods). Interestingly, activation of ChAT-ChR2 axons modulated different cell types differently. Robust facilitatory responses were observed in SOM neurons (**Fig. 2B, C**: $P < 0.05$, paired t-test, comparing normalized firing rate before and after photostimulation; duration = 30.9 ± 7.49 s) while suppressive responses were observed in PV neurons (**Fig. 2E, F**: $P <<< 0.0001$, paired t-test comparing normalized visual responses before and after photostimulation). In putative PYR neurons however, there was no significant change in response rate (**Fig. 2H, I**: $P > 0.2$, paired t-test, comparing normalized visual response before and after photostimulation). Thus, endogenous ACh release via

photostimulation evokes distinct *in vivo* signatures from SOM, PV and PYR neurons: SOM neurons are facilitated, PV neurons are suppressed, and the mean spike rate of PYR neurons does not change but their visual responses are decorrelated.

2.2.3. ACh application in slices evokes specific responses in SOM, PV and PYR neurons

To further examine the functional interaction that underlies the *in vivo* responses described above, we performed *ex vivo* whole-cell patch clamp recordings (**Fig. 3A**) from SOM neurons (tdTomato positive neurons in SOM-TD mice; **Fig. 3B-D**), PV neurons (in PV-TD mice; **Fig. 3E-G**) and PYR neurons (GFP-negative neurons in GAD67-GFP mice; **Fig. 3H-J**). A total of 101 neurons (from 42 animals) were examined in slices under current and voltage clamp, after ACh application and with different antagonists applied singly or in combination. Consistent with the *in vivo* recordings (Fig. 2B), ACh application evoked a robust train of action potentials in non-fast spiking, SOM-expressing neurons (**Fig. 3C *top*, Supplementary Fig. 3A**). These responses were significantly reduced in the presence of the cholinergic antagonists mecamylamine (**Fig. 3D**: $P < 0.0001$, paired t-test, comparing ACh-induced depolarization before and after mecamylamine) and atropine (**Fig. 3D**: $P = 0.005$, paired t-test, comparing ACh-induced depolarization before and after atropine; see also Supplementary Figs 2B-C demonstrating that superficial layer inhibitory neurons express both muscarinic and nicotinic ACh receptors). The facilitatory response in non-fast spiking inhibitory neurons persisted in the presence of glutamatergic and GABAergic antagonists (**Supplementary Fig. 3B-C**), indicating that it was due to direct action of ACh.

In PV neurons (patched in voltage clamp mode with Cl- based internal solution), ACh application increased the frequency of IPSCs (**Fig. 3F *top***), which were sensitive to cholinergic antagonists (**Fig. 3F *bottom*, Fig. 3G**: $P < 0.05$, paired t-test, comparing ACh-induced current amplitudes before and after mecamylamine; $P < 0.05$, paired t-test, comparing amplitudes before and after atropine). Unlike SOM neurons however, the responses in PV neurons were observed to be indirect and of inhibitory origin as they were significantly reduced by GABA antagonist (**Fig. 3F *bottom*, Fig. 3G**: $P < 0.01$, paired t-test, comparing ACh-induced current amplitudes before and after gabazine). Additionally, the ACh-induced increase in frequency of IPSCs in PV neurons was also abolished in TTX (**Fig. 3F *bottom*, Fig. 3G**: $P < 0.05$, paired t-test, comparing ACh-induced current amplitudes before and after TTX). The cholinergic response in PYR neurons was similar to that in PV neurons, so that ACh application led to an increase in frequency of IPSCs (**Fig. 3I *top***). This response was also significantly reduced in the presence of cholinergic antagonists (**Fig. 3I *bottom*, Fig. 3J**: $P < 0.001$, paired t-test, comparing ACh-induced current amplitudes before and after mecamylamine; $P < 0.02$, paired t-test, comparing amplitudes before and after atropine). Likewise, GABA antagonists and TTX also significantly reduced the response (**Fig. 3I *bottom*, Fig. 3J**: $P < 0.0001$, paired t-test, comparing ACh-induced current amplitudes before and after gabazine/bicuculline; $P < 0.005$, paired t-test, comparing ACh-induced current amplitudes before and after TTX). Thus, the ACh-induced responses in PV and PYR neurons appear to be indirectly mediated.

2.2.4. ACh-induced facilitation of SOM responses leads to ACh-induced inhibition in other cell types

We hypothesized that the TTX and gabazine sensitive increase in frequency of IPSCs in PV and PYR neurons is due to activation of SOM neurons by ACh and subsequent inhibitory drive from SOM neurons to PV and PYR neurons. To test the hypothesis, we transiently blocked the activity of SOM neurons by selectively expressing archaerhodopsin-3 (Arch)(*19*) in them by viral injection of a flexed Arch construct into V1 of SOM-cre mice; in addition, we crossed SOM-cre mice with GAD67-GFP mice for identifying inhibitory/fast-spiking neurons in conjunction with Arch blockade of SOM neurons (GAD67-GFP-SOM-cre mice). We carried out current and voltage clamp recordings in slices, with ACh application before and during green light stimulation of Arch in SOM neurons (**Fig. 4A**). Specific cell types were also identified by their electrophysiological characteristics (**Supplementary Fig. 4A).** Stimulation of Arch in SOM neurons (532 nm, 5-15s, continuous light, 0.174 mW/mm^2) indeed abolished their cholinergic responses (**Fig. 4B-D:** $P < 0.0005$, paired t-test, comparing ACh-induced depolarization in SOM neurons before and after Arch activation). Control recordings from SOM neurons in SOM-TD mice without Arch expression showed that green light stimulation alone did not induce any changes in ACh-evoked responses (**Supplementary Fig. 4B-C**). To test the causal relationship between the ACh-induced facilitation of SOM responses and ACh-induced IPSCs in PV and PYR neurons, we carried out voltage clamp recordings from putative PV neurons (identified by their fast-spiking properties and presence of GFP in GAD67-GFP-SOM-cre mice; **Fig. 4E-G**) and from putative PYR neurons (identified by their pyramidal morphology and absence of GFP in SOM-cre mice; **Fig. 4H-J**). Photostimulation of Arch in SOM neurons completely blocked the

ACh-induced increase in frequency of IPSCs in both putative PV neurons (**Fig. 4F, G** $P < 0.01$, paired t-test, comparing ACh-induced current amplitudes before and after Arch) and putative PYR neurons (**Fig. 4I, J**: $P < 0.0001$, comparing ACh-induced current amplitudes before and after Arch).

Thus, by a combination of optogenetics and pharmacology, these data reveal for the first time the circuit interactions between SOM, PV and PYR neurons in the context of ACh modulation. SOM neurons are directly activated by ACh, and release GABA to evoke IPSCs in PV and PYR neurons via GABA-A receptors (**Fig. 4K**). Because PV neurons widely inhibit PYR neurons (*20-22*), the SOM-mediated inhibition of PV neurons would subsequently disinhibit PYR neurons. Indeed, direct inhibition followed by disinhibition at sub-threshold levels is captured in ACh-induced responses of PYR neurons recorded in current clamp mode with a normal internal solution (**Supplementary Fig. 4D-E**). Such a circuit, comprising direct inhibition by SOM neurons and disinhibition via PV on PYR neurons, is also consistent with the *in vivo* observation of no net change in firing rate of PYR neurons during cholinergic modulation (**Fig. 2H, I**).

2.2.5. Desynchronization of local field potentials and neuronal decorrelation in V1 *in vivo* is mediated by SOM neurons

We next examined whether this specific inhibitory microcircuit can drive the ACh-induced changes in temporal dynamics of cortical activity, including LFP desynchronization and neuronal decorrelation (Fig.1). To establish a causal relationship between these phenomena and SOM neurons, we crossed ChAT-ChR2 mice with SOM-cre mice and expressed Arch in SOM neurons by viral injection (ChAT-ChR2-Som-cre mice; **Fig. 5A**). Blue light induced ChAT-ChR2 stimulation facilitated SOM neurons, but green light activation of Arch simultaneous with blue light stimulation blocked the facilitation and even reduced responses below background, consistent with hyperpolarization of SOM neurons by Arch (**Fig. 5A-C**; activation by blue light: $P < 0.0001$; suppression by green + blue light: $P < 0.0001$, paired t-test). We then measured the LFP in the Arch-injected V1 area (**Fig. 5D**). Activation of ChAT-ChR2 axons desynchronized the LFP (**Fig. 5E, F**: $P < 0.05$ comparing decrease in low frequency amplitudes, $P < 0.001$ comparing increase in high frequency amplitudes, paired t-test); however, this modulation was absent when Arch was activated during ChAT-ChR2 stimulation (**Fig. 5E, F** $P > 0.3$ comparing low and high frequency amplitudes separately, paired t-test). We further confirmed in ChAT-ChR2 control experiments that without Arch expression, green light presentation was not sufficient to abolish the desynchronization (**Supplementary Fig. 5A-C**). These findings thus directly demonstrate that SOM neurons play a critical role in cholinergic-induced desynchronization of network activity.

To examine the effect of SOM neurons on decorrelation of neuronal activity, we carried out single-unit recordings in ChAT-ChR2-SOM-cre mice within the region of V1 where Arch was expressed in SOM neurons (**Fig. 5G, Supplementary Fig. 6A**). ChAT-ChR2 activation with blue light induced decorrelation between neurons (**Fig. 5H, 5I**: $p << 0.0001$, paired t-test, **5J**: $P < 0.002$, paired t-test), but the decorrelation was blocked during green light activation of Arch (**Fig. 5H, 5I**: $P > 0.4$, paired t-test, **5J**: $P > 0.7$, paired t-test). In control ChAT-ChR2 experiments without Arch expression, green light alone did not alter the extent of decorrelation (**Supplementary Fig. 5D-F**).

Decorrelation can improve visual coding by reducing redundancy between neurons(*3, 23*). We carried out a simple discrimination analysis(*3*) and found that decorrelation indeed improved discrimination performance; this improvement was also blocked by activation of Arch in SOM neurons (**Supplementary Fig. 6B**). Collectively, these data demonstrate that cholinergic activation of SOM neurons drives neuronal decorrelation in V1 and thus potentially contributes to enhanced information processing.

2.2.6. Computational analyses show that both SOM-induced direct inhibition and indirect PV disinhibition are necessary for rate-independent neuronal decorrelation

Previous computational studies have shown that correlations between pairs of neurons generated by common inputs is a function of their spike rate(*12*). Our findings however showed no significant change in the spike rate of pyramidal neurons (Fig. 2I) during ACh-induced decorrelation (Fig. 1G-H). Although SOM neurons directly inhibit PYR neurons, they also disinhibit PYR neurons through suppression of PV neurons (Fig. 2E-F). It is thus be possible that a different mechanism than inhibition-dependent spike rate modulation exists for this rate-independent neuronal decorrelation. To investigate possible mechanisms, we simulated a network model of 2000 SOM, 1000 PV and 1000 PYR neurons where varying SOM inputs could alter the strengths of the direct inhibitory connection (SOM-PYR) and indirect disinhibitory connection (SOM-PV-PYR). All neurons were modeled as conductance-based leaky integrate-and-fire neurons (**Fig.6A; Supplementary Methods: Computational model**). We first generated a synchronously firing network that resembled basal correlated states (**Fig. 6B *top and middle panels***) by providing common inputs with independent noise to PYR and PV neurons.

We then introduced a PV-PYR synaptic delay(*24, 25*) that filtered out independent noise to favor signal propagation of common input. This led to the excitatory conductance being tightly followed by the inhibitory conductance(*26*) (**Fig. 6B bottom panel, Fig. 6C *left***). With SOM activation, the temporal relationship between the inhibitory and excitatory conductance was disrupted (**Fig. 6B *bottom;* Fig. 6C *right***). This was accompanied by a robust decorrelation of the spike profile of PYR neurons (**Fig. 6B *top;* Fig. 6D, 6F**) with little change in the firing rate of PYR neurons (**Fig.6E, Fig. 6G**), similar to that observed experimentally (Fig.1G-H; Fig. 2F,

2I). The model demonstrated that this relationship held for a wide range of SOM firing rates (**Fig. 6F**). As the SOM rate increased, the PV rate decreased while the PYR rate remained relatively unchanged and PYR correlation decreased (**Fig. 6E - F**), until the direct SOM-PYR inhibition became too strong for the indirect SOM-PV-PYR disinhibition to counter, thereby allowing rate-dependent decorrelation to dominate (*12*) (**Fig. 6G,** spike rates below point '2').

We further probed which connections were necessary for rate-independent decorrelation, by repeating the simulation in reduced circuits. In the three reduced circuits where each connection was selectively removed, we observed a rate-dependent correlation as reflected by the covariation of correlation with PYR rates (**Fig. 6G, Supplementary Fig. 7**). Thus, these analyses indicate that both the direct SOM-PYR inhibition and indirect SOM-PV-PYR disinhibition are necessary for rate-independent neuronal decorrelation of PYR neurons.

2.3. Discussion

Decorrelation between neurons can enhance(*3*) and even optimize(*27*) information processing. During execution of attentional tasks, decorrelation has been demonstrated to enhance population sensitivity to stimulus changes and the signal to noise ratio of neural signals (*7, 8*). Our study provides the first demonstration of a neural circuit that allows a mechanistic understanding of such temporal alterations of spike trains in the context of cholinergic modulation, a major neuromodulatory pathway implicated in attention and arousal(*6*). Specifically, we show experimentally that direct cholinergic facilitation of SOM neurons can activate both direct inhibitory and indirect PV disinhibitory pathways as well as decorrelate PYR neuronal spike profiles. Computational simulation further reveals that the two pathways together serve to destabilize intrinsic correlated network activity maintained by balanced excitation and PV inhibition(*26*), which are necessary for driving a and drive firing rate-independent decorrelation. These findings point to a crucial functional role of SOM neurons in intact cortical circuits, not only as players in spatial summation(*28*) and possibly in associative fear learning(*29*) but also in active shaping of the temporal structure of neural activity.

Our results indicate that direct SOM activation by ACh is also critical for the generation of network desynchronization (*1, 5*). This agrees with parallel observations of state-dependent SOM activation(*28, 30, 31*) and state-dependent variation in cholinergic output in the cortex(*32*) where more awake states favor both greater ACh release and higher SOM activity. Taken together, our data support the hypothesis that cortical circuits recruit unique inhibitory neuronal

cell types to modulate distinct brain states(*14, 31, 33, 34*) possibly for different brain functions, similar to that proposed in the hippocampus(*35*).

The co-existence of neuronal decorrelation and LFP desynchronization during ACh-induced SOM activation supports co-variation of temporal population activity with cortical states(*5*). Global cortical fluctuations have been proposed to induce neuronal correlations(*5*). During cholinergic modulation, these global fluctuations are suppressed, as reflected by a decrease in large amplitude, low frequency oscillations (Fig. 1D)(*2*) thereby leading to neuronal decorrelation(*5*). Small amplitude, high frequency oscillations then dominate(*2*), possibly due to sparsely distributed but simultaneously active neurons that fire synchronously(*9*). Indeed, previous findings have revealed the existence of such highly correlated neuronal pairs in decorrelated states(*36*). Future work will be necessary to characterize possible cell assemblies in the ACh-induced decorrelated states.

It is worth mentioning the link between high frequency events (gamma oscillations) and surround suppression through SOM activation. It has been recently shown that surround suppression in V1 neurons is mediated by SOM neurons(*28*). Interestingly, the same visual stimulus that evokes surround suppression has also been shown to induce gamma oscillations(*37*). Likewise, ACh has also been shown to modulate surround suppression(*38*) and gamma oscillations(*2*). Our finding on SOM neurons mediating ACh-induced desynchronization provides the missing link between these various observations. Further investigation will be

important to understand the difference, if any, between SOM- and PV-mediated gamma oscillations.

Our findings help to reconcile seemingly contradictory effects of cholinergic modulation and nucleus basalis stimulation on visual responses of V1 neurons(*27*). Cortical cholinergic activation has been linked to both fast GABA-mediated suppression(*3, 39*) and slow facilitation of visual responses of V1 neurons(*4, 27, 38-40*). These findings can in principle be explained by our results where direct cholinergic activation of SOM neurons can drive both direct inhibition and indirect disinhibition(*41*) on PYR neurons to vary their firing rate according to the relative strengths of the two pathways. In addition, cholinergic activation of astrocytes(*18*) can provide excitatory influences at a slower timescale. Our results also extend the conclusions of earlier slice studies (*42, 43*) which have demonstrated the excitation of non fast-spiking inhibitory neurons and induction of an inhibitory barrage in fast-spiking and pyramidal neurons by ACh. The findings we describe do not rule out the possibility of other neuronal cell types (*18, 44-46*) being active during cholinergic modulation. These include facilitatory responses observed in vasoactive intestinal peptide (VIP)(*44*) and cholecystokinin-expressing interneurons(*47*) where the former has recently been shown to exclusively provide weak inhibition to SOM neurons(*20*). However, these cell types, unlike SOM neurons, have little connection to the two other principal cell types, PV and PYR neurons(*20*) that we have demonstrated to be critical players in driving the ACh-induced temporal changes in cortical dynamics. It is likely that these VIP neurons are involved in the modulation of energy supply during cholinergic modulation(*47*). Additionally, mAChR mediated activation of prolonged facilitatory responses in cortical astrocytes and hippocampal PYR neurons have also been proposed to drive ACh-induced plasticity (*18, 45, 46*).

Together with our data showing SOM neurons as a dominant driver of both decorrelation and desynchronization in cortical networks, we propose that these distinct ACh-responsive cell-types can reorganize to form specialized microcircuits for enabling multiple brain functions during cholinergic modulation.

2.4. Acknowledgments

We thank Guoping Feng, Holly Robertson (MIT) for providing the ChAT-ChR2 mice; Ed Boyden, Aimei Yang (MIT) for providing Arch virus; Chuong Le for technical assistance with viral injections and immunohistochemistry; Travis Emery for technical assistance with the optogenetics laser setup; Michael Goard and Jitendra Sharma for providing technical advice. This work was supported by an A*STAR (Singapore) Fellowship (**NC**), NIH (R01EY007023 and R01EY018648), NSF and Simons Foundation grants (**MS**).

2.5. Figures

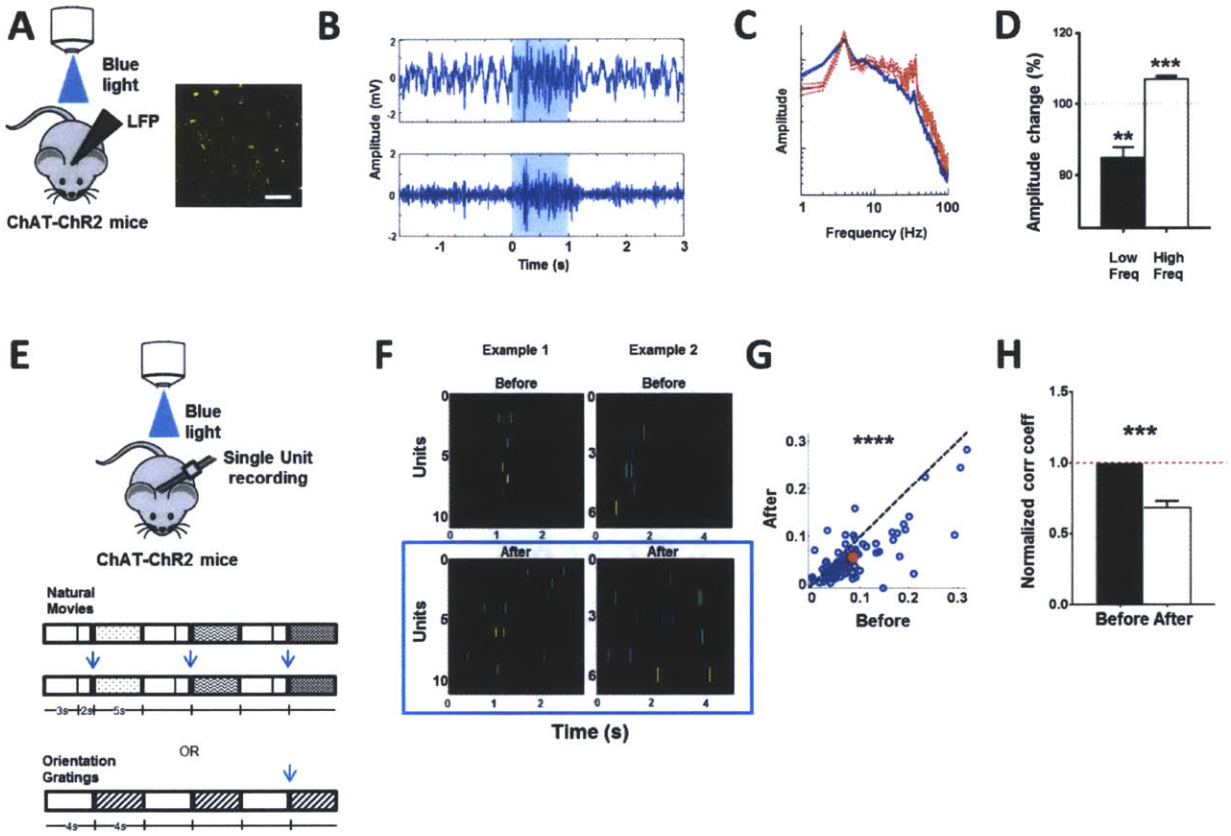

Fig. 1. *In vivo* optogenetic stimulation of ChAT-ChR2 expressing axons induces desynchronization of the local field potential (LFP) and decreases correlation between visual responses of layer 2/3 cortical neurons in V1. **(A)** (***Left***) Schematic illustration of the experimental setup for *in vivo* LFP recording using a glass pipette, with ChAT-ChR2 blue light stimulation through objective. (***Right***) Fluorescence image of ChAT-ChR2 axons in V1. Scale bar, 50 μm. **(B)** Desynchronization of the LFP during ChAT-ChR2 stimulation at t = 0 - 1 s (blue bar). (***Top***) Raw trace. (***Bottom***) Band pass filtered at 5 – 100 Hz. **(C)** Amplitude-frequency graph 1s before (blue) and after (red) NB stimulation, averaged over 10 trials. **(D)** ChAT-ChR2 stimulation induces a decrease in amplitude of low frequency events and increase in high frequency events. **(E)** (***Top***) Schematic illustration of the experimental setup for *in vivo* single unit recording using a tungsten electrode array during ChAT-ChR2 blue light stimulation through objective. (***Bottom***) Schematic of the visual and ChAT-ChR2 stimulation protocol. Each natural stimuli comprises 3 movies (patterned boxes) of 5s duration. Each random orientation grating stimuli comprises 3 trials of alternating 4s of blank screen and 4s of random orientation gratings. ChAT-ChR2 stimulation is indicated by arrows. **(F)** Two example experiments showing neuronal decorrelation before (control) and after ChAT-ChR2 stimulation. Each panel shows the responses of multiple single units recorded simultaneously during a single natural movie trial. Each unit is indicated by a different color. **(G)** Scatter plot showing single unit correlation coefficients before and after ChAT-ChR2 stimulation. Blue circles represent mean Pearson correlation coefficients for each neuron; red circle represents population averaged correlation coefficient. **(H)** ChAT-ChR2 stimulation induces a significant decrease in the population averaged normalized correlation coefficient across experiments. ** P<0.01, *** P<0.001, **** P<0.0001.

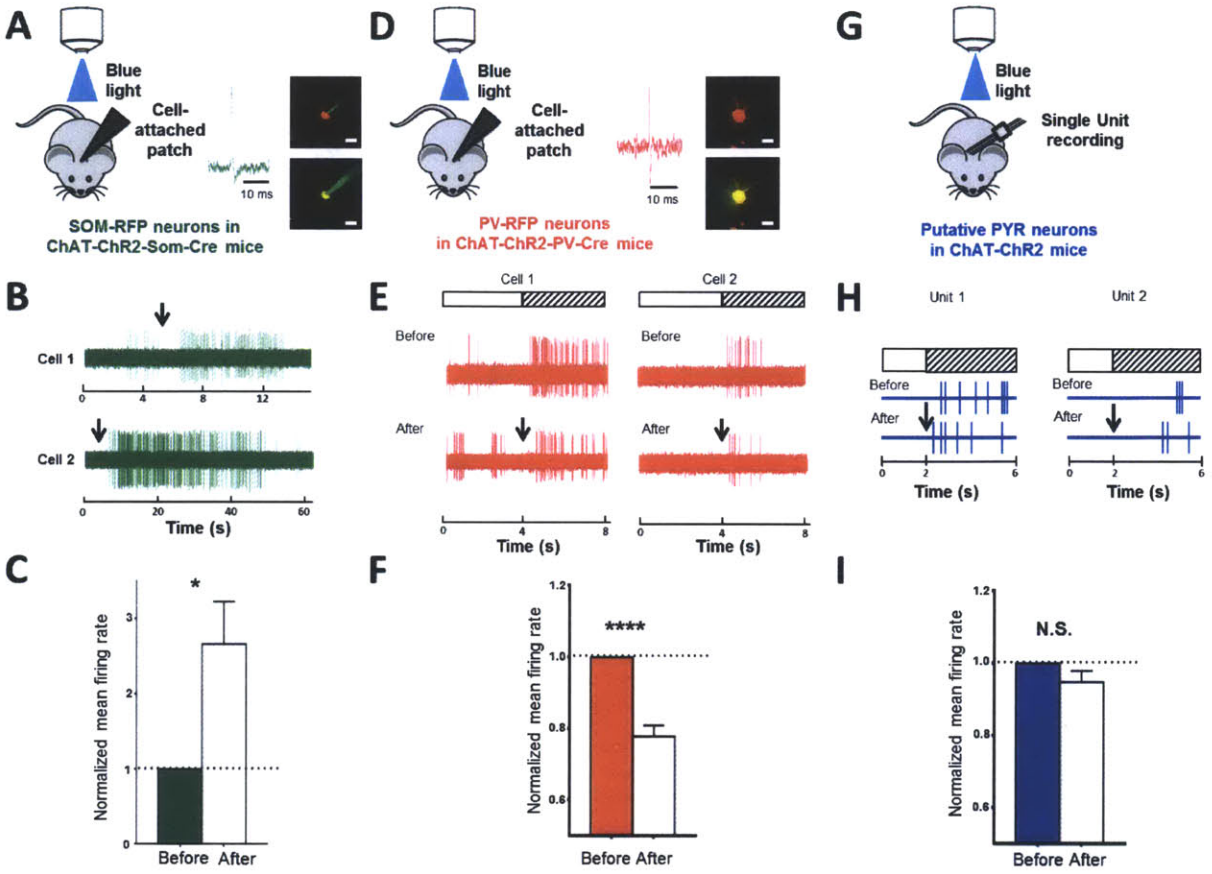

Fig. 2. *In vivo* optogenetic stimulation of ChAT-ChR2 expressing axons evokes diverse responses in layer 2/3 SOM, PV and putative PYR neurons. **(A)** (***Left***) Schematic illustration of the experimental setup for *in vivo* two-photon guided, cell-attached recording of labeled SOM neurons during ChAT-ChR2 blue light stimulation through objective. (***Middle***) A typical spike of a SOM neuron in a ChAT-ChR2-SOM-cre animal. (***Right, Top***) RFP+ SOM cells (red) were targeted with a glass pipette containing Alexa 488 dye (green). (***Right, Bottom***) The cell was filled to confirm its identity after recording. Scale bar, 20 µm. **(B)** Responses of 2 SOM neurons to ChAT-ChR2 stimulation (arrow). **(C)** Normalized mean firing rate 8s before and after ChAT-ChR2 stimulation. **(D)** Similar to (A) where RFP+ PV neurons in ChAT-ChR2-PV-cre mice were recorded. Scale bar, 20 µm. **(E)** Visual responses of 2 PV neurons before and after ChAT-ChR2 stimulation (arrow). ChAT-ChR2 stimulation was synchronized to the start of orientation grating stimulus (patterned bar). A blank grey screen (white bar) preceded visual stimulation. **(F)** Normalized mean visual response (over 4s) before and after ChAT-ChR2 stimulation. **(G)** Schematic illustration of the experimental setup for *in vivo* single unit recording in ChAT-ChR2 animal using a tungsten electrode array during ChAT-ChR2 blue light stimulation through objective. **(H)** Visual responses of 2 units (putative PYR neurons) before and after ChAT-ChR2 stimulation (arrow). ChAT-ChR2 stimulation was synchronized to the start of random orientation grating or natural movie stimulus (patterned bar). A blank screen (white bar) preceded visual stimulation. **(I)** Normalized mean visual response (over 4s) before and after ChAT-ChR2 stimulation. * $P<0.05$, **** $P<0.0001$. N.S., not significant.

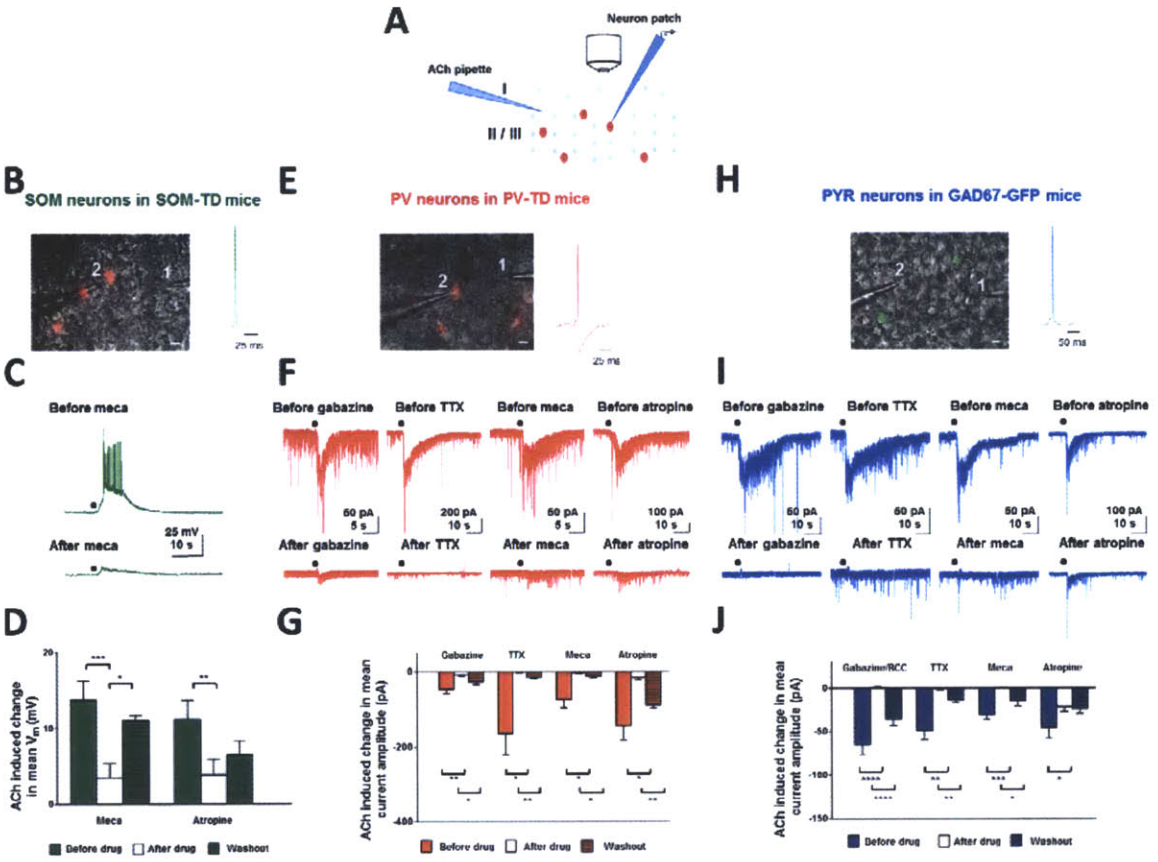

Fig. 3. *Ex vivo* application of ACh induces diverse responses in layer 2/3 SOM, PV and PYR neurons **(A)** Schematic illustration of whole-cell patch-clamp recording of layer 2/3 neurons in slices during ACh application. **(B)** (***Left***) Merged fluorescence and differential interference contrast (DIC) images of a tdTomato positive SOM neuron patched in a SOM-TD slice. Relative positions of ACh pipette (1) and patch pipette (2) were as indicated. Scale bar, 10 µm. (***Right***) A typical spike of a SOM neuron. **(C)** Local ACh application (black dot; 10 mM, 200 ms, 20 psi) evoked a transient train of action potentials in SOM neurons which were abolished by mecamylamine and atropine (not shown). **(D)** Population average of ACh-induced changes in mean V_m of SOM neurons before and after bath application of mecamylamine and atropine **(E)** Similar to (B) where fast-spiking, tdTomato positive PV neurons in PV-TD slices were recorded. Scale bar, 10 µm. **(F)** Local ACh application evoked IPSCs in PV neurons which were reduced by gabazine, TTX, meca and atropine. **(G)** Population average of ACh-induced changes in mean current amplitude (pA) of PV neurons before and after bath application of gabazine, TTX, meca and atropine. **(H)** Similar to (B) where GFP negative, PYR neuron in GAD67-GFP slices were recorded. Scale bar, 10 µm. **(I)** Local ACh application evoked IPSCs in PYR neurons which were abolished by gabazine, bicuculline (not shown), TTX, meca and atropine. **(J)** Population average of ACh-induced changes in mean current amplitude (pA) of PYR neurons before and after bath application of gabazine/bicuculline, TTX, meca and atropine. IPSCs were recorded with a chloride based intracellular whole-cell patch solution. * P<0.05, ** P<0.01, *** P<0.001, **** P<0.0001.

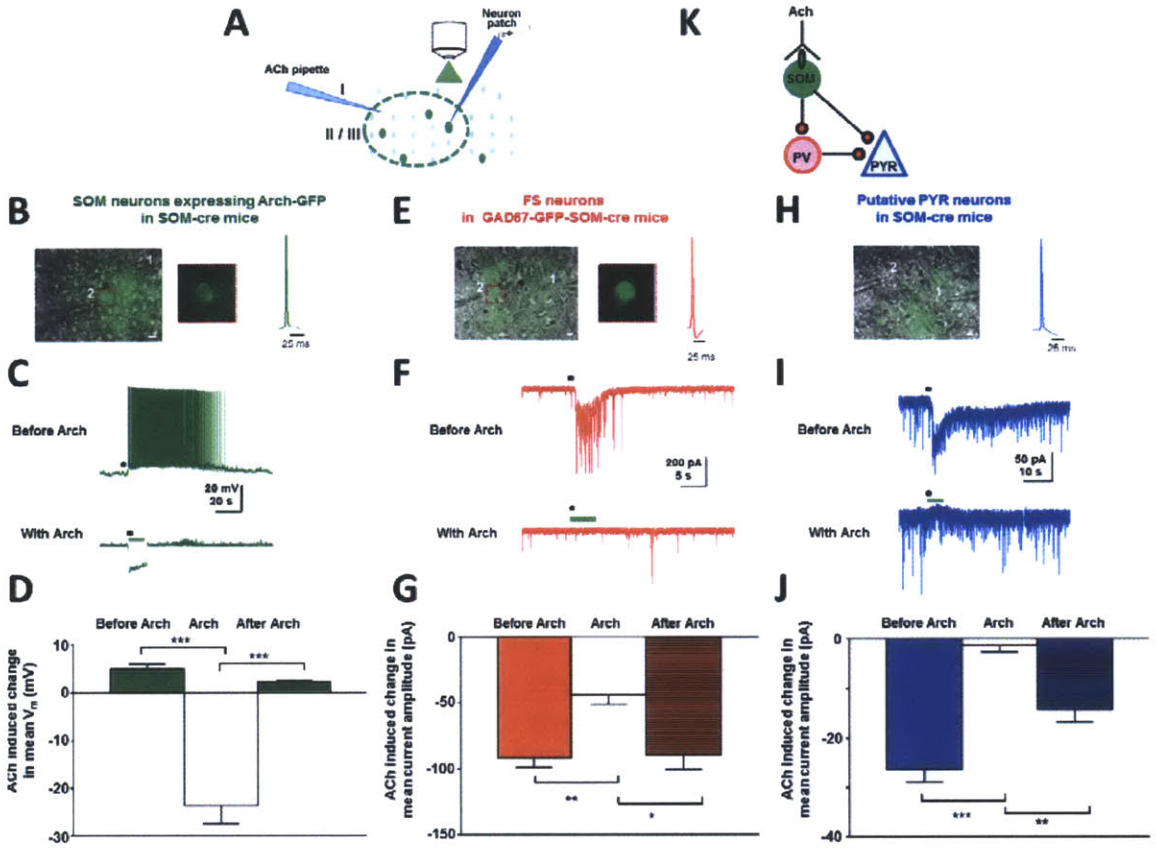

Fig. 4. ACh-induced facilitation of SOM responses leads to ACh-induced IPSCs in fast-spiking (FS, putative PV) and PYR neurons. **(A)** Schematic illustration of whole-cell patch-clamp recording of layer 2/3 V1 neurons during ACh pressure application, in SOM-cre slices at a location where AAV-flex-Arch-GFP virus was injected (green dotted region), with green light stimulation of Arch to block SOM neurons. **(B)** (***Left***) Merged fluorescence and DIC images of a GFP-positive, Arch-expressing SOM neuron patched in a SOM-cre slice. Relative positions of ACh pipette (1) and patch pipette (2) were as indicated. (***Middle***) Magnified image of the SOM neuron patched in the previous image. Scale bar, 10 μm. (***Right***) A typical spike of a SOM neuron. **(C)** Local ACh application (black dot; 10 mM, 200 ms, 20 psi) evoked a transient train of action potentials in an Arch-expressing SOM neuron which was abolished by green light exposure (green bar). **(D)** Population average of ACh-induced changes in mean V_m of SOM neurons before, during and after Arch. **(E)** Similar to (B) where GFP positive, non-Arch-expressing, FS neurons in a GAD67-GFP-SOM-cre slice were recorded. Scale bar, 10 μm. Note that the neuron is completely filled with GFP in contrast to the annular filling observed in Fig. 4B. Scale bar, 10 μm. **(F)** Local ACh application evoked IPSCs in a GFP positive, FS neuron which is abolished by green light exposure (green bar). **(G)** Population average of ACh-induced changes in mean current amplitude of GFP positive neurons before, during and after Arch. **(H)** Similar to (B) where GFP negative, putative PYR neuron in a SOM-cre slice were recorded. Scale bar, 10 μm. **(I)** Local ACh application evoked IPSCs in a putative PYR neuron which were abolished by green light exposure (green bar). **(J)** Population average of ACh-induced changes in mean current amplitude (pA) of putative PYR neurons before, during and after Arch. IPSCs were recorded with a chloride based intracellular whole-cell patch solution **(K)** Proposed mechanism for cholinergic action on specific cortical cell types. Red circles and green ovals indicate inhibitory synapses and cholinergic receptors respectively. * P<0.05, ** P<0.01, *** P<0.001

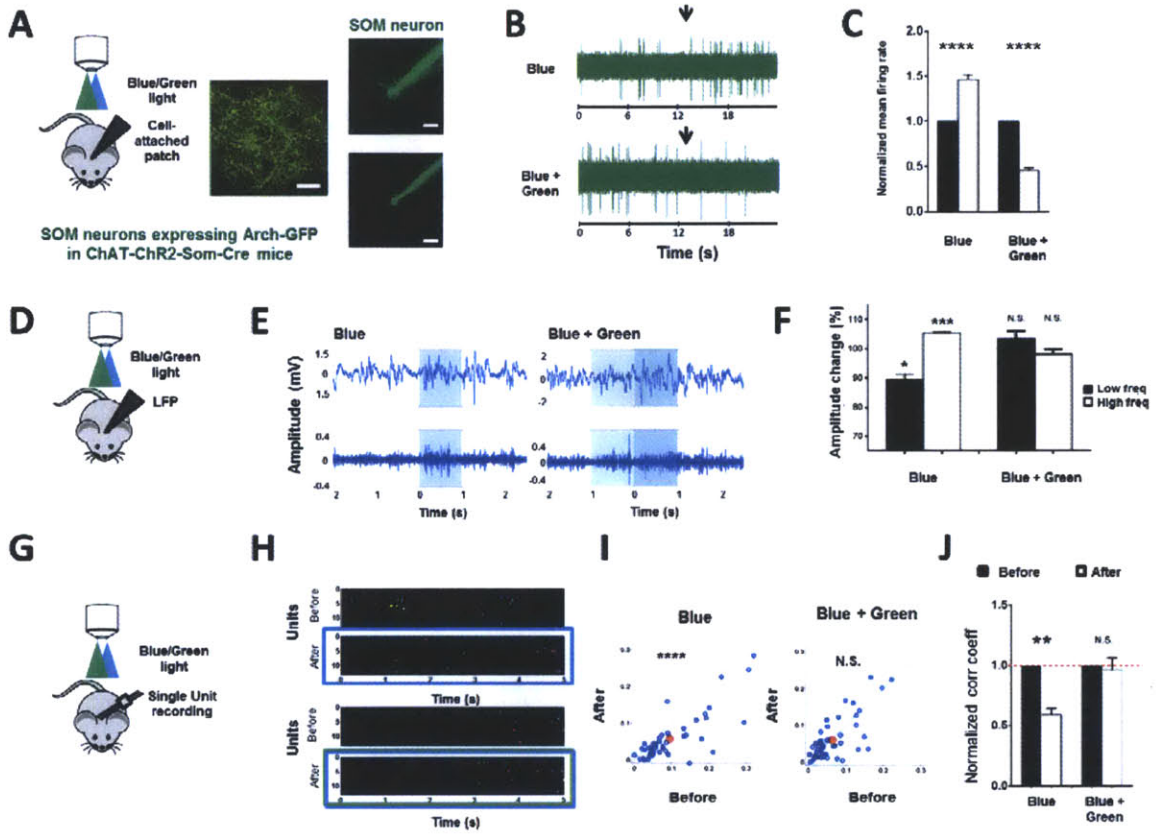

Fig. 5. *In vivo* ChAT-ChR2 stimulation induced desynchronization of local field potentials and neuronal decorrelation in V1 is mediated by SOM neurons. **(A)** (***Left***) Schematic illustration of the experimental setup for *in vivo* two-photon guided, cell-attached recording of SOM neurons during ChAT-ChR2 blue light stimulation and SOM-Arch green light stimulation through objective. (***Middle***) Image of Arch-GFP expression in V1. Scale bar, 50 μm. (***Right, Top***) An Arch-expressing SOM neuron with membrane-bound GFP was targeted with a glass pipette containing Alexa 488 dye (green). (***Right, Bottom***) The cell was filled to confirm its identity after recording. Scale bar, 20 μm. **(B)** Responses of a SOM neuron to ChAT-ChR2 stimulation (arrow, 1s duration) (***Top***) without and (***Bottom***) with Arch stimulation (10s duration, where the start precedes ChAT-ChR2 stimulation by 1s). **(C)** Normalized mean firing rate 8s before and after ChAT-ChR2 stimulation without and with Arch stimulation. **(D)** Schematic illustration of the experimental setup for *in vivo* local field potential recording using a glass pipette. **(E)** Desynchronization of the local field potential during optogenetic ChAT-ChR2 stimulation at t = 0 - 1 s (blue bar) (***Left***) is blocked by Arch stimulation during t = -1 – 1 s (green bar) (***Right***). The raw trace (***Top***) is band pass filtered at 5 – 100 Hz (***Bottom***). **(F)** ChAT-ChR2 blue light stimulation induces a decrease in amplitude of low frequency events (<10 Hz) and increase in high frequency events (10 – 100 Hz) respectively. This is blocked during simultaneous SOM-Arch green light and ChAT-ChR2 blue light stimulation. **(G)** Schematic illustration of the experimental setup for *in vivo* single unit recording using a tungsten electrode array. **(H)** An example experiment showing a decrease of between cell-correlation before (control) and after ChAT-ChR2 stimulation (blue box). The decorrelation is absent during simultaneous SOM-Arch green light and ChAT-ChR2 blue light stimulation (blue and green boxes). Each panel shows the responses of multiple single units recorded simultaneously during a single natural movie trial. Each unit is indicated by a different color. **(I)** Scatter plot showing the between-cell correlation coefficients before and after ChAT-ChR2 stimulation (***Left***) as well as before and after simultaneous SOM-Arch and ChAT-ChR2 stimulation (***Right***). Each blue circle represents the average correlation coefficient between a single neuron and all other neurons in the same recording; the red circle is the population average. **(J)** The population averaged normalized correlation coefficient across experiments during ChAT-ChR2 blue light stimulation and

during simultaneous SOM-cre Arch green light and ChAT-ChR2 blue light stimulation. * $P<0.05$, ** $P<0.01$, *** $P<0.001$, **** $P<0.0001$. N.S., not significant.

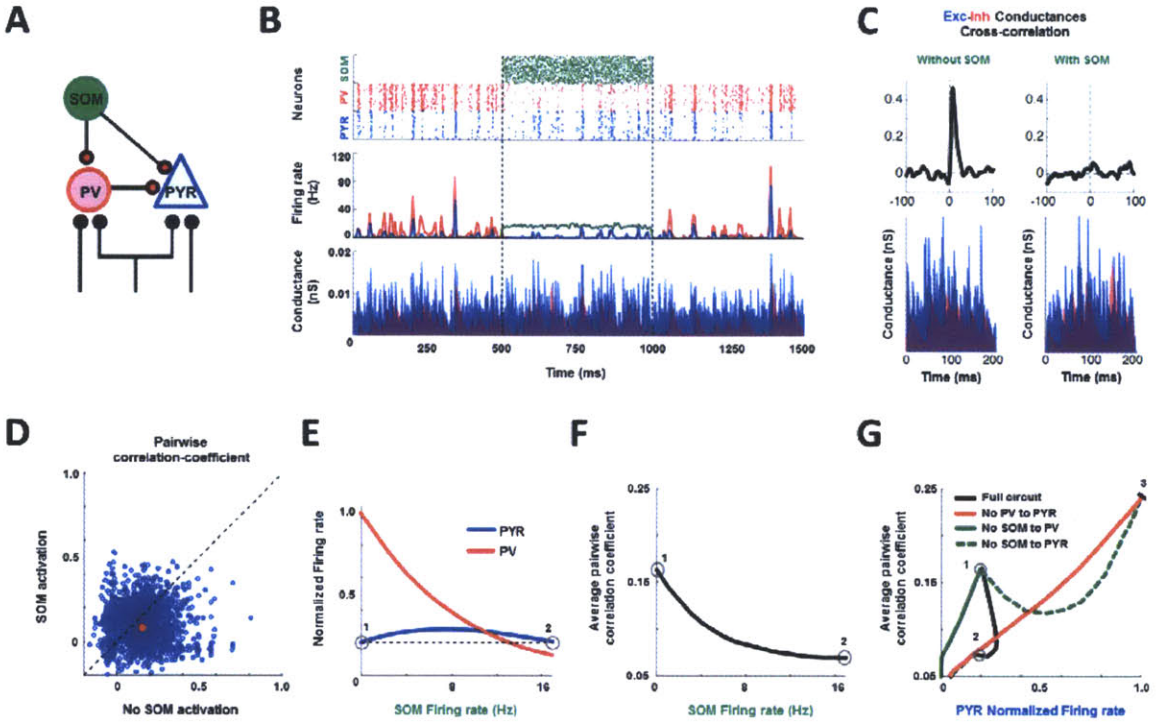

Fig. 6. SOM-evoked direct inhibitory and indirect disinhibitory pathways are both necessary for rate-independent neuronal decorrelation. **(A)** Schematic of the modeled circuit comprising the direct inhibitory (SOM-PYR) and indirect disinhibitory (SOM-PV-PYR) pathways. Red and black circles indicate inhibitory synapses and common input with independent noise respectively. **(B)** (***Top***) Raster plot and (***Middle***) averaged firing rate of SOM (green), PV (red) and PYR (blue) neurons. (***Bottom***) Inhibitory (red, comprising PV and SOM inputs) and excitatory (blue) conductance of PYR neurons. Blue shaded regions indicate SOM activation. **(C)** Cross correlation between excitatory and inhibitory conductances (***Top left***) without and (***Top right***) with SOM activation (***Bottom***) The conductance traces in Fig. 6B, *bottom* at expanded time scale. **(D)** Scatter plot showing the between-cell correlation coefficients of PYR neurons without and with SOM activation. Each blue circle represents the correlation coefficient between two single neurons while the single red circle is the population averaged correlation coefficient. **(E)** Relationship between the normalized firing rates of PYR and PV with varying SOM firing rates. Circles 1 and 2 refer to data points plotted in Fig. 6D. **(F)** Relationship between the averaged correlation coefficient of PYR neurons with varying SOM firing rates. **(G)** Relationship between the averaged correlation coefficient with normalized firing rates of PYR neurons in the full model circuit (black) as well as in the circuits where the following connections are individually removed: PV to PYR (red), SOM to PV (green), SOM to PYR (green dotted). Circles 1 and 2 are the same reference data points in Fig. 6E-F. With zero SOM rate, the 'full circuit', 'No SOM to PV' and 'No SOM to PYR' circuits converges at circle 1 while the 'No PV to PYR' circuit rests at point 3. As the SOM rate increases from circle 1 to 2 in the 'full circuit', the SOM-PV-PYR disinhibition becomes weaker relative to the SOM-PYR inhibition. Beyond circle 2, the disinhibition is negligible relative to the inhibition, and the 'full circuit' merges with the 'No PV to PYR' circuit.

2.6. Methods

Details of mice, viral constructs, viral injection procedures, *in vivo* surgery, *in vivo* recording techniques including cell-attached recording, single unit recording, and local field potential recording, visual stimulation and optogenetic laser stimulation protocols, slice preparation, *ex vivo* whole cell patch-clamp recording procedures, immunohistochemistry protocol and computational model are described in the **Supplementary Methods.**

2.7. Supporting Information

2.7.1. Supplementary Methods

Mice

For *in-vivo* experiments, local field potential, single unit and cell-attached recordings were performed on adult mice between 2 - 6 months old. For slice experiments, whole-cell patch clamp recordings were performed on P13 – P28 mice. The following mouse lines were used: ***Figure 1:*** ChAT-ChR2-EYFP line 6 (ChAT-ChR2)(*16*), ***Figure 2:*** ChAT-ChR2; ChAT-ChR2-SOM-cre-RFP and ChAT-ChR2-PV-cre-RFP mice were generated by crossing the ChAT-ChR2 +/- with SOM-Cre knockin driver mice (SOM-cre +/+, Jackson Labs) and PV-Cre knockin driver mice (PV +/+, Jackson Labs) respectively(*48*) before viral injection of the adenoassociated virus (AAV, serotype 2/9) containing the ***loxP-STOP-loxP-RFP*** construct(*49, 50*). ***Figure 3:*** SOM-TD and PV-TD were generated by crossing the CAG- tdTomato +/+ mice(*51*) (td, Jackson labs) with SOM-cre +/+ and PV-cre +/+ respectively; GAD-67-GFP(*52*). ***Figure 4:*** SOM-cre-Arch mice were generated by injecting the AAV-CAG-FLEX-Arch-GFP virus (Arch)(*53*) into SOM-cre +/- mice; GAD-67-GFP-SOM-cre-Arch mice were generated by first crossing GAD-67-GFP with SOM-cre +/+ before injecting the Arch virus. ***Figure 5:*** ChAT-ChR2-SOM-cre-Arch-GFP mice were generated by crossing ChAT-ChR2 +/- with SOM-Cre+/+ before injecting the Arch virus. All experiments were performed under protocols approved by the Animal Care and Use Committee at MIT and conformed to NIH guidelines.

Viral injection

The procedure has been described earlier(*48, 49*). Briefly, adult mice were anesthetized in isoflurane before the skull was thinned and the dura in primary visual cortex (V1) was punctured using a glass micropipette filled with virus. A volume of 0.25 μl of virus was injected at the depth of 250 μm. Experiments were performed at least 2 weeks post-injection.

***In vivo* surgery**

Mice were anesthetized with urethane (1.15 mg/g). Ophthalmic ointment was used to protect the animal's eyes during the surgery and replaced with silicon oil during imaging. Body temperature was maintained at 37.5°C with a heating pad. A metal headplate was attached to the skull with cyanoacrylate glue and dental acrylic. A 2 x 2 mm craniotomy was made over V1 which was later covered with a thin layer of 2% agarose in ACSF (140 mM NaCl, 5mM KCl, 2 mM $CaCl_2$, 1mM $MgCl_2$, 0.01 mM EDTA, 10 mM HEPES, 10 mM glucose, pH 7.4).

***In vivo* cell-attached recording**

Glass pipettes (1.5 μm tip size, 3–7 MΩ) filled with Alexa dye 488 (A488, *Invitrogen, Carlsbad, CA*) and held at positive pressure were visually-guided into V1 with a two-photon microscope using ScanImage software(*54*) and directed to 100 - 200 μm below the pial surface (layer 2/3) using a micromanipulator(*49*). The resistance of the pipette was monitored during the penetration by delivering -0.5 nA current pulses for 6.3 ms at 0.55 Hz with Clampex software (Axon Instruments, v8.1) and Axoclamp-2A amplifier (Axon Instruments). When a seal with a cell during the advancement of pipette was obtained (assessed by increase in pipette tip resistance)

and well-isolated spikes were detected on Clampex during visual stimuli presentation, sustained negative pressure was applied (0.2–0.6 psi) to secure the seal(*55*). To fill the recorded cells, current pulses (35 ms, 900-2000 nA) were delivered at 15 Hz for 30-60 s. Recordings were performed at a sampling rate of 30 KHz and filtered between 300 Hz and 10 KHz. The pClamp data was analyzed with Clampfit software v 10.2 (MDS Analytical Technologies) for spike detection and the analyzed data was then imported in Matlab and further analyzed with custom-written scripts to calculate firing rates in epochs with and without visual and/or optogenetic stimulation.

***In vivo* single unit recording**

Single-unit extracellular recordings were made using tungsten microelectrodes (0.8 MΩ; FHC). Similar to what has been described in earlier work(*18*), the signal was amplified and recorded using the Plexon Neurotechnology Research Systems (4-8 channels, 40kHz at 12-bit resolution, Plexon Inc.). The signal was thresholded using an online amplitude discriminator and played over an integrated stereo amplifier (Optimus). Offline analysis to sort waveforms for each unit was performed using commercial programs (Offline Sorter version 2.8.8; Plexon Inc.). Post processing was done using in-house code written in MATLAB.

***In vivo* single unit data analysis**

Data analysis was performed with in-house code written in MATLAB. Units were selected by two criteria for further analysis: visually responsiveness (paired t-test, $P<0.05$) and firing rate (>0.1 Hz). To avoid artifact of the same units being picked up by more than one electrode, we also removed units which have high correlation with others (pair-wise between-units correlation

coefficient: >0.1, with 1 kHz bin). For correlation analysis across units, we first binned responses at 10 Hz before the mean Pearson correlation coefficient for each cell was calculated using all pairs of responses between the cell and other cells recorded simultaneously. Population averaged correlation coefficients in Fig. 1H, 5J, Supplementary Fig. 1B and 5F were computed by first averaging the correlation coefficient across all cells recorded simultaneously before taking the mean of these averaged correlation coefficients across experiments.

The discrimination analysis in Supplementary Fig. 6B was computed as previously described (*3*). We first binned responses at 100 ms segments. Discriminability was then calculated by comparing the similarity of single-trial responses to two templates comprising mean trial-averaged responses. Each discrimination was quantified by calculating the Euclidean distance between (a) single-trial responses in a given bin and the mean trial-averaged responses in the same bin, and between (b) the single-trial responses and the mean trial-averaged responses in a different bin. Discrimination was assigned correct when the distance (a) was smaller than distance (b). Two-way ANOVA was used to assess effect of number of units included to calculate discrimination performance, and effect of light stimulation. Data sets with more than 9 units were used for this analysis.

***In vivo* local field potential (LFP) recording**

The LFP recordings were made using a glass pipette (2.5 – 3 μm tip size, 2-3 MΩ) to prevent optogenetic laser stimulation-induced artifacts(*56*). The pipette, filled with A488 and Alexa dye 494 (A594), is visually-guided into V1 with a microscope and directed to 100 - 200 μm below

the pial surface (layer 2/3) using a micromanipulator. A single channel on the Plexon Neurotechnology Research Systems is used to amplify and record the signal.

Visual and optogenetic stimulation

Natural movies and random orientation gratings were displayed on a 19 inch LCD monitor situated 15 cm from the eyes.

Each natural stimuli experiment consisted of 40 – 60 trials where each trial comprises a set each of control and optogenetic stimulation conditions. Each set comprises three 5-seconds natural movies (128 x 128 pixels) selected from the van Hateren natural movie database. Each movie is preceded by a control period consisting of 3s of blank grey screen and 2s of still image of the first movie frame to avoid onset effect. Multiple trials were performed with alternating absence and presence of ChAT-ChR2 stimulation synchronized to the start of each movie (see **Fig. 1E**), where Arch stimulation precedes by 1s and continues for the duration of the ChAT-ChR2 stimulation so as to ensure suppression of SOM neurons during this period.

Each random orientation grating experiment consisted of 40 – 60 trials where each trial comprises 3 repeats of alternating 4s of blank screen and 4s of random orientation grating presentation. ChAT-ChR2 stimulation is synchronized to the start of the third repeat of gratings presentation (see **Fig. 1E**), where Arch stimulation precedes by 1s and continues for the duration of the ChAT-ChR2 stimulation. The random orientation grating stimuli were generated with the Psychophysics toolbox(*57*) in Matlab. The stimuli consisted of square wave drifting gratings at

100% contrast in 8 randomly-permuted directions, each 45 degrees apart and lasting for 450 ms.

To perform optogenetic stimulation of ChR2 and Arch, we used diode-pumped solid state blue and green lasers with analog intensity control (473 nm, 200 mW, MBL-III-473, and 532 nm, 200 mW, MBL-III-532, respectively, OptoEngine, LLC). Pulse patterns (20 Hz, 10ms of pulse width) were driven via custom D/A optogenetics software written in Matlab.

The onset of both visual stimuli was synchronized to the initiation of acquisition of cell-attached spike, single unit, LFP recordings and optogenetic stimulation via trigger pulses.

Photostimulation of ChAT-ChR2

When blue light is shone at V1, both the cholinergic axons from the basal forebrain and a small, localized set of intrinsic cholinergic interneurons are photostimulated. The functional consequences of the activation of the intrinsic cholinergic interneurons have however been shown to be limited (*58, 59*).

Slice physiology

Visual cortical coronal slices (300 μm) were cut in slicing buffer (< 4 °C, perfused with carbogen comprising 95% O_2/5% CO_2, pH 7.33 – 7.38) with a vibratome (Leica VT 1200S) and incubated in artificial cerebral spinal fluid (ACSF) at room temperature for at least 30 min before being transferred to a slice chamber for patch-recordings. All experiments were performed in carbogen-perfused ACSF. The ACSF contained (in mM): NaCl, 130; $NaHCO_3$, 24; KCl, 3.5;

NaH_2PO_4, 1.25; Glucose, 10; $CaCl_2$, 2.5; $MgCl_2$, 1.5. The slicing buffer is of similar composition as ACSF except (in mM): $CaCl_2$, 1; $MgCl_2$, 5. The intracellular pipette solution for patching neurons in current clamp mode contained (in mM): KCl, 20; K-Gluconate, 100; HEPES, 10; Mg-ATP: 4; Na-GTP: 0.3; Na-Phosphocreatine, 10, pH 7.4, 295 mOsm. For recording IPSCs in voltage clamp mode, a chloride-based intracellular solution was used (in mM): KCl, 120; HEPES, 10; Mg-ATP: 4; Na-GTP: 0.3; Na-Phosphocreatine, 10, pH 7.4, 295 mOsm. The drugs used include: Acetylcholine chloride (ACh, 10 mM), Atropine sulfate (Atropine, 50 μM), Mecamylamine hydrochloride (Meca, 10 μM), Bicuculline methiodide (BCC, 20 μM) and Tetrodotoxin (TTX, 1 μM) were purchased from Sigma; D-(−)-2-amino-5-phosphonopentanoic acid (D-APV, 50 μM), 2, 3-Dioxo-6-nitro-1,2,3,4-tetrahydrobenzo[*f*]quinoxaline-7-sulfonamide disodium salt (NBQX, 10 μM) and Gabazine (10 μM) were purchased from Tocris. Drugs were bath applied, except for ACh which was applied by pressure injection with a picospritzer.

Intracellular recording in slices

Glass pipettes (4 – 7 MΩ) were pulled with a Sutter P1000 puller (Sutter instruments). Layer 2/3 cells were visualized with an Olympus BX61WI microscope coupled with an LUMPLFLN 40x water immersion lens, infrared-DIC optics and QCapture Pro driven Retiga Exi CCD camera (Qimaging). A subset of experiments in Fig. 3H-J was performed in C57BL/6 slices where regular-spiking (RS) excitatory neurons were identified according to the following morphological and electrophysiological characteristics: pyramidal-shaped soma, apical dendrites radially projecting towards the pial and basal dendrites directed downwards and laterally(*60*) and adaptation of spike frequency when stimulated with a constant current(*61*). In GAD-67-GFP slices in Fig. 3H – J and in SOM-cre-Arch slices in Fig. 4H-J, PYR neurons were identified by

the absence of GFP and their electrophysiological and morphological characteristics. In GAD-67-GFP-SOM-cre-Arch slices used in Fig. 4E-G, fast-spiking (FS) neurons are identified by their expression of GFP and their FS characteristic. In GAD-67-GFP slices used in Supplementary Fig. 3B-E, non FS neurons are identified by their GFP expression and non FS characteristic. Recordings were performed with a multiclamp 700B amplifier and digidata 1440A data acquisition system, with pClamp software in both the current- and voltage-clamp modes. Analysis was performed with the Clampfit 10.2.0.12 software. Optogenetic stimulation of Arch was performed using output from a Lumen 200 fluorescence lamp (5% light output, Prior Scientific, Inc.) through a green filter. In Fig. 3 and 4, the ACh induced changes in response (%) after bath application of drugs is defined as

$$\frac{(Ach\ response)_{after\ drug} - (Ach\ response)_{before\ drug}}{(Ach\ response)_{before\ drug}} \times 100$$

Immunohistochemistry

SOM-TD mice (P34, see **Supplementary Fig. 2B-C**) were anesthetized with 4% isoflurane and perfused transcardially with saline followed by chilled 4 % paraformaldehyde in 0.1 M PBS. The brains were then postfixed in 4 % paraformaldehyde in 0.1 M PBS (<4°C) overnight. The fixed brains were sectioned into 50 μm visual cortical slices with a vibratome and then blocked in 10% normal goat serum with 1% triton in PBS (1 hour, room temperature) before being stained with rabbit anti-M1, anti-M2 (1:200, Millipore, AB5164, AB5166), rabbit anti-nAChR alpha4, rabbit anti-nAChR beta2 and rabbit anti-nAChR alpha7 (1:200, Abcam, ab41172, ab55980, ab23832) overnight (< 4 °C). This was followed by a 3 hour incubation in Alexa Fluor 488 goat anti-rabbit (1:200, Invitrogen, A11034) before being mounted on a glass slide with the Vectashield Hardset mounting media (Vector Labs). The slides were imaged using a confocal microscope (Zeiss LSM

5 Pascal Exciter) and the images were analyzed for co-localization of tdTomato positive SOM neurons and the respective cholinergic receptors stains.

Computational model

The simulated network comprised 1000 PYR, 1000 PV and 2000 SOM neurons. All neurons were modeled as conductance-based leaky integrate-and-fire neurons with membrane time constant τ_m = 20ms, leak conductance G_{leak} = 10nS and resting membrane potential V_{rest} = -70mV. The neuron fired whenever the membrane potential crosses the threshold V_{th} = - 40mV before artificially clamping it at a reset membrane value V_{reset} = -65mV for a refractory period τ_{ref} = 5ms. Synaptic interactions were modeled as instantaneous increases in excitatory (PYR) or inhibitory (PV, SOM) conductances followed by exponential decays with τ_{exc} = 2ms and τ_{inh} = 15ms. The receptors' reversal potentials were E_{exc} = 0mV and E_{inh} = -75mV. PYR and PV received feedforward inputs. PYR and PV neurons were driven by independent Poisson noise with common Poisson inputs at an overall fixed rate of 200 Hz, with the ratio between independent noise and common input at 0.6. Each PYR/PV neuron received 20 different Poisson inputs as feedforward excitatory drive with synaptic weight of 1nS. PV neurons were connected to PYR neurons with a fixed number of pre-synaptic partners: 100 PV to 1 PYR. We simulated synchronous sensory events by incorporating a delay between the correlated feedforward excitation and inhibition, similar to (*26*). This delay was set at 3ms with corresponding synaptic weights at 0.2 nS. Each PYR and PV neurons received projections from 1 SOM neuron driven by a Poisson process with variable rate. The synaptic weights were 15nS for PYR and 30nS for PV. The equations for the network dynamics of PYR are given by

$$\tau_m \frac{dV_i}{dt} = (V_{rest} - V_i) + g_{ext}(E_{exc} - V_i) + (g_{SOM+} + g_{PV+})(E_{inh} - V_i)$$

$$\tau_{exc}\frac{dg_{ext}}{dt} = -g_{ext} + w_{exc}S_{ext}(t)$$

$$\tau_{inh}\frac{dg_{PV+}}{dt} = -g_{PV+} + w_{inh}S_{PV+}(t)$$

$$\tau_{inh}\frac{dg_{SOM+}}{dt} = -g_{SOM+} + w_{inh}S_{SOM+}(t)$$

where $i \in [1 - 1{,}000]$, g_{ext}, g_{PV+} and g_{SOM+} are expressed in unit of leak conductances and S_{ext}, S_{PV+} and S_{SOM+} are synaptic inputs from pre-synaptic external sources as well as PV and SOM neurons impinging on the post-synaptic neuron i.

Duration of each simulation was 10s with time step dt = 0.1 ms. Simulations were performed using NEST simulator (*62*) and the PyNN interface(*63*).

Spike trains were binned at 100 ms segments before each averaged pairwise correlation coefficient was computed by averaging the correlations of 2500 neuron pairs randomly drawn from the PYR population.

2.7.2. Supplementary Figures

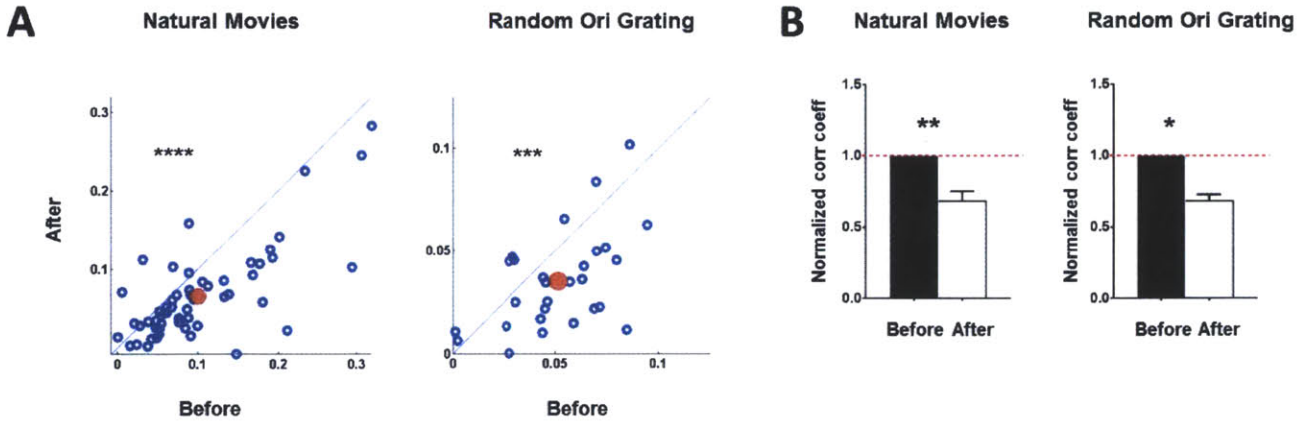

Fig. S1. *In vivo* optogenetic stimulation of ChAT-ChR2 expressing axons decreases correlation between responses of layer 2/3, V1 cortical neurons to both natural movies and random orientation gratings. **(A)** Scatter plot showing the between-cell correlation coefficients before and after ChAT-ChR2 stimulation when (***Left***) natural movies and (***Right***) random orientation gratings are shown. Each blue circle represents the averaged correlation coefficient between a single neuron and all other neurons in the same recording while the single red circle is the population averaged correlation coefficient. There is a significant decrease of between-cell correlation coefficient after ChAT-ChR2 stimulation in both natural movies ($p <<< 0.0001$, paired t-test) and random orientation grating experiments ($p < 0.001$, paired t-test). **(B)** ChAT-ChR2 stimulation induces significant decrease in population averaged normalized correlation coefficient across experiments in both natural movies ($P < 0.006$, paired t-test) and random orientation grating experiments ($P < 0.03$, paired t-test). * $P < 0.05$, ** $P<0.01$, *** $P<0.001$, **** $P<0.0001$.

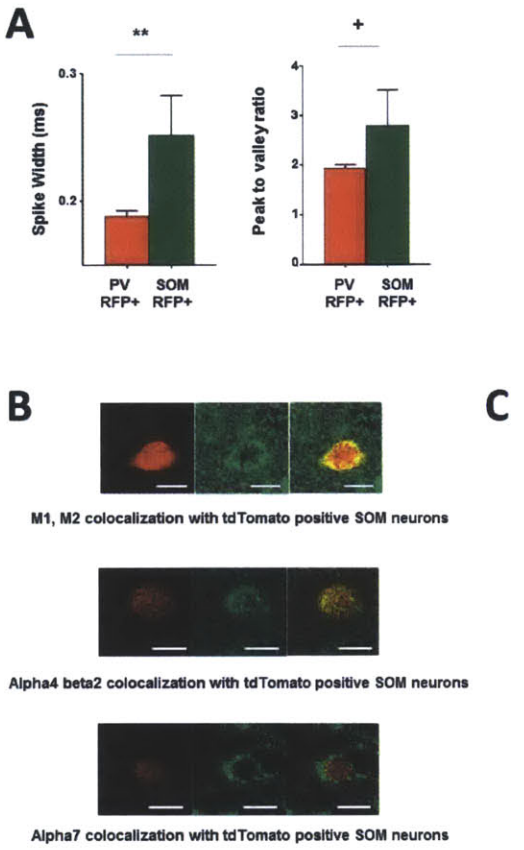

	All layers	Layer 2/3
mAChRs (m1,m2)	125/164 (76.2 %)	14/17 (82.4 %)
nAChRs (alpha-4, beta-2)	121/133 (91.0 %)	34/37 (91.9 %)
nAChRs (alpha-7)	142/172 (82.6 %)	29/40 (72.5 %)

Fig. S2. (A) Electrophysiological properties of SOM and PV neurons studied with cell attached recordings *in vivo* in ChAT-ChR2 SOM-cre-RFP and ChAT-ChR2 PV-cre-RFP animals (see Fig. 2). Population average of the (***Left***) mean spike half-width and (***Right***) mean peak to valley ratio of spike in the 24 PV and 11 SOM neurons recorded. ** $P < 0.007$, + $P = 0.0926$, t-test. Error bars indicate SEM. See (*30*). **(B)** Muscarinic (mAChR) and nicotinic (nAChR) receptors on tdTomato positive SOM neurons in V1 of SOM-TD mice. Immunohistochemistry (anti-mAChR M1/M2, anti-nAChR alpha4 and beta2, anti-nAChR alpha-7) showing co-localization of these receptors on SOM neurons. Scale bar, 10 μm. **(C)** Percentage co-localization of each set of cholinergic receptors with tdTomato positive SOM neurons in P34 fixed slices.

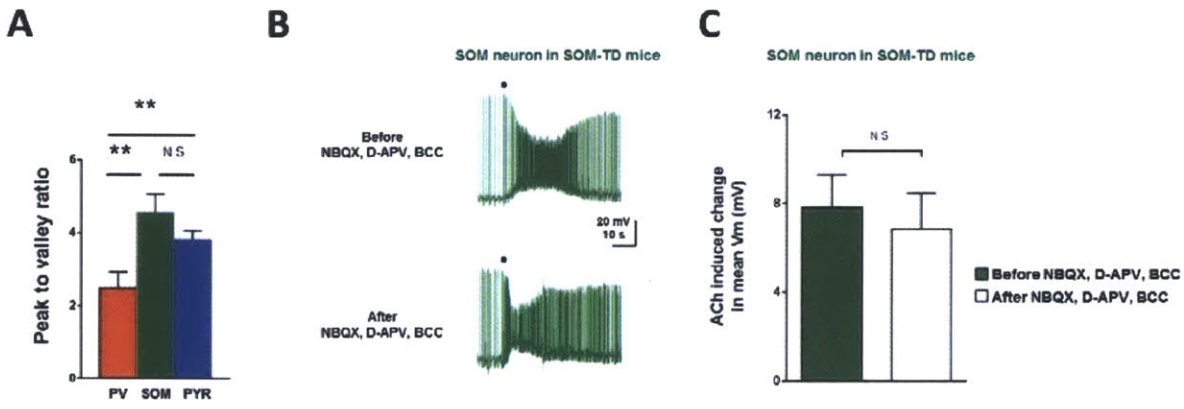

Fig. S3. (A) Population average of the mean peak to valley ratio of spikes of PV, SOM and PYR neurons studied with whole cell patch-clamp recordings *ex vivo* in PV-TD, SOM-TD and GAD-67-GFP/WT animals respectively ($P < 0.01$, Wilcoxon rank-sum test. See **Fig. 3**). Error bars indicate SEM. **(B)** Local ACh application (black dot; 10 mM, 200 ms, 20 psi) evokes a transient train of action potentials (AP) in SOM neurons (in SOM-TD slices) which persists in the presence of NBQX, D-APV and BCC. The change in spike height post ACh application is due to high firing rate. **(C)** Population average of ACh-induced changes in mean V_m of SOM neurons before and after bath application of NBQX, D-APV and BCC ($P > 0.4$, paired t-test). Error bars indicate SEM. ** $P<0.01$, N.S., not significant.

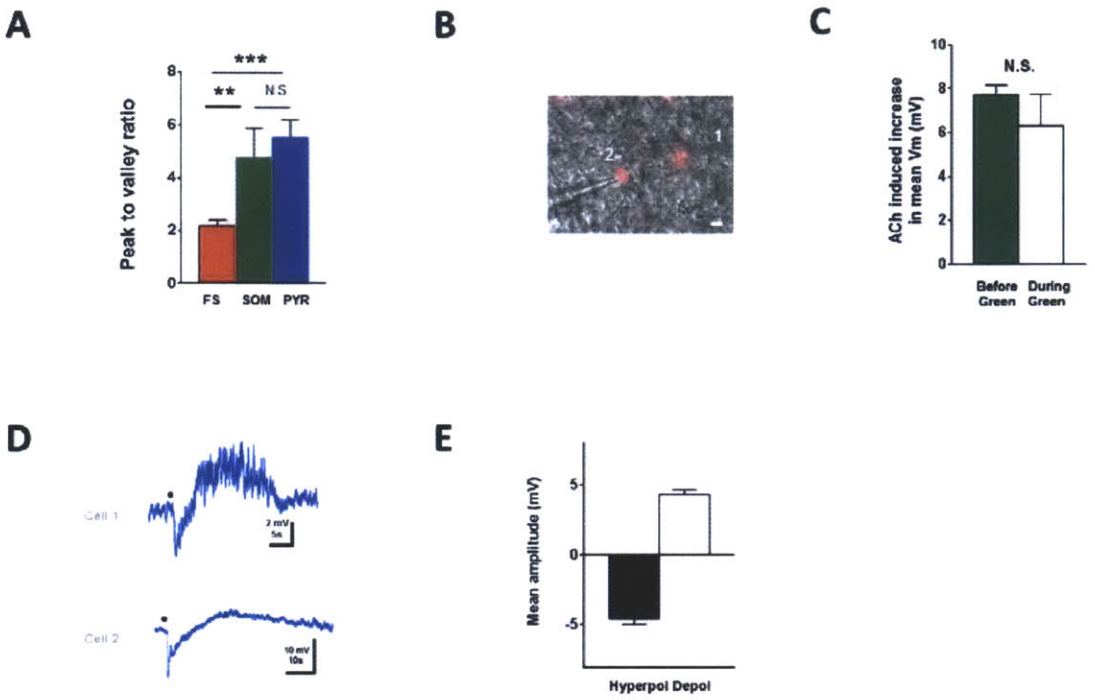

Fig. S4. (A) Population average of the mean peak to valley ratio of spikes in GFP-expressing SOM neurons and non GFP-expressing PYR neurons of SOM-cre-Arch-GFP animals as well as FS inhibitory neurons in GAD-67-GFP-SOM-cre-Arch animals studied with whole cell patch-clamp recordings *ex vivo.* (see Fig. 4). *** $P < 0.001$, ** $P < 0.01$, Wilcoxon rank-sum test. Error bars indicate SEM. **(B)** Merged fluorescence and DIC images of a SOM neuron patched in a SOM-TD slice. Relative positions of ACh pipette (1) and patch pipette (2) are as indicated. Scale bar, 10 μm. **(C)** Population average of ACh-induced changes in mean V_m of SOM neurons before and after green light exposure ($n = 3$, $P = 0.442$, paired t-test). Green light does not significantly change the ACh-induced response in SOM neurons in slices without Arch expression. **(D)** Local ACh application (black dot; 10 mM, 200 ms, 20 psi) evokes hyperpolarization followed by depolarization. Cells were recorded in current clamp mode. **(E)** Mean amplitude of the hyperpolarization and depolarization. ** $P<0.01$, *** $P<0.001$, N.S., not significant.

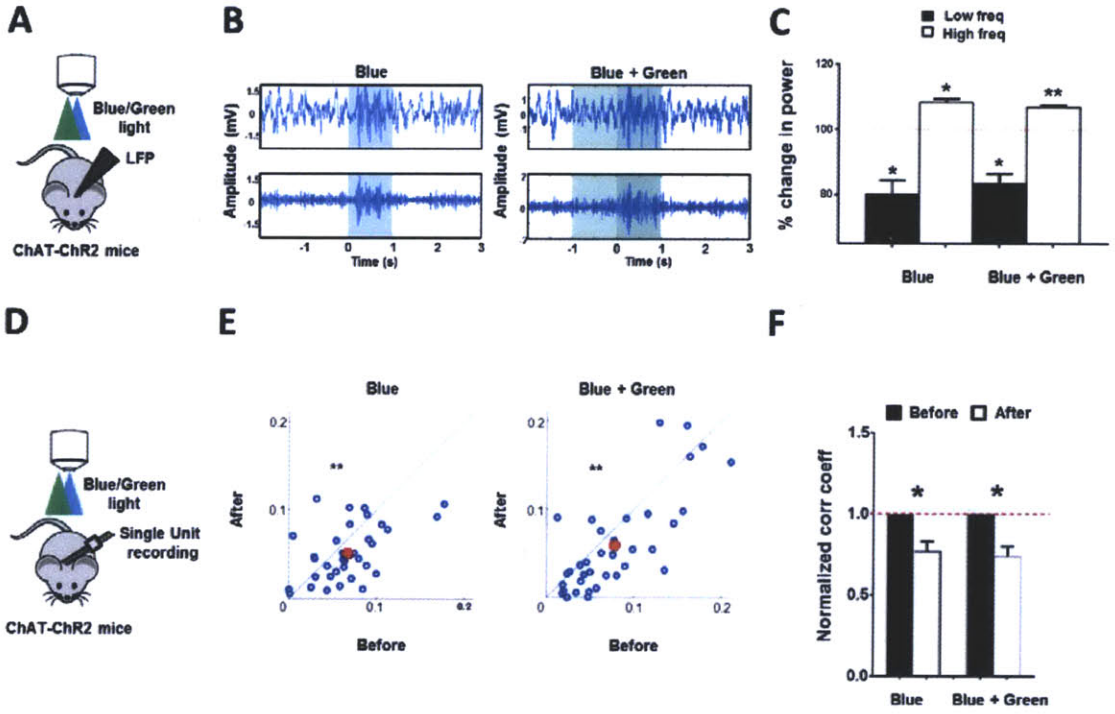

Fig. S5. Green light stimulation does not abolish the *in vivo* ChAT-ChR2 stimulation induced desynchronization of local field potential and neuronal decorrelation in ChAT-ChR2 animals without Arch expression. **(A)** Schematic illustration of the experimental setup for *in vivo* local field potential recording using a glass pipette during blue and blue/green stimulation of ChAT-ChR2 through objective. **(B)** Desynchronization of the local field potential during ChAT-ChR2 stimulation at t = 0 - 1 s (blue bar) (***Left***) is not blocked by green light stimulation during t = -1 – 1 s (green bar) (***Right***). The raw trace (***Top***) is band pass filtered at 5 – 100 Hz (***Bottom***). **(C)** ChAT-ChR2 blue light stimulation induces a % decrease in amplitude of low frequency events (<10 Hz, $P < 0.05$, paired t-test) and % increase in high frequency events (10 – 100 Hz, $P < 0.02$, paired t-test) respectively. This is not blocked during simultaneous green light and blue light stimulation in the ChAT-ChR2 control animals without Arch expression (low frequency: $P < 0.04$; high frequency: $P < 0.005$). **(D)** Schematic illustration of the experimental setup for *in vivo* single unit recording using a tungsten electrode array during blue and blue/green stimulation of ChAT-ChR2 through objective. **(E)** Scatter plot showing the between-cell correlation coefficients before and after ChAT-ChR2 blue light stimulation (***Top***) as well as before and after simultaneous ChAT-ChR2 blue and green light stimulation (***Bottom***) (Each blue circle represents the averaged correlation coefficient between a single neuron and all other neurons in the same recording while the single red circle is the population averaged correlation coefficient. There is a significant decrease of between-cell correlation coefficient during ChAT-ChR2 blue light stimulation ($p < 0.01$, paired t-test) and also duringChAT-ChR2 simultaneous blue and green light stimulation ($p < 0.005$, paired t-test). **(F)** There is a significant decrease in population averaged normalized correlation coefficient across experiments during ChAT-ChR2 blue light stimulation ($P < 0.04$, paired t-test) as well as during ChAT-ChR2 simultaneous blue and green light stimulation ($p < 0.03$, paired t-test). * $P < 0.05$, ** $P<0.01$.

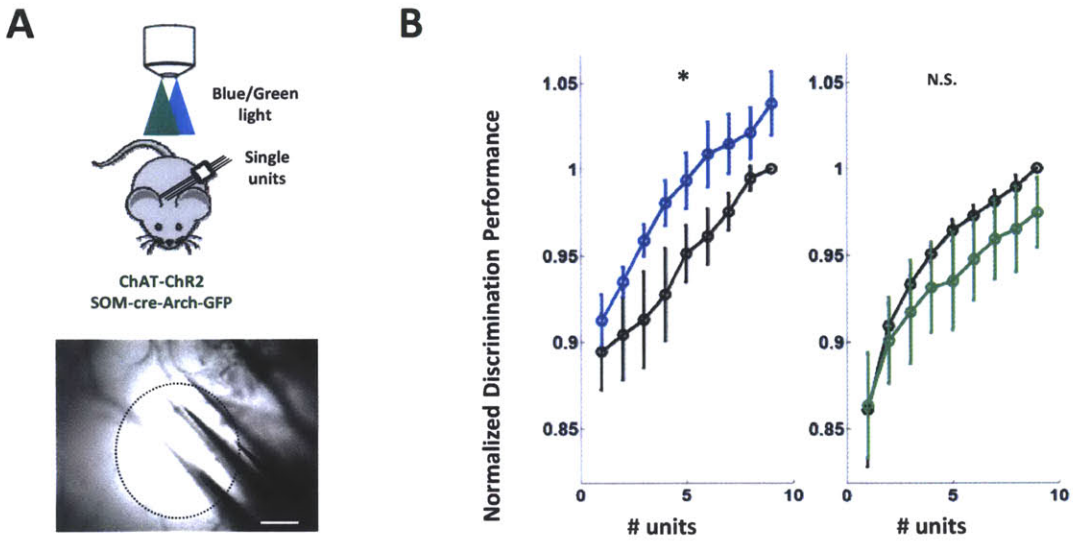

Fig. S6. *In vivo* ChAT-ChR2 stimulation enhances discrimination performance via SOM neurons. **(A)** (***Top***) Schematic illustration of the experimental setup for *in vivo* single unit recording using a tungsten electrode array during ChAT-ChR2 blue light stimulation and SOM-cre Arch green light stimulation through objective. (***Bottom***) Image of a tungsten electrode array used for single-unit recording in the Arch virus injected region in V1 in ChAT-ChR2-SOM-cre-Arch-GFP animals. Scale bar, 200 μm. **(B)** (***Left***) Normalized discrimination performance with (blue curve) and without (black curve) blue light stimulation. Discrimination performance was plotted as a function of number of units assessed for computation of population performance and normalized by the control performance at 9 units. Only data sets with more than 9 units were included. Performance improved with increased number of units assessed as well as with blue light stimulation (Two-way ANOVA: effect of number of units: $P < 0.03$, effect of light stimulation: $P < 0.04$, no significant interaction). (***Right***) Normalized discrimination performance with (green curve) and without (black curve) blue and green light stimulation. The effect of light stimulation is absent (Two-way ANOVA: effect of number of units: $P < 0.003$, effect of light stimulation: $P > 0.1$, no significant interaction). * $P<0.05$, N.S., not significant.

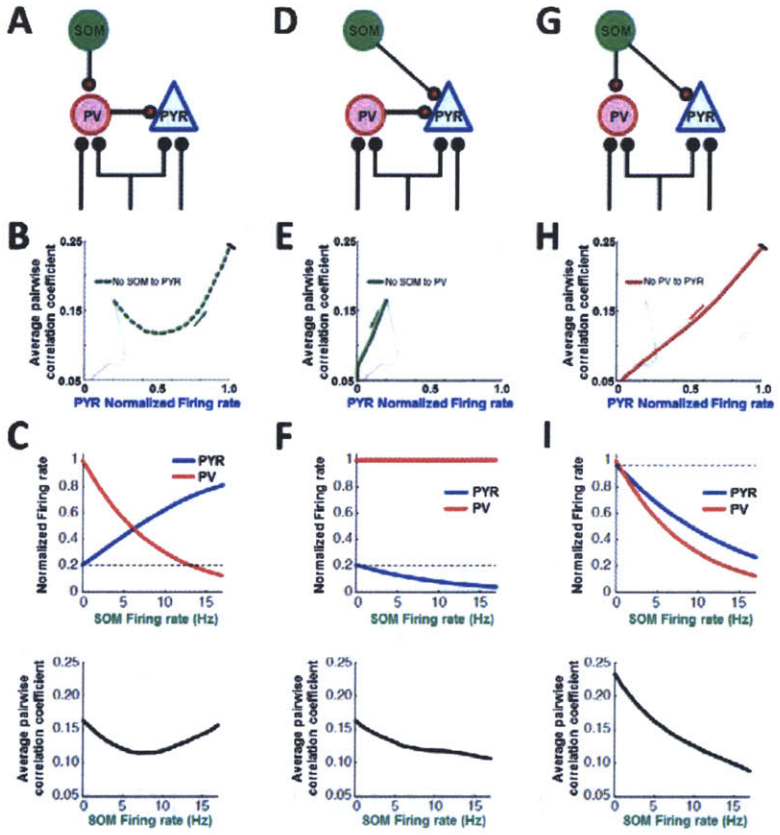

Fig. S7. Computational simulations show that each of the three connections in the microcircuit comprising SOM, PV and PYR are necessary for rate-independent neuronal decorrelation. **(A)** Schematic of the modeled circuit in Fig. 6 with the SOM-PYR connection removed. **(B)** Relationship between the averaged correlation coefficient with normalized firing rates of PYR neurons in the circuit of S7A. Arrow indicates direction of increasing SOM firing rate. **(C)** Relationship between the (***Top***) firing rates (Hz) of PYR and PV as well as (***Bottom***) the averaged correlation coefficient with varying SOM rates in the circuit of S7A. **(D)** Schematic of the modeled circuit in Fig. 6 with the SOM-PV connection removed. **(E)** Relationship between the averaged correlation coefficient with normalized firing rates of PYR neurons in the circuit of S7D. Arrow indicates direction of increasing SOM firing rate. **(F)** Relationship between the (***Top***) firing rates (Hz) of PYR and PV as well as (***Bottom***) the averaged correlation coefficient with varying SOM rates in the circuit of S7D. **(G)** Schematic of the modeled circuit in Fig. 6 with the PV-PYR connection removed. **(H)** Relationship between the averaged correlation coefficient with normalized firing rates of PYR neurons in the circuit of S7G. Arrow indicates direction of increasing SOM firing rate. **(I)** Relationship between the (***Top***) firing rates (Hz) of PYR and PV as well as (***Bottom***) the averaged correlation coefficient with varying SOM rates in the circuit of S7G.

Figure	# neurons	# slices	# animals	# neurons for washout
1D			5	
1G	85		9	
1H			9	
2C	11		6	
2F	23		4	
2I	85		9	
3D: meca	6	6	3	3
3D: atropine	5	5	2	3
3G: gabazine	5	5	2	5
3G: TTX	6	6	2	4
3G: meca	5	5	3	3
3G: atropine	5	5	3	2
3J: gabazine/BCC	22	22	7	18
3J: TTX	7	7	2	5
3J: meca	9	9	6	9
3J: atropine	11	11	3	11
4D	6	6	3	5
4G	6	6	3	3
4J	8	8	3	8
5C	8		4	
5F			3	
5I	49		5	
5J			5	

Table S1. Details of statistical comparisons made for Fig.1-5.

Figure	# neurons	# slices	# animals
Supp. 1A: Nat Mov	57		6
Supp. 1A: Grating	28		3
Supp. 1B: Nat Mov			6
Supp. 1B: Grating			3
Supp. 2A: PV	24		
Supp. 2A: SOM	11		
Supp. 3C	4	4	2
Supp. 4C	3	3	1
Supp. 4E	48		25
Supp. 5C			3
Supp. 5E	36		4
Supp. 5F			4
Supp. 6B			4

Table S2. Details of statistical comparisons made for Supplementary Fig.1-6.

2.8. References

1. C. A. Kitt, C. Höhmann, J. T. Coyle, D. L. Price, Cholinergic innervation of mouse forebrain structures. *The Journal of Comparative Neurology* 341, 117 (1994).
2. R. Metherate, C. Cox, J. Ashe, Cellular bases of neocortical activation: modulation of neural oscillations by the nucleus basalis and endogenous acetylcholine. *The Journal of Neuroscience* 12, 4701 (1992).
3. M. Goard, Y. Dan, Basal forebrain activation enhances cortical coding of natural scenes. *Nat Neurosci* 12, 1444 (2009).
4. A. Thiele, J. L. Herrero, C. Distler, K.-P. Hoffmann, Contribution of Cholinergic and GABAergic Mechanisms to Direction Tuning, Discriminability, Response Reliability, and Neuronal Rate Correlations in Macaque Middle Temporal Area. *The Journal of Neuroscience* 32, 16602 (November 21, 2012, 2012).
5. K. D. Harris, A. Thiele, Cortical state and attention. *Nature reviews. Neuroscience* 12, 509 (2011).
6. J. L. Herrero *et al.*, Acetylcholine contributes through muscarinic receptors to attentional modulation in V1. *Nature* 454, 1110 (2008).
7. J. F. Mitchell, K. A. Sundberg, J. H. Reynolds, Spatial Attention Decorrelates Intrinsic Activity Fluctuations in Macaque Area V4. *Neuron* 63, 879 (2009).
8. M. R. Cohen, J. H. R. Maunsell, Attention improves performance primarily by reducing interneuronal correlations. *Nat Neurosci* 12, 1594 (2009).
9. W. Singer, Synchronization of cortical activity and its putative role in information processing and learning. *Annual review of Physiology* 55, 349 (1993).
10. Jose L. Herrero, Marc A. Gieselmann, M. Sanayei, A. Thiele, Attention-Induced Variance and Noise Correlation Reduction in Macaque V1 Is Mediated by NMDA Receptors. *Neuron* 78, 729 (2013).
11. P. D. King, J. Zylberberg, M. R. DeWeese, Inhibitory Interneurons Decorrelate Excitatory Cells to Drive Sparse Code Formation in a Spiking Model of V1. *The Journal of Neuroscience* 33, 5475 (March 27, 2013, 2013).
12. J. De La Rocha, B. Doiron, K. J. Eric Shea-Brown, cacute, A. Reyes, Correlation between neural spike trains increases with firing rate. *Nature* 448, 802 (2007).
13. T. Klausberger, Brain-state- and cell-type-specific firing of hippocampal interneurons in vivo. *Nature* 421, 844 (2003, 2003).
14. J. A. Cardin *et al.*, Driving fast-spiking cells induces gamma rhythm and controls sensory responses. *Nature* 459, 663 (2009).
15. O. J. Avella Gonzalez *et al.*, External Drive to Inhibitory Cells Induces Alternating Episodes of High- and Low-Amplitude Oscillations. *PLoS Comput Biol* 8, e1002666 (2012).
16. S. Zhao *et al.*, Cell type–specific channelrhodopsin-2 transgenic mice for optogenetic dissection of neural circuitry function. *Nature methods* 8, 745 (2011).
17. A. Kalmbach, T. Hedrick, J. Waters, Selective optogenetic stimulation of cholinergic axons in neocortex. *Journal of Neurophysiology* 107, 2008 (April 1, 2012, 2012).
18. N. Chen *et al.*, Nucleus basalis-enabled stimulus-specific plasticity in the visual cortex is mediated by astrocytes. *Proceedings of the National Academy of Sciences*, (September 24, 2012, 2012).
19. B. Y. Chow *et al.*, High-performance genetically targetable optical neural silencing by proton pumps. (2010).

20. C. K. Pfeffer, M. Xue, M. He, Z. J. Huang, M. Scanziani, Inhibition of inhibition in visual cortex: the logic of connections between molecularly distinct interneurons. *Nature neuroscience*, (2013).
21. E. Fino, R. Yuste, Dense Inhibitory Connectivity in Neocortex. *Neuron* 69, 1188 (2011).
22. N. R. Wilson, C. A. Runyan, F. L. Wang, M. Sur, Division and subtraction by distinct cortical inhibitory networks in vivo. *Nature* 488, 343 (2012).
23. H. Barlow, Redundancy reduction revisited. *Network: computation in neural systems* 12, 241 (2001).
24. M. Okun, I. Lampl, Instantaneous correlation of excitation and inhibition during ongoing and sensory-evoked activities. *Nature neuroscience* 11, 535 (2008).
25. S. J. Cruikshank, T. J. Lewis, B. W. Connors, Synaptic basis for intense thalamocortical activation of feedforward inhibitory cells in neocortex. *Nature neuroscience* 10, 462 (2007).
26. J. Kremkow, L. U. Perrinet, G. S. Masson, A. Aertsen, Functional consequences of correlated excitatory and inhibitory conductances in cortical networks. *Journal of computational neuroscience* 28, 579 (2010).
27. A. Thiele, Optimizing brain processing. *Nature neuroscience* 12, 1359 (2009).
28. H. Adesnik, W. Bruns, H. Taniguchi, Z. J. Huang, M. Scanziani, A neural circuit for spatial summation in visual cortex. *Nature* 490, 226 (2012).
29. J. J. Letzkus *et al.*, A disinhibitory microcircuit for associative fear learning in the auditory cortex. *Nature* 480, 331 (2011).
30. W.-p. Ma *et al.*, Visual Representations by Cortical Somatostatin Inhibitory Neurons—Selective But with Weak and Delayed Responses. *The Journal of Neuroscience* 30, 14371 (October 27, 2010, 2010).
31. L. J. Gentet *et al.*, Unique functional properties of somatostatin-expressing GABAergic neurons in mouse barrel cortex. *Nature neuroscience* 15, 607 (2012).
32. F. Marrosu *et al.*, Microdialysis measurement of cortical and hippocampal acetylcholine release during sleep-wake cycle in freely moving cats. *Brain Research* 671, 329 (1995).
33. L. J. Gentet, M. Avermann, F. Matyas, J. F. Staiger, C. C. H. Petersen, Membrane Potential Dynamics of GABAergic Neurons in the Barrel Cortex of Behaving Mice. *Neuron* 65, 422 (2010).
34. J. F. A. Poulet, C. C. H. Petersen, Internal brain state regulates membrane potential synchrony in barrel cortex of behaving mice. *Nature* 454, 881 (2008).
35. T. Klausberger *et al.*, Brain-state-and cell-type-specific firing of hippocampal interneurons in vivo. *Nature* 421, 844 (2003).
36. A. Renart *et al.*, The Asynchronous State in Cortical Circuits. *Science* 327, 587 (January 29, 2010, 2010).
37. M. A. Gieselmann, A. Thiele, Comparison of spatial integration and surround suppression characteristics in spiking activity and the local field potential in macaque V1. *European Journal of Neuroscience* 28, 447 (2008).
38. M. J. Roberts *et al.*, Acetylcholine Dynamically Controls Spatial Integration in Marmoset Primary Visual Cortex. *Journal of Neurophysiology* 93, 2062 (April 1, 2005, 2005).
39. C. M. Mu¨ller, W. Singer, Acetylcholine-induced inhibition in the cat visual cortex is mediated by a GABAergic mechanism. *Brain Research* 487, 335 (1989).
40. K. Krnjević, R. Pumain, L. Renaud, The mechanism of excitation by acetylcholine in the cerebral cortex. *The Journal of Physiology* 215, 247 (1971).
41. H. Xu, H.-Y. Jeong, R. Tremblay, B. Rudy, Neocortical Somatostatin-Expressing GABAergic Interneurons Disinhibit the Thalamorecipient Layer 4. *Neuron* 77, 155 (2013).
42. Z. Xiang, J. R. Huguenard, D. A. Prince, Cholinergic Switching Within Neocortical Inhibitory Networks. *Science* 281, 985 (1998).

43. S. Arroyo, C. Bennett, D. Aziz, S. P. Brown, S. Hestrin, Prolonged Disynaptic Inhibition in the Cortex Mediated by Slow, Non-α7 Nicotinic Excitation of a Specific Subset of Cortical Interneurons. *The Journal of Neuroscience* 32, 3859 (March 14, 2012, 2012).
44. H. J. Alitto, Y. Dan, Cell-type-specific modulation of neocortical activity by basal forebrain input. *Frontiers in systems neuroscience* 6, (2012).
45. K. A. Buchanan, M. M. Petrovic, S. E. L. Chamberlain, N. V. Marrion, J. R. Mellor, Facilitation of Long-Term Potentiation by Muscarinic M1 Receptors Is Mediated by Inhibition of SK Channels. *Neuron* 68, 948 (2010).
46. A. J. Giessel, B. L. Sabatini, M1 Muscarinic Receptors Boost Synaptic Potentials and Calcium Influx in Dendritic Spines by Inhibiting Postsynaptic SK Channels. *Neuron* 68, 936 (2010).
47. J. T. Porter *et al.*, Selective excitation of subtypes of neocortical interneurons by nicotinic receptors. *The Journal of Neuroscience* 19, 5228 (1999).
48. N. R. Wilson, C. A. Runyan, F. L. Wang, M. Sur, Division and subtraction by distinct cortical inhibitory networks in vivo. *Nature* 488, 343 (2012).
49. C. A. Runyan *et al.*, Response Features of Parvalbumin-Expressing Interneurons Suggest Precise Roles for Subtypes of Inhibition in Visual Cortex. *Neuron* 67, 847 (2010).
50. S. J. Kuhlman, Z. J. Huang, High-resolution labeling and functional manipulation of specific neuron types in mouse brain by Cre-activated viral gene expression. *PLoS One* 3, e2005 (2008).
51. L. Madisen *et al.*, A robust and high-throughput Cre reporting and characterization system for the whole mouse brain. *Nature neuroscience* 13, 133 (2009).
52. N. Tamamaki *et al.*, Green fluorescent protein expression and colocalization with calretinin, parvalbumin, and somatostatin in the GAD67-GFP knock-in mouse. *The Journal of Comparative Neurology* 467, 60 (2003).
53. B. Y. Chow *et al.*, High-performance genetically targetable optical neural silencing by light-driven proton pumps. *Nature* 463, 98 (2010).
54. T. A. Pologruto, B. L. Sabatini, K. Svoboda, ScanImage: flexible software for operating laser scanning microscopes. *Biomed Eng Online* 2, 13 (2003).
55. S. Joshi, M. J. Hawken, Loose-patch-juxtacellular recording in vivo--A method for functional characterization and labeling of neurons in macaque V1. *Journal of Neuroscience Methods* 156, 37 (2006).
56. J. A. Cardin *et al.*, Targeted optogenetic stimulation and recording of neurons in vivo using cell-type-specific expression of Channelrhodopsin-2. *Nature protocols* 5, 247 (2010).
57. D. H. Brainard, The Psychophysics Toolbox. *Spatial Vision* 10, 433 (1997).
58. J. von Engelhardt, M. Eliava, A. H. Meyer, A. Rozov, H. Monyer, Functional Characterization of Intrinsic Cholinergic Interneurons in the Cortex. *The Journal of Neuroscience* 27, 5633 (May 23, 2007, 2007).
59. L. Tricoire, C. A. Cea-Del Rio, Illuminating Cholinergic Microcircuits in the Neocortex. *The Journal of Neuroscience* 27, 12119 (November 7, 2007, 2007).
60. J. DeFelipe, I. Fariñas, The pyramidal neuron of the cerebral cortex: Morphological and chemical characteristics of the synaptic inputs. *Progress in Neurobiology* 39, 563 (1992).
61. B. W. Connors, M. J. Gutnick, Intrinsic firing patterns of diverse neocortical neurons. *Trends in Neurosciences* 13, 99 (1990).
62. M. Diesmann, M.-O. Gewaltig, NEST: An environment for neural systems simulations. *Forschung und wisschenschaftliches Rechnen, Beiträge zum Heinz-Billing-Preis* 58, 43 (2001).
63. A. Davison, P. Yger, J. Kremkow, L. Perrinet, E. Muller, PyNN: towards a universal neural simulator API in Python. *BMC Neuroscience* 8, P2 (2007).

Chapter 3: Cholinergic activation of astrocytes mediates nucleus basalis-enabled stimulus-specific plasticity in the visual cortex

Naiyan Chen*, Hiroki Sugihara*,
Jitendra Sharma, Gertrudis Perea, Jeremy Petravicz, Chuong Le, Mriganka Sur †

* Equal contribution

This chapter is presented as it appeared in publication, which can be found in the October 9 2012 issue of **Proc. Natl. Acad. Sci.** USA. Slight modifications are made.

N.C., H.S., and M.S. designed research;
N.C., H.S., conducted *in vivo* experiments; N.C., G.P. conducted *ex vivo* experiments;
N.C., H.S. and G.P. analyzed data;
J.S. provided technical advice and C.L. provided technical assistance;
J.P. contributed new transgenic mice;
N.C. and M.S. wrote the paper.

Chapter 3: Cholinergic activation of astrocytes mediates nucleus basalis-enabled stimulus-specific plasticity in the visual cortex

Although cholinergic innervation of the cortex by the nucleus basalis (NB) is known to modulate cortical neuronal responses and instruct cortical plasticity, little is known about the underlying cellular mechanisms. Using cell-attached recordings *in vivo*, we demonstrate that electrical stimulation of NB, paired with visual stimulation, can induce significant potentiation of visual responses in excitatory neurons of the primary visual cortex (V1) in mice. We further show with *in vivo* two-photon calcium imaging, *ex vivo* calcium imaging and whole–cell recordings that this pairing induced potentiation is mediated by direct cholinergic activation of V1 astrocytes via muscarinic acetylcholine receptors (mAChRs). The potentiation is absent in IP_3R2-cKO mice which lack astrocyte calcium activation, and is stimulus specific, as pairing NB stimulation with a specific visual orientation reveals a highly selective potentiation of responses to the paired orientation compared to unpaired orientations. Collectively, these findings reveal a novel and surprising role for astrocytes in NB-induced stimulus specific plasticity in the cerebral cortex.

3.1. Introduction

Sensory experience associated with nucleus basalis (NB) driven, cholinergic activation of the cortex (*1*) has been shown to induce cortical plasticity at both single cell and cortical map levels (*2-6*). To understand how cortical responses and representations can be altered by experience during cholinergic modulation, it is critical to identify the circuit elements involved and define how their interactions can contribute to the restructuring of cortical network dynamics.

Previous studies have shown that multiple cortical cell types including neurons (*7-9*) and astrocytes (*10-12*) can be responsive to acetylcholine (ACh). Among these cell-types, astrocytes are a promising candidate for contributing to NB-mediated cortical plasticity: *ex vivo* studies have implicated hippocampal astrocytes in synaptic potentiation [(*13-15*) but see (*16*)], demonstrating that they can potentially provide a powerful means of altering the state of neuronal networks to induce plasticity. More recently, studies using combined somatosensory and cholinergic stimulation have revealed that NB-induced astrocytic activation can induce potentiation of local field potentials recorded in somatosensory cortex (*17, 18*). These findings open up several key questions: Does the NB-mediated potentiation manifest at the level of single neurons and astrocytes? If so, does the potentiation influence specific features of single neuronal responses and representations? Particularly, is the potentiation a non-specific increase in responses that is independent of sensory stimulus features, or does it selectively facilitate responses to stimuli that have been paired with NB stimulation?

The primary visual cortex (V1) provides an excellent model system to address these issues. Modulation by ACh in general, and cholinergic drive from the NB in particular, is known to influence V1 circuits in multiple ways, resulting in enhancement of direction and orientation selectivity in V1 neurons (*19-22*), increase in attentional modulation of V1 neurons in behaving monkeys (*23*), and alteration in the reliability and synchrony of stimulus-evoked spikes in V1 neurons (*24*). Responses of mature V1 neurons to specific visual stimulus features have also been shown to be plastic and depend on the history of visual stimulation (*25*). Moreover, cortical astrocytes have been previously demonstrated to be an integral component of V1 circuits as they are visually responsive and are capable of modulating visually-driven neuronal responses (*26*). We therefore examined the influence of NB-mediated cholinergic activation of astrocytes and neurons in mouse V1 *in vivo*, and the mechanisms of their interactions in V1 slices *ex vivo*, using both calcium imaging and electrophysiological recording. We show for the first time that pairing electrical stimulation of the NB with visual stimuli can induce potentiation of visual responses in V1 excitatory neurons. The potentiation is facilitated by astrocytes which are activated by cholinergic inputs from the NB and in turn directly influence neuronal responses, and is abolished in mice which lack astrocyte calcium increases due to deletion of astrocytic inositol 1,4,5 trisphosphate receptor type 2 (IP_3R2). This astrocyte-mediated response potentiation is stimulus specific, as pairing one stimulus orientation with NB stimulation selectively potentiates the visual response of the paired over other unpaired orientations.

3.2. Results

3.2.1. Pairing NB and visual stimulation potentiates visual responses in excitatory neurons *in vivo*

We first investigated if paired NB and visual stimulation can induce potentiation of identified excitatory neuron responses. The NB was stimulated with an implanted bipolar electrode (see SI Materials and Methods: *In vivo* surgery) (*24*) while responses of single visual cortical neurons in the supragranular layers were recorded with *in vivo* cell-attached recordings (**Fig. 1*A* and 1*D***, top). The stereotaxic accuracy of the implantation was determined by (a) localization of the electrode tip within NB as assessed by acetylcholinesterase staining (**Fig. 1*B***) (*24*) and (b) the effect of stimulation on desynchronization of the interhemispheric electroencephalogram (**Fig. 1*C***) (*24, 27*). Excitatory neurons were characterized by their 'regular spiking' properties (*28*), including spike half widths and peak-to-valley ratios (**Fig. S1*A-B***) and their responses before, during and after the pairing paradigm were recorded at single-spike resolution for long durations. The visual stimuli consisted of gratings of random orientation designed to evoke robust responses and were presented alternately with blank gray screens (**Fig. 1*D***, bottom, see SI Materials and Methods: *Visual Stimulation*). Stimulating the NB with multiple trains of pulses, where each train (50 pulses at 100 Hz; see SI Materials and Methods: NB stimulation) was paired with each cycle of visual stimulus (**Fig. 1D,** bottom), induced a prominent sustained slow potentiation of visual responses in excitatory neurons lasting over 40 minutes (**Fig. 1*E-F***). The firing rates during the alternate visual stimulus and blank gray screen presentations were quantified as ON and OFF responses respectively, while the ON responses relative to the preceding OFF responses were quantified as ON–OFF. The increase was pronounced in both

visual ON and ON-OFF responses (**Fig. 1*F*:** n= 6 neurons in 6 animals, P <<<0.001). Thus, paired NB and visual stimulation reliably potentiates visually driven responses of regular spiking, presumably pyramidal V1 neurons.

3.2.2. *In vivo* NB stimulation evoke robust calcium responses in visual cortical astrocytes via muscarinic receptors

We next investigated if NB stimulation can activate V1 astrocytes using *in vivo* two-photon imaging (**Fig. 2*A***, left). V1 astrocytes and neurons were loaded with fluorescent calcium indicator Oregon Green 488 Bapta-1-AM (OGB1-AM), while astrocytes were loaded with the selective astrocytic marker sulforhodamine101 (SR101) (*29*) (**Fig. 2*A***, right). OGB1-AM fluorescence in astrocytes was monitored continuously with two-photon imaging during NB stimulation. First, we examined whether spontaneous activity in astrocytes was affected by a brief train of pulses applied to NB (50 pulses at 100 Hz). Indeed, we observed robust increases in the calcium responses of astrocytes (**Fig. 2*B***, left; n = 30/44 astrocytes in 5 animals, P < 0.0001, paired t-test, comparing population, trial-averaged responses before and after brief NB stimulation). When atropine, a mAChR antagonist, was delivered by a visualized pipette (**Fig. 2*A***, right), NB-evoked responses were reduced to pre-NB levels (**Fig. 2*B***, right; **Fig. 2*C***; n = 17 NB stimulation facilitated astrocytes in 3 animals, P = 0.001, paired t-test, comparing responses before and after NB stimulation; P < 0.001, paired t-test, comparing NB evoked responses before and after atropine application, **Fig. S2*A***). Thus, responses of cortical astrocytes to NB stimulation are evoked by cholinergic modulation via mAChRs.

To examine how NB activation influenced visual responses of astrocytes, we presented randomly oriented visual gratings synchronized to a single, brief train of pulses applied to NB (**Fig. 2*D***) while imaging astrocyte responses. Indeed, visual responses of astrocytes were enhanced by NB stimulation (**Fig. 2*E* and 2*F***: n = 47 visually responsive astrocytes in 5 animals, $P < 0.01$, paired t-test, comparing population average of visual responses pre- and post-NB, **Fig. S2*B***), showing that V1 cortical astrocytes are capable of integrating visual and cholinergic inputs.

3.2.3. ACh stimulation in V1 slices evokes calcium responses in astrocytes via muscarinic receptors

To examine the mechanisms underlying NB-evoked responses in astrocytes, we performed calcium imaging of astrocytes in slices of V1. Responses of OGB1-AM loaded layer 2/3 astrocytes were imaged (**Fig. 2*G***) before and after ACh application. Imaged astrocytes had small round somas with thin radiating processes revealed by OGB1-AM loading (**Fig. 2*H***, top left). The identity of the imaged astrocytes was further confirmed by co-localization of their dye-filled processes (**Fig. 2*H***, top right) with anti-GFAP immunohistochemistry (**Fig. 2*H***, bottom left) and with the astrocyte-selective marker SR101 (*29*) in selected experiments (**Fig. 2*H***. bottom right). To mimic brief NB stimulation, we applied a brief pulse (0.2 – 1s) of ACh, which evoked robust calcium transients in astrocytes (**Fig. 2*I***, top). These responses were TTX-insensitive (**Fig. 2*I***), and were abolished by the mAChR antagonist scopolamine and atropine (**Fig. 2*I***, bottom, and **Fig. 2*J***: n = 8 astrocytes in 3 animals; P = 0.0001, paired t-test). Immunohistochemistry confirmed that mAChRs were expressed on GFAP-expressing astrocytes (**Fig. S3*A-B***). To mimic prolonged NB stimulation, we bath-applied ACh, which caused an increase in the frequency and duration of calcium transients lasting for several minutes (**Fig. S3*C-F***). These

findings, together with *in vivo* results (Fig. 2A-F), indicate that V1 astrocytes are direct targets of NB stimulation-evoked cholinergic modulation via mAChRs (*10, 11*), and have calcium responses of different time scales dependent on the mode of ACh application, independently of neuronal action potentials.

3.2.4. Cholinergic activation of astrocytes contributes to prolonged depolarizing responses in excitatory neurons via calcium-mediated processes

The NB and ACh induced astrocyte responses suggested that the sustained slow potentiation of excitatory neuronal responses following paired NB and visual stimulation (Fig. 1D-F) could be a contribution by astrocytes to neuronal plasticity, based on previous evidence that hippocampal astrocytes play a role in synaptic plasticity (*13-15*) and facilitate neuronal responses via gliotransmitter release (*30, 31*) or regulation of glutamate uptake (*32*).

We first tested the hypothesis that cholinergic activation of astrocytes can contribute to cholinergic facilitation of neuronal responses by performing whole-cell patch recordings in V1 slices (**Fig. 3*A***). Excitatory neurons were identified by their electrophysiological regular-spiking and morphological characteristics and responded to a brief pulse of ACh with a slow, prolonged depolarization (**Fig. 3*E***, ***F***, ***G***, top, n = 50/50 neurons) which is TTX-insensitive (**Fig. S4,** n = 10, P>0.9, paired t-test). We examined the mechanisms behind the ACh-induced slow depolarization further by blocking calcium responses in astrocytes (**Fig. 3*A***). Astrocytic calcium was chelated through patch-loading electrophysiologically-characterized astrocytes (**Fig. 3*B***) with the cell impermeable calcium chelator BAPTA and allowing BAPTA to travel within the local syncytium of astrocytes via gap junctions (*33, 34*). The spread of BAPTA was assessed by Alexa

Fluor 594 (A594) dye included in the patch pipette and determined to be approximately 150 μm from the patched astrocyte within 30 – 45 min of dialysis (**Fig. 3*C***). BAPTA effectively blocked ACh-induced calcium transients in the dialyzed astrocytes (**Fig. 3*D***). Excitatory neurons within 100 μm of the patched astrocytes (**Fig. 3*C***) were recorded after BAPTA dialysis. The amplitude of the ACh-induced slow depolarization in neurons within the dialyzed astrocytic network was reduced as compared to that in control conditions (**Fig. 3*E***), either without astrocyte patch ($n = 9$ neurons, $P < 0.001$, t-test) or in the presence of astrocytes dialyzed with A594 without BAPTA ($n = 9$ neurons, $P < 0.0001$, t-test) (**Fig. 3*H***). The slow neuronal depolarizations were mediated by mAChRs as they were abolished by atropine (**Fig. 3*F* and 3*I*** – atropine: $n = 18$ neurons in 13 animals, $P < 0.001$, paired t-test), consistent with our previous demonstration that ACh-induced astrocyte calcium transients were mAChR-mediated (**Fig. 2*B-C* and 2*I-J***). These data therefore demonstrate that cholinergic activation of astrocytes can contribute to cholinergic facilitation of mAChR-mediated neuronal responses via increase of intracellular calcium.

3.2.5. Cholinergic activation of astrocytes evokes slow NMDAR-mediated currents in neurons

Earlier work has demonstrated that gliotransmitters released by astrocytes can act on the NR1/NR2B subunits of NMDARs in the extrasynaptic membranes of neurons (*35, 36*). These subunits have slow kinetics (*37-39*) and have been proposed to give rise to slow currents observed in neurons when adjacent astrocytes are activated (*12, 36, 40*) . To investigate if NMDA-mediated currents underlie the astrocyte-evoked cholinergic responses in neurons, we performed whole-cell voltage clamp recordings where slow currents were defined and

discriminated from miniature EPSCs (mEPSCs) by their differential time-courses (**Fig. 4*A-C*, Fig. S5*A-B*,** see SI Materials and Methods: *Analysis of slow currents*). Indeed, ACh induced an increase in the frequency of TTX-insensitive slow currents (**Fig. 4*D-F***, top; **Fig. 4*G*, Table S1, Fig. S5*C***: n = 18 neurons in 9 animals, $P < 0.0001$, paired t-test). These ACh-induced slow currents were atropine-sensitive (**Fig. 4*E*; Fig. 4*G*, Table S1**: n = 10 neurons in 5 animals, $P < 0.02$, paired t-test comparing ACh-induced slow current frequency before and after atropine application). To investigate if these currents have an astrocytic origin, double-patch experiments were performed where a pyramidal neuron was patched and a neighboring astrocyte contacted with a BAPTA-containing patch pipette in cell-attached configuration, keeping the membrane intact to prevent BAPTA diffusion into the astrocyte. ACh-induced slow currents in the pyramidal neurons were first recorded before the seal between the astrocyte and BAPTA containing patch pipette was broken to allow BAPTA dialysis of the astrocyte syncytium. After 30 – 45 min of BAPTA dialysis, a reduction of ACh-induced slow currents was observed (**Fig. 4*D***, bottom; **Fig. 4*G*, Table S1**: n = 5 neurons in 4 animals, $P < 0.006$, paired t-test comparing ACh-induced slow current frequency before and after BAPTA dialysis of astrocytes). In a similar set of experiments where excitatory neurons were patched after astrocytic BAPTA dialysis, we also observed a reduction in the frequency of ACh-induced slow currents (**Fig. S5*C***: $P <<< 0.001$, t-test comparing ACh-induced slow current frequency without [n=18 neurons] and with [n=11 neurons] BAPTA dialysis of astrocytes). The reduction of slow currents was further confirmed not to be due to the extracellular action of BAPTA (**Fig. S5*D***). Both the ACh-induced slow currents and slow depolarizations in neurons were mediated by NMDARs as they were reduced in the presence of D-APV (***Slow currents:* Fig. 4*F*; Fig. 4*G*, Table S1**: n = 10 in 7 animals, $P = 0.0001$, paired t-test comparing ACh-induced slow current frequency before and after D-APV

application; ***Slow depolarization:*** **Fig. 3*G***; **Fig. 3*I***: n = 8 neurons in 8 animals, $P < 0.003$, paired t-test). While we cannot determine the causal relationship between the ACh-induced slow currents and slow depolarization, their similar insensitivity to TTX (**Fig. S4, Fig. 4*D-F***) and similar sensitivity to BAPTA dialysis, D-APV and atropine (**Fig. 3*E-I*, Fig. 4*D-G***) as well as comparable durations (mean duration of slow depolarization = 76.6 ± 10.25s, n = 24; duration of increase in slow current frequency = 60 – 120s, n = 13, **Fig. 4*D-F***, top) and long peak and valley latency (**Fig. 3*E*, 4*A-B*, 4*D***) suggest a correlation between the two phenomena. Considering the low slow current frequency, it is possible that the depolarization of the cellular membrane induced by these slow currents favors the development of ACh-induced prolonged depolarization. Collectively, these findings indicate that cholinergic excitation of astrocytes via mAChRs leads to calcium-mediated processes that in turn evoke NMDAR mediated facilitatory responses including the neuronal slow currents and slow depolarization.

3.2.6. Astrocytic IP_3R2-mediated calcium mediates NB stimulation-evoked potentiation of visual responses in excitatory neurons

We next investigated if cholinergic activation of astrocytes can contribute to the NB mediated potentiation of visual responses in excitatory neurons observed *in vivo* (Figure 1E, F). For this purpose, we used conditional IP_3R2 knockout mice (IP_3R2-cKO) (**Fig. S6**, SI Materials and Methods: Mice) where the astrocytic inositol 1,4,5 trisphosphate receptor type 2 (IP_3R2), previously shown to be the only IP_3R (*41*) that mediates agonist-induced calcium responses in astrocytes (*33, 42*), is specifically knocked out in GFAP-expressing astrocytes (**Fig. 5A:** Fractions (%) of GFAP-expressing cortical astrocytes that co-localize with IP_3R2 in WT and IP_3R2-cKO are 77/80 astrocytes (96.3%) and 7/90 astrocytes (7.8%) respectively). [Since the

evidence for IP_3R2 expression in neurons remains inconclusive (*41, 42*), the conditional IP_3R2 knockout mice were used instead of the full IP_3R2 knockout mice]. We first performed calcium imaging (**Fig. 2*G***) in V1 slices of adult IP_3R2-cKO and WT (control) animals. While ACh induced calcium responses in astrocytes of WT mice, no astrocytic calcium responses were observed in the IP_3R2-cKO mice (**Fig. 5*B***). We next performed whole-cell patch recordings in V1 slices of adult IP_3R2-cKO and WT animals. The amplitude of the ACh-induced slow depolarization in IP_3R2-cKO regular spiking neurons was indeed drastically reduced as compared to that in WT (**Fig. 5*C***: n = 5 WT and n = 5 IP_3R2-cKO neurons in 2 animals each, $P < 0.001$, t-test). When the NB was stimulated with multiple trains of pulses where each train was paired with visual stimulation in the IP_3R2-cKO animals *in vivo*, using the same protocol/analysis as in WT animals (**Fig. 1*D***), no sustained potentiation was observed (**Fig. 5*D***: n=5 neurons in 4 animals, $P > 0.1$, paired t-test comparing pre-NB responses to post-NB responses pooled across all 400s time segments for ON, ON-OFF and OFF responses). The neurons in the IP_3R2-cKO animals had similar electrophysiological properties as the WTs (**Fig. S7**) and therefore the lack of sustained potentiation in the IP_3R2-cKO animals cannot be attributed to unintended secondary effects due to abnormal electrophysiology in the transgenic mice. These data therefore confirm that astrocytic IP_3R2-mediated calcium plays a significant role in the potentiation of visual responses in excitatory neurons following prolonged pairing of NB and visual stimulation.

3.2.7. NB-induced cholinergic activation of astrocytes contributes to potentiation of stimulus- specific responses

The NB stimulation-evoked, astrocyte-mediated potentiation of visual responses could be a general increase in neuronal responsiveness such that responses to any visual stimulus are indiscriminately enhanced, or it could reflect a specific facilitation of particular visual stimuli. To discriminate between these possibilities, we paired NB stimulation with visual gratings of a specific orientation while performing single unit recordings from neuronal populations (**Fig. 6*A***) in both WT and IP_3R2-cKO mice. Responses to 9 orientations each 20 degrees apart, including an arbitrarily chosen orientation for the paired NB and visual orientation stimulation (conditioned orientation), were measured before and after the pairing protocol. Blank gray screens were interleaved between each orientation presentation. We observed an increase in the firing rates (**Fig. 6*B***) as well as in normalized post minus pre responses at the conditioned orientation in WT animals (ON-OFF responses shown in **Fig. 6*C*, *left*, Fig. 6*D*, *top***: n=41 neurons, $P < 0.001$, Wilcoxon rank-sum test comparing responses before and after pairing protocol; ON responses shown in **Fig. S8*A*, *C*, *top***: $P< 0.001$, Wilcoxon rank-sum test comparing responses before and after pairing protocol). Interestingly, this increase was specific to the conditioned orientation as the facilitation at the conditioned orientation was significantly greater than at unconditioned orientations, with the latter showing no change in response (**Fig. 6*B***, **Fig. 6*C*, *left*, Fig. 6D; Fig. S8A, C**). Recovery of this facilitation was observed earlier (**Fig. S8*D***) than when NB stimulation was paired with random orientations (**Fig. 1F**), possibly due to reversal of synaptic modifications (*43*) induced by exposure to orientations other than the conditioned orientation after the pairing protocol (during assays of the post-conditioning effects). In sum, these findings demonstrate that pairing NB stimulation with a specific visual orientation

induces a highly specific potentiation of the conditioned orientation over unconditioned orientations in WT animals.

In the IP_3R2-cKO animals, no potentiation at the conditioned orientation was observed after the pairing protocol. Instead, a slight response depression was surprisingly revealed (**Fig. 6*B***, **Fig. 6*C*, *left***, **Fig. 6*D*, *top***, **Fig. S8*A*, S8*C*, *top***). The population mean conditioned minus unconditioned response in the IP_3R2-cKO mice showed a reversal in sign of conditioned responses, in marked contrast to the findings in the WT experiments (**Fig. 6*C*, *right***, **Fig. S8*B***: $P<0.0001$ comparing mean differential ON –OFF and ON response in WT and IP_3R2-cKO paired experiments, n=41 WT neurons, 45 IP_3R2-cKO neurons).

In additional control experiments where the same visual stimuli were presented without NB stimulation (visual only experiments), a similar reversal in sign of conditioned responses was observed (**Fig. 6*C***, **6*D***, **Fig. S8*A*-*C***: $P<0.0001$ comparing mean differential responses, both ON–OFF and ON, between WT paired and visual only experiments). Visual only responses in WT and IP_3R2-cKO animals were similar (**Fig. S8*E***). Conditioned responses were depressed to similar extents in the visual only experiments, as well as in the IP_3R2 KO paired experiments (**Fig. 6C, *right*, Fig. S8B, Fig. S8E**, $P > 0.05$ for each comparison). Collectively, these findings show that the potentiation observed at the conditioned orientation requires both NB activation and intact astrocytic IP_3R2-mediated calcium elevation. The absence of either of these two factors changes the sign of conditioned responses, indicating that by itself the prolonged orientation-specific visual stimulation in the training protocol induces cortical response suppression, likely via adaptation mechanisms that have been previously shown to be reliably evoked by similar prolonged orientation-specific stimulation (*25*). [This phenomenon is absent in the IP_3R2-cKO responses measured in Fig. 5D likely because the random orientation gratings

used for pairing constitute a rapid presentation of drifting gratings of multiple orientations and thus do not induce orientation-specific adaptation]. The presence of NB stimulation paired with single orientation stimulation, however, decisively counters this adaptation-induced suppression in WT animals but not in IP3R2-KO animals. In sum, these data show that astrocyte calcium can mediate an NB-evoked stimulus-specific potentiation of V1 neuron responses that over-rides adaptation-induced response suppression in these neurons.

3.3. Discussion

We have demonstrated for the first time that repeated NB stimulation paired with visual stimulation *in vivo* leads to prolonged potentiation of visual responses in V1 excitatory neurons. Previous work in rat auditory cortex has shown that NB stimulation paired with an auditory stimulus leads to significant cortical plasticity exemplified by changes in receptive fields (*2, 6*) and reorganization of cortical maps (*3-5*). Our work extends these findings by revealing the critical role of astrocytes in mediating this NB-induced cortical plasticity through their direct activation by cholinergic modulation via muscarinic receptors. It is possible that these activated astrocytes are involved in the initial induction of the cortical plasticity which triggers structural changes that can contribute to the subsequent prolonged facilitatory responses in neurons. Although we cannot rule out a direct facilitatory effect of NB stimulation on pyramidal neurons, the predominant contribution to the potentiation in neurons seems to be from an astrocytic calcium-driven mechanism, since removal of IP_3R2-mediated astrocytic calcium blocks NB-induced potentiation *in vivo* while chelation of intracellular astrocytic calcium abolishes ACh-induced neuronal depolarization and slow currents *ex vivo*.

Recent reports using combined somatosensory and cholinergic stimulation have shown that cholinergic-activated astrocytes can induce synaptic plasticity (*17, 18*). Yet, it remained unknown if this plasticity reflects a general increase of cortical responsiveness or a more specific potentiation at the stimulus and circuit level. Using visual cortex as a model system together with cell-attached and single unit recordings, we were able to apply a more refined stimulus protocol and address the question at a single-cell level. We find that the astrocyte-mediated potentiation is indeed stimulus specific as pairing a grating of a particular orientation with NB stimulation induces a highly specific increase in responses to the paired orientation but not to unpaired orientations. There are several possible mechanisms that can mediate this stimulus-specific potentiation. Since individual synapses on superficial layer V1 neurons convey specific orientation information (*44*), astrocytes can contribute to the potentiation through non-specific release of glutamate to the extracellular matrix. However, matched response features of V1 neurons and their adjacent astrocytes in earlier studies (*26*) have also suggested stimulus-specific activation of astrocytes. It has also recently been revealed that astrocytic processes can exhibit intense activity (*33*), which may support the hypothesis of intimate organization of astrocytic processes that can locally modulate neuronal synapses to convey and generate orientation specific responses.

The generation and plasticity of orientation-selective responses in V1 requires both feedforward inputs from the thalamus and recurrent inputs within the cortex (*45, 46*) and can be powerfully altered by top-down influences (*47*). NB inputs have also been implicated in top-down processes including attention (*23*). Our findings indicate that astrocyte-mediated mechanisms, potentially through astrocytic calcium dependent release of gliotransmitters that act on neuronal NMDARs,

can induce a plasticity cascade in synapses and alter orientation specific responses. Candidate ligands include glutamate (*36*) or D-serine ((*15*) but see (*48*)). Alternatively, the potentiation can be mediated by astrocytic calcium-dependent regulation of extracellular glutamate (*26*) or extracellular potassium (*49*) which may indirectly lead to NMDAR-mediated responses. Further investigation however is required to understand them in the context of NB-mediated potentiation. Regardless of the mechanism, however, our findings reveal an important role of astrocytes in NB-induced cortical plasticity and highlight their role as partners with neurons in restructuring specific circuits that govern stimulus-specific cortical responses.

3.4. Acknowledgments

We are grateful to K.D. McCarthy (UNC) for providing the IP_3R2 mice. We thank Michael Goard, Caroline Runyan, Travis Emery, Jonathan Woodson and Jorge Castro for discussions/technical advice/assistance; This work was supported by an A*STAR Fellowship **(NC),** Marie Curie Fellowship (**GP**), and grants from the NIH (R01EY007023, R01EY018648) and the Simons Foundation (**MS**).

3.5. Figures

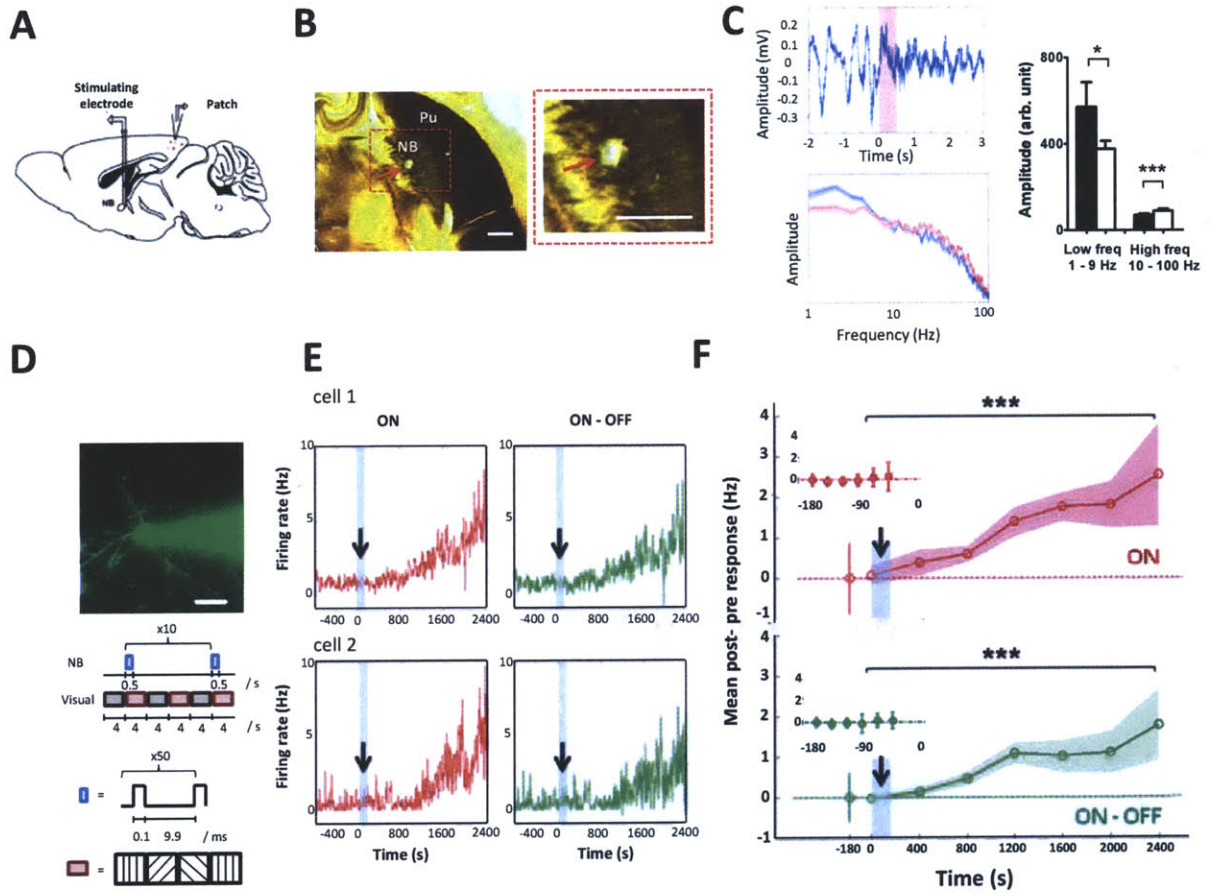

Fig. 1. Paired NB and visual stimulation potentiates visual responses in excitatory neurons *in vivo*. **(A)** Schematic illustration of cell attached recordings from V1 neurons during paired NB and visual stimulation (*50*). **(B)** (***Left***) Localization of the stimulation electrode tract in NB (red arrow), revealed by acetylcholinesterase histochemistry. Pu: Putamen. (***Right***) Magnified view of red box on left. Scale bars, 500 μm. **(C)** (***Top left***) Desynchronization of the interhemispheric EEG signal after NB stimulation at t = 0 s (pink bar). (***Bottom left***) Amplitude-frequency graph 1s before (blue) and after (red) NB stimulation, averaged over 10 trials. (***Right***) NB stimulation induces a decrease in the amplitude of low frequency events ($P<0.05$, n = 9 data sets, paired t-test) and an increase in high frequency events ($P<0.0001$, n = 91 data sets, paired t-test) respectively. EEG desynchronization and/or acetylcholinesterase histochemistry was used to verify NB electrode placement in every experiment. **(D)** (***Top***) Pyramidal neuron electroporated with green Alexa 488 dye by a glass pipette that forms a loose seal with it. (***Bottom***) Schematic illustration of the paired NB and visual stimulation protocol. A visual stimulus (random orientation gratings, pink) was alternately presented with blank gray screen (gray). NB trains (blue) were synchronized with the onset of each visual stimulus, for 10 trials. **(E)** Example neurons showing potentiation of ON and ON – OFF responses with paired NB and visual protocol (blue shades with arrow). **(F)** Mean post-pre response changes (firing rate, Hz) showing potentiation of ON and ON-OFF visual responses in a population of neurons (n = 6 neurons, 6 animals, $P <<< 0.0001$, paired t-test comparing pre-NB to post-NB responses pooled across all the 400s time segments for both ON and ON-OFF responses). Blue shaded bars with arrow indicate NB stimulation period. Color shades around means indicate SEM. The insets show stable baseline responses before NB stimulation. The x-axis labels indicate the start of the time segment analyzed.

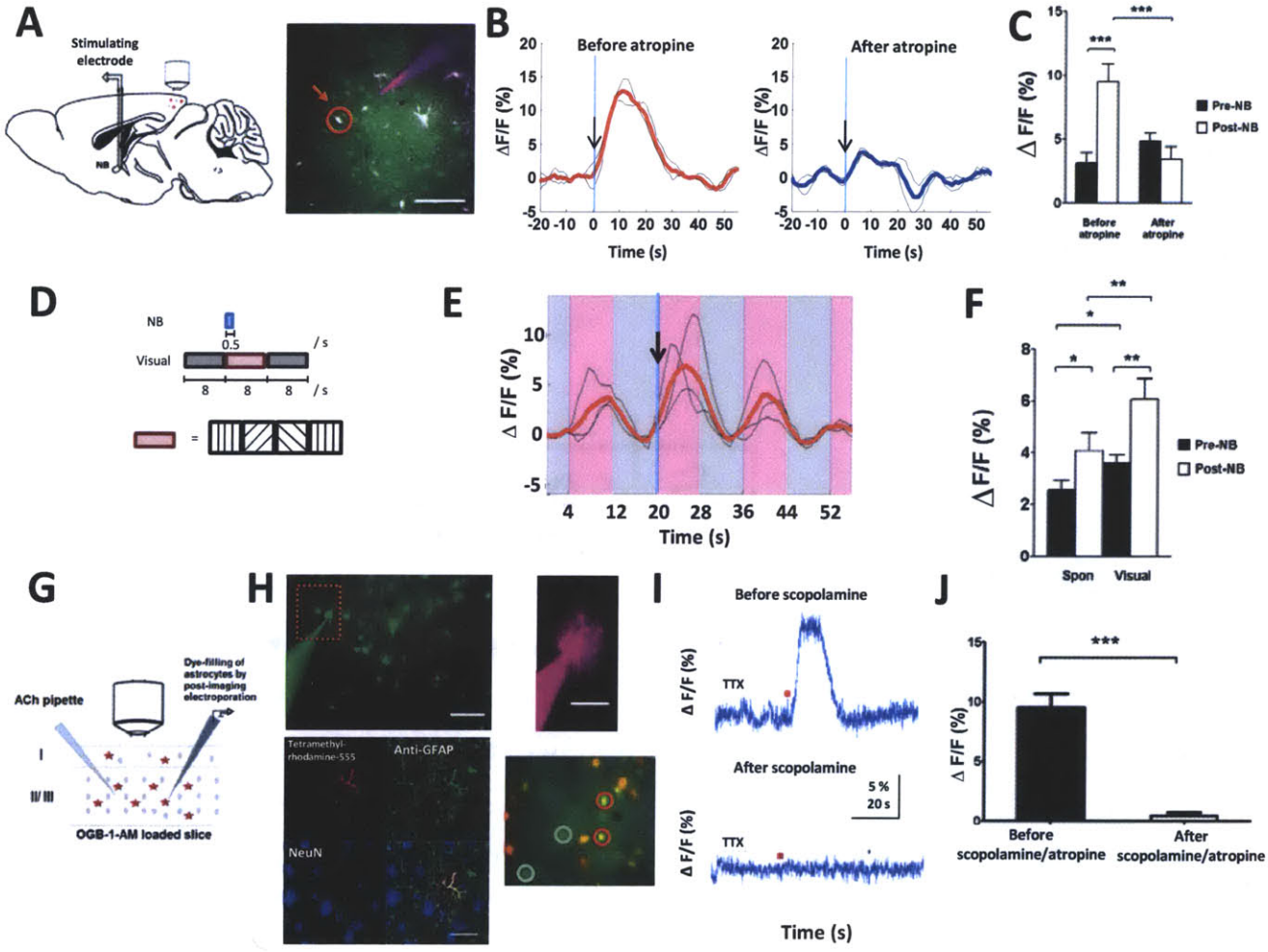

Fig. 2. *In vivo* NB stimulation and ex vivo ACh application directly induces robust calcium responses in visual cortical astrocytes via muscarinic receptors. **(A)** (***Left***) Schematic illustration of the experimental setup for two-photon calcium imaging during NB stimulation. (***Right***) Labeling of cortical astrocytes with OGB1-AM (green) and SR-101 (red) with micropipette for pressure injection of atropine plus Alexa594 to visualize drug spread. An astrocyte used in the analysis is circled red. Scale bar, 50 μm. **(B)** Responses of astrocytes to brief NB stimulation (arrow) before and after the application of atropine. Black lines show example trial-averaged single cell responses computed from 3 NB stimulation repeats; red and blue lines are means of the single cell responses. **(C)** Population averages of NB stimulation-induced calcium responses in astrocytes before and after atropine application. Shown are responses of cells with trial-averaged post-NB responses greater than pre-NB responses (astrocytes: 17/26, n=3 animals). *** denote P<0.001. **(D)** Schematic illustration of the paired NB and visual stimulation protocol used. Random orientation grating stimulus (pink) was alternately presented with blank gray screen (gray) across multiple cycles. A single brief train of NB pulses was synchronized with the onset of one visual stimulus cycle. **(E)** NB stimulation (arrow) facilitates visual responses in astrocytes. Pink/gray bars indicate time segments when visual stimulus and blank gray screen was presented respectively. Black and red lines are computed similarly as Fig. 2B. **(F)** Population average of NB-stimulation induced calcium responses in astrocytes before and after visual stimulation. Shown are n = 47/63 cells (5 animals) with significant visual responses ($p < 0.05$, paired t-test comparing pre-NB responses before and after visual stimulation). * P<0.05; ** P<0.01, paired t-test. **(G)** Schematic illustration of experimental setup for calcium imaging of OGB1-AM loaded layer 2/3 astrocytes in V1 slices. ACh

was pressure-ejected locally and electroporated astrocytes were identified by immunohistochemistry (see SI Materials and Methods: Immunohistochemistry). **(H)** (***Top Left***) Fluorescence image of OGB1-AM loaded astrocytes and neurons, showing electroporation pipette. Scale bar, 50 μm. (***Top Right)*** Tetramethylrhodamine-555 (T-555) dye filled astrocyte. Scale bar, 25 μm. (***Bottom Left***) The astrocyte in (***Top Right***) is demarcated in yellow by extent of T-555 which co-localizes with anti-GFAP but not with NeuN immunohistochemistry. Scale bar, 25 μm. (***Bottom Right***) Merged SR101 (red) and OGB1-AM (green) fluorescence images obtained during simultaneous calcium imaging of OGB1-AM loaded astrocytes (circled red) and neurons (circled green), where the former is co-labeled with SR101. Scale bar, 50 μm. **(I)** ACh (red dot; 50 mM, 0.2-1 s, 20 psi) induces TTX-insensitive calcium transients in astrocytes which are abolished by mAChR antagonist scopolamine (20 μM). **(J)** Population average of ACh-induced calcium responses in astrocytes before/after mAChR antagonists. Responses to scopolamine and atropine are similar and pooled (scopolamine, n= 6 astrocytes; atropine, n = 2 astrocytes; P = 0.0001, paired t-test, 4 slices, 3 animals). Error bars indicate SEM.

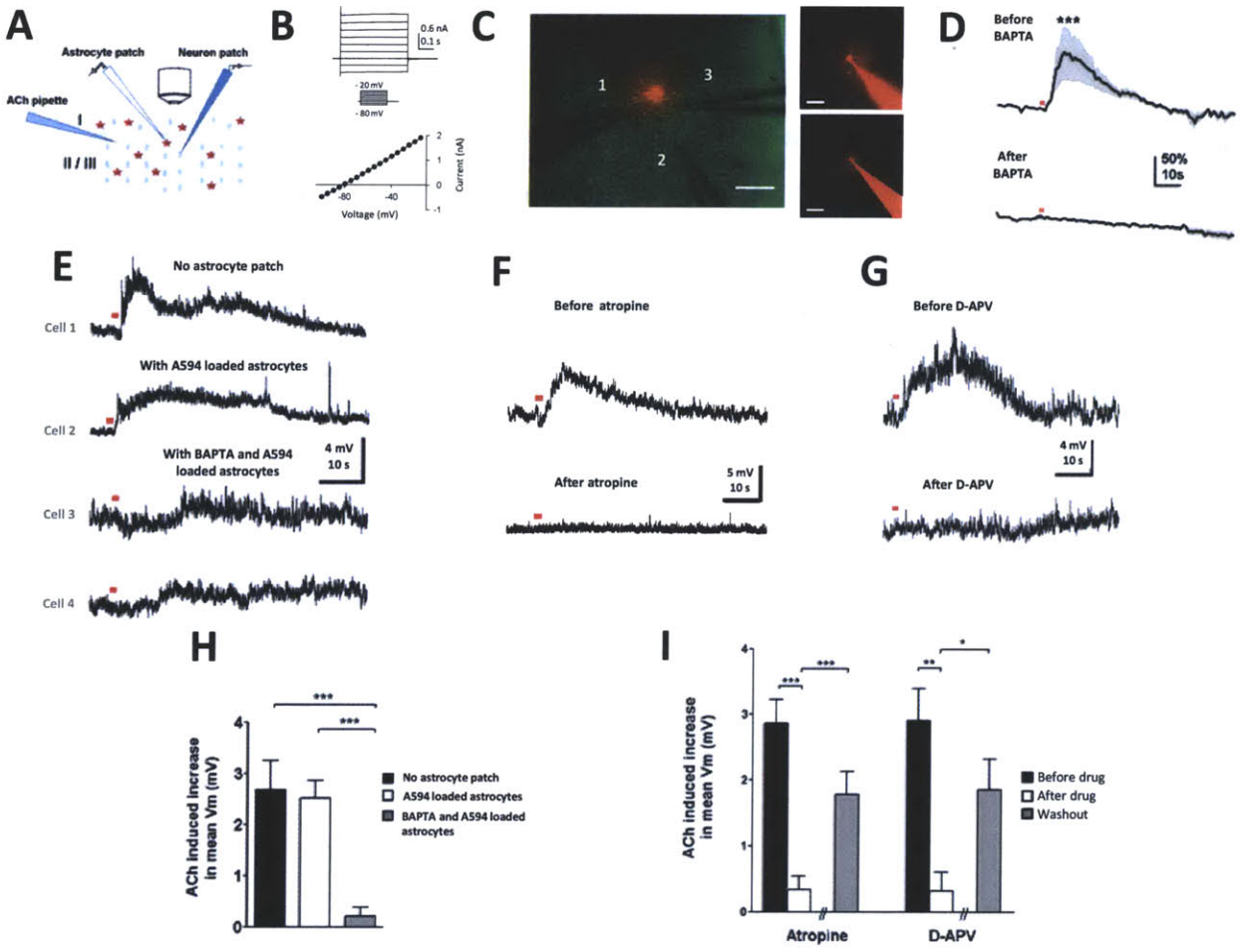

Fig. 3. Cholinergic activation of astrocytes contributes to prolonged depolarizing responses in excitatory neurons *ex vivo*. **(A)** Schematic illustration of slice experimental setup. Calcium responses of layer 2/3 V1 astrocytes were imaged after ACh application (10 mM, 200 ms, 20 psi, unless indicated otherwise), before/after being loaded with Alexa Fluor 594 (A594) and/or calcium chelator BAPTA by whole-cell patch-clamp. Neurons were patched immediately after A594 and/or BAPTA dialysis within astrocyte syncytium. **(B)** ***(Top, bottom)*** Electrophysiological characteristics of an astrocyte, with the I-V curve showing negative resting membrane voltage (V_m) and absence of active membrane currents. **(C)** ***(Left)*** Relative positions of astrocyte patch pipette (1), ACh pipette (2) and neuronal patch pipette (3) as indicated. Scale bar, 100 μm. The range of spacing between ACh and patch pipettes in all experiments was 20 – 100 μm. ***(Right)*** Spread of A594 (and BAPTA) in the syncytium (*bottom,* scale bar 100 μm) within 30-45 min of patching an astrocyte identified by its small round soma with thin radiating processes (*top,* scale bar 25 μm). **(D)** Population averaged calcium responses in astrocytes to ACh application (red dot, 1s, 20 psi) (n = 35 astrocytes, 4 animals) before and after BAPTA loading (50 mM). P <<< 0.0001, paired t-test comparing population averaged responses during 10s post-ACh application before and after BAPTA loading. SEM is represented by shading about the mean. **(E)** Compared to control responses from patch-clamped excitatory neurons recorded without astrocyte patch (cell 1) and with A594 loading of the astrocyte syncytium (cell 2), the amplitude of ACh-induced slow depolarization is reduced in excitatory neurons after BAPTA/A594 dialysis of adjacent astrocytes (cells 3, 4). **(F, G)** Bath-application of atropine (10 – 100 μM) and D-APV (50 μM) drastically reduce the slow depolarization amplitude. **(H)** Population average of ACh-induced increase in mean V_m of: (1) neurons patched without loading astrocytes (n = 9, randomly sampled without replacement from a large pool of 50 neurons), (2) neurons patched after loading astrocytes with A594 (n = 9 neurons, 4 astrocytes, 4 animals), and (3) neurons patched after loading astrocytes with BAPTA and A594 (n = 9 neurons, 8 astrocytes, 6 animals). P > 0.8, P < 0.001 and P <0.0001, t-test comparing (1) and (2), (1) and (3), (2) and (3) respectively. **(I)** Population average of ACh-induced

increase in mean V_m of neurons before/after bath application and washout of atropine (n = 18, n = 8/18 with washout, 13 animals) and D-APV (n = 8, n = 4/8 with washout, 8 animals). The ACh-induced increase in mean V_m was calculated as the difference between mean V_m during 15s pre and post ACh application. * denotes $P<0.05$, ** denotes $P<0.01$, *** denotes $P<0.001$, paired t-test comparing before/after drug and t-test comparing after drug/washout. Error bars indicate SEM.

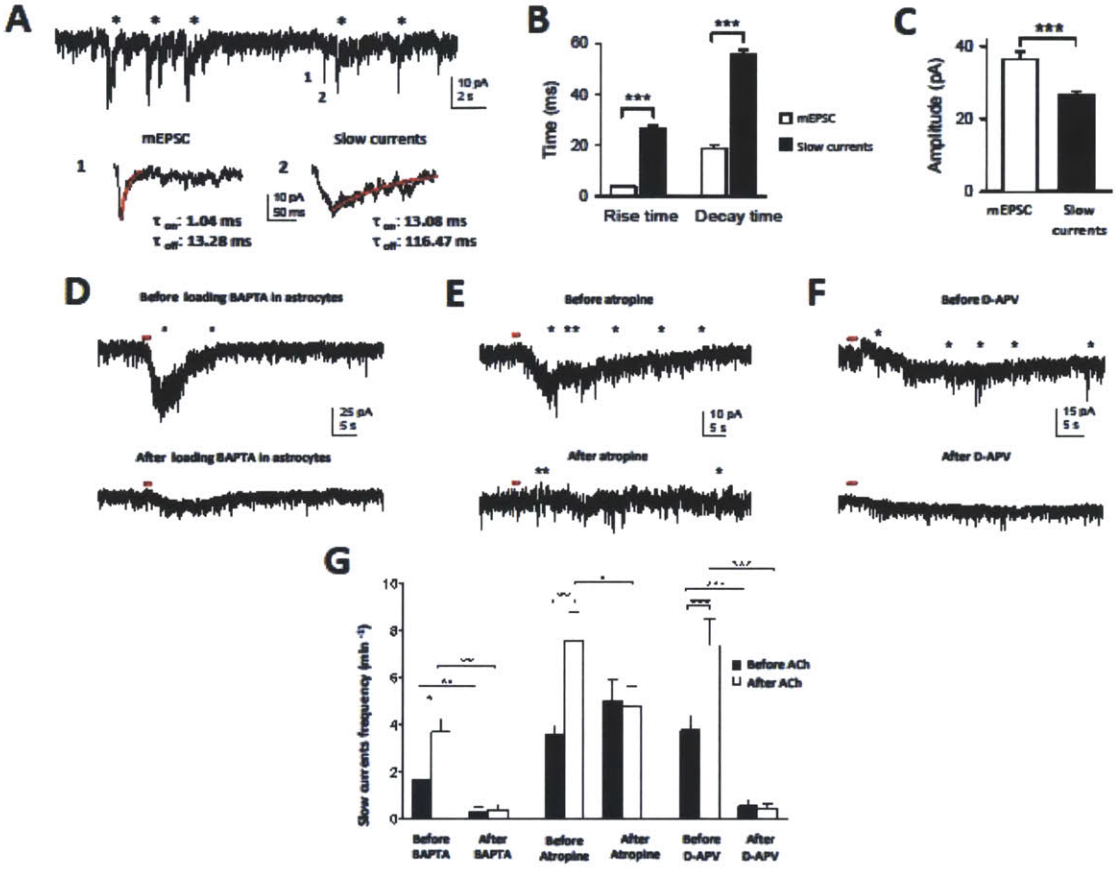

Fig. 4. Cholinergic activation of astrocytes contributes to an increase in TTX-insensitive slow currents in excitatory neurons via calcium-mediated processes that act on neuronal NMDARs. **(A)** Whole-cell neuronal recording where slow currents (labeled with asterisks) were discriminated from miniature EPSCs (mEPSCs) based on their timecourse. Bottom: expanded trace showing the amplitude and time-course of (1) a mEPSC and (2) a slow current event. τ (on and off) refers to the time constants of activation and deactivation (delineated by the red traces). **(B)** Comparison of the mean rise and decay times between mEPSCs and slow currents (rise and decay times: P <<< 0.0001, t-test). **(C)** Comparison of the mean amplitudes between mEPSC and slow current (P <<< 0.0001, t-test). (B) and (C) were computed from 75 events in 15 neurons. Error bars indicate SEM. **(D - F)** ACh induces an increase in the frequency of TTX-insensitive slow currents (labeled with asterisks) in a neuron ***(Top)*** which is reduced after ***(D, Bottom)*** BAPTA dialysis of astrocytes, **(E, *Bottom*)** after bath application of atropine (50uM) and **(F, *Bottom*)** after bath application of D-APV (50 uM). In **(D)**, unlike in Fig. 3, neurons were patched first and their cholinergic responses assessed before and after BAPTA dialysis of astrocytes. **(G)** Population average of TTX-insensitive slow currents before and after ACh application in the following conditions: before/after BAPTA dialysis, before/after atropine and before/after D-APV. * denotes P<0.05, ** denotes P<0.01, *** denotes P<0.001, paired t-test. Error bars indicate SEM.

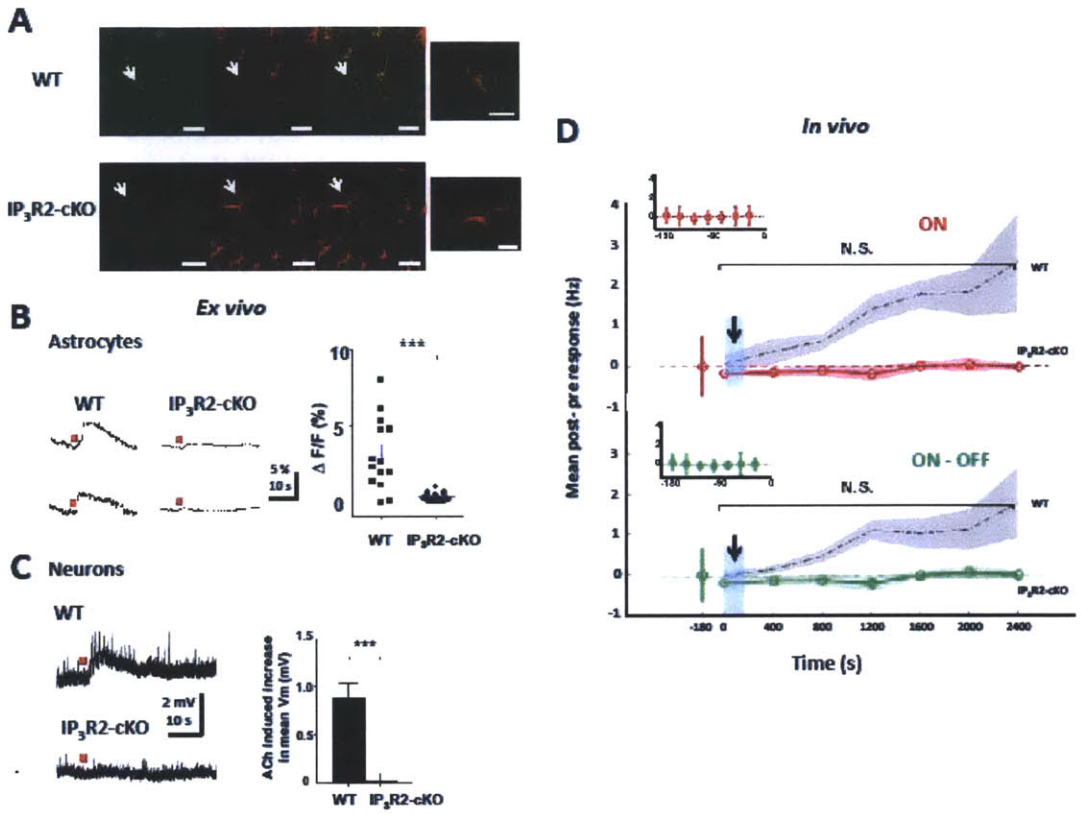

Fig. 5. Deletion of astrocyte IP_3R2 receptors abolishes ACh-induced depolarizing responses in excitatory neurons *ex vivo* and NB-induced potentiation of visual responses *in vivo*. **(A)** Immunohistochemical staining of layer 2/3 cortical astrocytes in (top) WT animals and (bottom) IP_3R2-cKO animals (2 animals each), with (left) anti-IP_3R2, and (middle) anti-GFAP, and showing (right) co-localization of IP_3R2 on astrocytes in WT but not in IP_3R2-cKO animals due to highly reduced IP_3R2 staining in the latter. Image on the right (scale bar, 10 μm) shows a magnified image of the astrocyte marked by arrow in the images on the left (scale bar, 20 μm). **(B)** ***(Left)*** Local ACh application (red dot) evokes calcium responses in astrocytes in WT but not in IP_3R2-cKO adult slices. ***(Right)*** Magnitude of astrocyte calcium responses in WT (n = 14 astrocytes, 2 animals) and IP_3R2-cKO (n = 24 astrocytes, 2 animals). *** denotes $P<0.0001$, t-test. **(C)** ***(Left)*** Local ACh application (red dot) evokes prolonged depolarizing responses in neurons in WT but not in IP_3R2-cKO adult slices. ***(Right)*** Population average of ACh-induced increase in mean V_m of neurons in WT (n = 5 neurons, 2 animals) and IP_3R2-cKO (n = 5 neurons, 2 animals). *** denotes $P < 0.001$, t-test. **(D)** Mean post-pre response changes (firing rate, Hz) in IP_3R2-cKO animals (red and green traces) following multiple pairings of NB stimulation trains with visual stimuli (identical to Fig. 1D), showing absence of facilitation of visual responses (n = 5 neurons, 4 adult animals, $P > 0.1$, paired t-test comparing pre-NB responses to post-NB responses pooled across all 400s time segments for both ON and ON-OFF responses). The black dotted traces with grey shades are WT responses from Fig. 1F. Blue shaded bars with arrow indicate NB stimulation period. Color shades around means indicate SEM. The insets show stable baseline responses before NB stimulation.

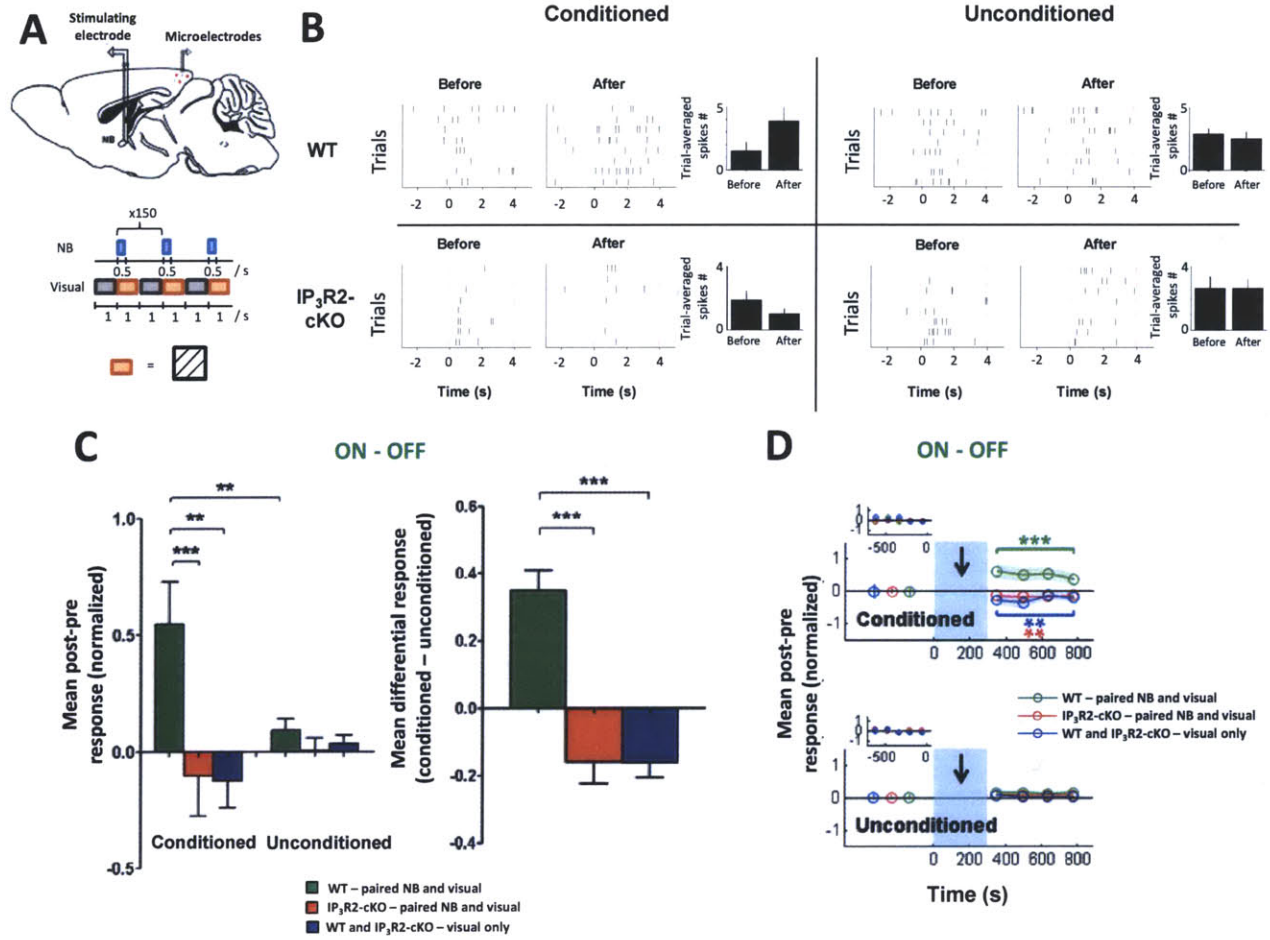

Fig. 6. Cholinergic activation of astrocytes contributes to stimulus-specific potentiation. (A) Schematic illustration of *(Top)* single unit recordings from V1 neurons and (*Bottom*) the protocol used during paired NB and visual stimulation. A visual grating of arbitrary orientation (orange) was alternately presented with a blank gray screen (gray); NB stimulation was synchronized with the onset of the visual stimulus for 150 trials. (B) Raster plots showing example neuronal responses from a WT and an IP_3R2-cKO animal to a conditioned orientation *(left)* and an unconditioned orientation *(right)* before and after the pairing protocol. Presentation of the conditioned orientation was indicated by dotted red lines (0 – 4s). Trial-averaged number of spikes for the example neurons at left is shown in bar graphs at right. (C) *(Left)* Population mean of normalized post-pre, ON-OFF responses at conditioned and unconditioned orientations in WT and IP_3R2-cKO animals, under different protocols. Control (visual only) responses in WT and IP_3R2-cKO animals were similar (Fig. S8E) and are pooled for clarity. See also SI Materials and Methods: Single unit recording; and statistical comparisons in Table S2. *(Right)* Mean differential responses (conditioned - unconditioned orientations). *** denotes P<0.0001, Wilcoxon rank-sum test. Error bars indicate SEM. WT (n=5 animals): paired n = 41 neurons, visual only n = 24 neurons; IP_3R2-cKO (n=4 animals): paired n = 45 neurons, visual only n = 21 neurons. (D) Time course of mean normalized post-pre, ON-OFF responses at conditioned (top) and unconditioned (bottom) orientations. Blue shaded bars with arrow indicate NB stimulation period. The pre-NB baseline responses were averaged over 4 trials and are shown in the insets. Post-pairing responses at the conditioned orientation were significantly enhanced in WT animals (green). Responses were suppressed in the visual only condition (blue, P<0.01) and in IP_3R2-cKO animals after pairing (red, P < 0.01). ** denotes P<0.01, *** denotes P<0.001, Wilcoxon rank-sum test comparing responses before and after NB pairing.

3.6. Methods

C57BL/6 mice and IP_3R2-cKO mice were used for *ex vivo* and *in vivo* experiments at above 2 weeks old and above 6 weeks old respectively. All experiments were performed under protocols approved by the Animal Care and Use Committee, MIT, and conformed to NIH guidelines. For *in vivo* two-photon calcium imaging, cell-attached and single unit experiments, mice were anesthetized with urethane or a fentanyl/midazolam/medetomidine mixture before craniotomy, NB electrode and EEG probe implantation. The NB was stimulated with either a single train or multiple trains of pulses, paired with either presentation of random or single orientation visual gratings. EEG recordings during the experiment, and acetylcholinesterase histochemistry post-experiment, were performed to verify the stereotaxic accuracy of NB stimulation. Slice experiments *ex vivo* were performed for calcium imaging and whole-cell recording. Anti-GFAP, NeuN, anti-mAChR and DAPI immunohistochemistry were performed to verify the identity of astrocytes and localization of mAChRs on them. Student's t-test and Wilcoxon rank-sum test were used for statistical analyses as appropriate. For full details, see **SI Materials and Methods.**

3.7. Supporting Information

3.7.1. Supplementary Methods

Mice

All experiments were performed under protocols approved by the Animal Care and Use Committee at MIT and conformed to NIH guidelines. For *in-vivo* experiments, two-photon calcium imaging, cell-attached recordings and single unit recordings were performed on adult (> 6 weeks old) C57BL/6 and IP_3R2-cKO mice maintained on a C57BL/6 background. For slice experiments, C57BL/6 mice and IP_3R2-cKO mice aged 2 – 3 weeks (for Fig. 3 and 4) and > 6 weeks (for Fig. 5A-C) were used. Adult mice were used in the latter experiments to match the ages of IP_3R2-cKO mice used for *in vivo* experiments. IP_3R2-cKO mice were generated (Ken McCarthy Lab, UNC, Chapel Hill) by (see Fig. S6) (i) backcrossing IP_3R2 flox/flox mice (Black swiss background, Dr. Ju Chen, UCSF) (*51*) to C57BL/6J mice (Jackson Laboratory) for four generations to generate mice heterozygous for the floxed IP_3R2 allele (IP_3R2 flox/+). The IP_3R2 flox/+ mice were screened by PCR for the retinal degeneration gene known to occur in the IP_3R2 flox/flox background strain (*52*) and validated to be absent in these mice. (ii) These mice were crossed to GFAP-Cre recombinase mice on a C57BL/6J background to generate IP_3R2 flox/+ mice with or without Cre-recombinase. (iii) These mice were then interbred to generate mice (iv) homozygous for the floxed IP_3R2 allele (IP_3R2 flox/flox) and heterozygous for Cre-recombinase (IP_3R2-cKO). Mice were genotyped by Transnetyx (Cordova, TN) with real time PCR using genomic DNA and primers specific to Cre-recombinase (CRE), 5' LoxP site of the IP3R2 floxed allele (Itpr2-2 FL) and wild type sequence within the Itpr2 gene that is disrupted by the insertion

of loxP (Itpr2-2 WT). The IP_3R2-cKO mice used in our experiments are positive for CRE and Itpr2-2 FL but negative for Itpr2-2 WT. IP_3R2-cKO mice on the C57BL/6J background were confirmed to have intact visual behavior on a range of visual tests.

***In vivo* surgery**

For the *in vivo* experiments, mice were anesthetized with urethane (1.5 mg/g). In a subset of *in vivo* calcium imaging experiments, a cocktail containing fentanyl (0.05 mg/kg), midazolam (5 mg/kg) and medetomidine (0.5 mg/kg), maintained with 0.2 – 0.5% isoflurane or fentanyl/medetomidine supplements was used. Similar conclusions were derived from data collected from experiments using either of the anesthetics. Ophthalmic ointment was used to protect the animal's eyes during the surgery and replaced with silicon oil during imaging. Body temperature was maintained at 37.5°C with a heating pad. The mice were placed in a stereotaxic apparatus (Kopf Instruments) and bipolar stimulating electrodes were stereotaxically implanted (1.5 mm lateral and 0.5 mm posterior from bregma, 4.5 mm deep from the surface) in the left nucleus basalis (NB). Two silver wire leads were implanted on the brain's surface, over the left frontal cortex and right visual cortex respectively, for EEG recordings (performed with AM systems Model 3000 amplifier and Tektronix TDS 1002 oscilloscope). Desynchronization of the interhemispheric EEG waveform following NB stimulation was used to verify the accuracy of NB electrode implantation in every experiment. A metal headplate was attached to the skull with cyanoacrylate glue and dental acrylic. A 2 x 2 mm craniotomy was made over the primary visual cortex (V1) which was later covered with a thin layer of 2% agarose in ACSF (140 mM NaCl, 5mM KCl, 2 mM $CaCl_2$, 1mM $MgCl_2$, 0.01 mM EDTA, 10 mM HEPES, 10 mM glucose, pH 7.4).

In vivo two-photon calcium imaging

A glass pipette filled with 1.0 mM Oregon Green 488 Bapta-1-AM (OGB1-AM) and 100 μM sulforhodamine101 (SR101, Molecular Probes, Eugene, OR) was visually guided into layer 2/3 using a micromanipulator (Sutter, MP-285) and a small volume was pressure-injected using a Picospritzer. Atropine (500 μM, Sigma) was pressure injected with a pipette containing Alexa Fluor 594 (A594, Molecular Probes, Eugene, OR) for visualization of pipette and drug delivery. *In vivo* imaging of OGB1-AM and SR101 was performed with a two-photon laser scanning microscope (Sutter Instruments, Novato, CA) at excitation wavelength 810 nm. Fluorescence was detected using photomultiplier tubes (R6357; Hamamatsu, Japan). A 25x, 0.95 NA lens (Olympus Optical) was used. Image acquisition was carried out in image planes separated by at least 20 μm using ScanImage software. Imaged cells were located at a depth of 120–200 μm below the pial surface.

In vivo calcium imaging data analysis

Custom-written software in Matlab® (Mathworks, Natick, MA) was used for computation of the time-lapse ΔF/F for each distinct regions of interest (ROIs). Astrocytes were discriminated from neurons by SR101 labeling and their ROIs are manually selected on the OGB1-AM fluorescence image. The raw fluorescence intensity was smoothed with a Gaussian kernel and the change in fluorescence normalized by the baseline fluorescence (ΔF/F) was computed for each ROI. The baseline fluorescence was defined as the average fluorescence across pre-stimulus frames while the change in fluorescence was computed as the baseline fluorescence subtracted from the maximum fluorescence intensity during the stimulus (visual or NB electrical stimulation). Pre- and post-NB responses were computed as described in Fig. S2.

In vivo cell-attached recording

Glass pipettes (1.5 mm tip size, 3–7 MΩ) filled with A594 and held at positive pressure were visually-guided into V1 with a two-photon microscope and directed to 100 - 200 μm below the pial surface (layer 2/3) using a micromanipulator (*28*). The resistance of the pipette was monitored during the penetration by delivering - 0.5 nA current pulses for 6.3 ms at 0.55 Hz with Clampex software (Axon Instruments, v8.1) and Axoclamp-2A amplifier (Axon Instruments). When a seal with a cell during the advancement of pipette was obtained (assessed by increase in pipette tip resistance) and well-isolated spikes were detected on Clampex during visual stimuli presentation, sustained negative pressure was applied (0.2–0.6 psi) to secure the seal (*53*). Recordings were performed at a sampling rate of 30 KHz and filtered between 300 Hz and 10 KHz. The pClamp data was analyzed with Clampfit software v 10.2 (MDS Analytical Technologies) for spike detection and the analyzed data was then imported in Matlab and further analyzed with custom-written scripts to calculate firing rates in epochs with and without visual stimulus presentation.

Single unit recording

Single-unit extracellular recordings were made using tungsten microelectrodes (1.5–2 MΩ, FHC) as described in (*25*). Briefly, the signal was amplified using an 8 channel differential amplifier (FHC), thresholded using an online amplitude discriminator and displayed on an oscilloscope (Tektronix TDS 2022B) and played over an audio monitor (Optimus). Units were isolated from the superficial layers of V1 and amplified (Plexon Neurotechnology Research Systems). Offline analysis to sort waveforms for each unit was performed using commercial programs (Offline Sorter v 2.8.8, Plexon Inc.); post processing was done using in-house code written in Matlab. In

Fig. 6C, 6D, S8, average normalized responses were calculated by first normalizing the responses to the conditioned (or any unconditioned) orientation by the mean of the responses across all orientations excluding conditioned (or any unconditioned) orientation before and after NB stimulation. The normalized pre-NB baseline response was then subtracted from the normalized responses in each post-NB time segment. Only visually responsive units (evaluated using paired t-test, over 8-10 cycles) were used in the analysis. Data points in Figs. 6D, S8C, S8D were computed as sliding window averages of normalized responses.

Nucleus basalis stimulation

The nucleus basalis was stimulated with either a single brief train of 50 pulses (0.1 ms per pulse) at 100 Hz (Fig. 2A-F) or multiple trains of these pulses (Fig. 1D-F, Fig. 5D, Fig. 6) using a stimulator with constant current stimulus isolation unit (S88 Stimulator, Grass Technologies) or PC-driven current isolator (A365, WPI). Visual and NB stimulation were paired by synchronizing the initiation of visual stimulus and output of current isolator through a MATLAB®-driven setup.

Visual Stimulation

Visual stimuli, generated with the Psychophysics toolbox (*54*) in Matlab®, were displayed on a 19 inch LCD monitor situated 15 cm from the eyes. Random orientation gratings were presented in the calcium imaging and cell-attached recording experiments (Fig. 1D-F, 2D-F, 5D) while specific orientation grating were presented in the single unit recording experiments (Fig. 6). The onset of the visual stimulus was synchronized to the initiation of acquisition of two-photon calcium images, cell-attached and single unit spike recordings. The random orientation grating

stimuli consisted of square wave drifting gratings at 100% contrast in 8 randomly-permuted directions, each 45 deg apart and lasting for 450 ms. In the calcium imaging experiments, this stimulus was presented for 8s before alternating with a blank gray screen for 8s across multiple cycles. The duration was shortened to 4s in cell-attached recording experiments. In the single unit stimulus specific plasticity experiments, multiple trials of a set of 9 orientations, each at 4s interval at 20 degrees apart were shown before and after paired nucleus basalis and specific orientation grating stimulation. A blank gray screen was shown for 4s in between each orientation grating. During the pairing, a specific orientation grating, synchronized to the NB stimulation, was presented every 2s.

Acetylcholinesterase histochemistry

At the end of *in vivo* experiments, mice were supplemented with the fentanyl/medetomidine or urethane anesthesia and perfused transcardially with saline followed by chilled 4% paraformaldehyde in 0.1 M PBS. The brains were then postfixed in 4% paraformaldehyde in 0.1 M PBS (<4°C) overnight. The fixed brains were sectioned into 100 μm horizontal slices with a vibratome and stained for acetylcholinesterase: Slices were incubated in 4 mM acetylthiocholine iodide, 4 mM copper sulfate and 16 mM glycine in a 50 mM sodium acetate solution (pH 5.0) overnight and developed in 1% sodium sulfide solution (pH 7.0) for 10 min. Images were captured with an Axiovert 200 microscope with a Sony 3 CCD color video camera.

Slice physiology

Coronal visual cortical sections (300 μm) slices were cut in < 4 °C artificial cerebral spinal fluid (ACSF, with 95% O_2/5% CO_2, pH 7.33 – 7.38) with a vibratome (Leica VT 1200S) and

incubated in ACSF (room temperature) for at least 30 min before being transferred to a slice chamber for patch-recordings. ACSF contained (in mM): NaCl, 127; NaHCO3, 25; KCl, 2.5; NaH2PO4, 1.25; Glucose, 25; MgCl2, 1; CaCl2, 2. For p16 and older animals, the slicing buffer was prepared by altering the ACSF $CaCl_2$ and $MgCl_2$ concentration to 1 and 5 mM respectively to optimize the slice viability. For slice calcium imaging, the slices were preincubated in ACSF containing 1 mM OGB1-AM, 0.4% pluronic F-127 in DMSO and 95% O_2/5% CO_2 for 45 min before they were rinsed in fresh ACSF for 30 min and transferred to the slice chamber. In a subset of the calcium imaging experiments, the slices were incubated for 10 min in slicing buffer containing 1 μM SR101 which preferentially loads astrocytes (*29*) before being transferred to fresh ACSF for 10 min. A solution containing OGB1-AM (344 μM), 1.8% pluronic F-127, 3.87% DMSO in ACSF was pressure puffed to load the calcium indicator in a localized area of astrocytes and neurons. The slices were then incubated in fresh ACSF for 45 min prior to imaging. All experiments were performed in ACSF except for astrocyte-mediated NMDA current experiments (Figure 4) where Mg^{2+}-free ACSF with TTX (1μM) was used. The intracellular pipette solution for patching neurons contained (in mM) Potassium gluconate, 100; KCl, 20; Hepes, 10; MgATP, 4; NaGTP, 0.3; Naphosphocreatine,10 ;295 mOSm, pH 7.4 while that used for patching astrocytes contained (in mM) K-gluconate, 50; ATP, 2; GTP, 0.4; HEPES, 10; 310 – 315 mOsm; pH 7.2 – 7.25. A594 (40 μM) and/or BAPTA (50 mM) were included in this solution in experiments where the spread of A594 and/or BAPTA in the syncytium was quantified. Acetylcholine chloride (ACh), Atropine sulfate (Atropine), Scopolamine hydrobromide (Scopolamine), Tetrodotoxin (TTX) and Adenosine 5′-triphosphate disodium salt hydrate (ATP) were purchased from Sigma; D-(−)-2-amino-5-phosphonopentanoic acid (D-APV), NBQX and 1,2-Bis(2-aminophenoxy)ethane-*N*,*N*,*N*′,*N*′-tetraacetic acid (BAPTA) were

purchased from Tocris. Drugs were bath applied, except for ACh which was applied by pressure injection in specific experiments and BAPTA/A594 which were patch-loaded. In a subset of astrocyte BAPTA/A594 experiments, ATP (20 mM) or ACh (10 mM) was applied by pressure injection at the start of the experiment to check for the health of the slice and viable cellular responses. BAPTA dialysis into astrocytes was only performed in slices that showed astrocyte calcium responses to these agonists. Control experiments for the BAPTA astrocyte dialysis experiments were performed where BAPTA was puffed into the extracellular space while both spontaneous and ACh-induced slow currents were recorded (Fig. S5D).

Analysis of slow currents

To avoid possible controversies regarding the definition of slow inward currents, we used the following criteria in Fig. 4, S5 and Table S1: both the spontaneous and ACh-induced slow currents were discriminated from standard miniature EPSCs (mEPSCs) such that the former had a time-course at least 2 times greater than the latter. These slow currents were similar to the slow inward currents observed in the hippocampus (*12*).

Calcium imaging in slices

Layer 2/3 cells were visualized with a Zeiss Axioskop under an Achroplan 40x water immersion lens, infrared-DIC optics and Streampix 4.20 (Norpix) driven Retiga Exi CCD camera (Qimaging). Fluorescence was continuously excited using a metal halide lamp (EXFO X-cite 120Q). OGB1-AM and SR101 were imaged with blue excitation filter/green emission filter and green excitation filter/red emission filter respectively. Images were continuously acquired at 2.5x or 4x, 10-20 Hz, using 2x2 or 4x4 binning. Images were saved by the Streampix software as

TIFF files and analyzed with custom-written Matlab® scripts. Individual cells were circled manually where astrocytes were discriminated from neurons by their morphology, small soma size and SR101 labeling. The mean fluorescence for each cell was computed from frame to frame, giving a time-varying intensity signal for each cell. After correction for lamp flicker noise and dye photo-bleaching, $\Delta F/F$ was calculated by subtracting the local corresponding baseline (F) from the peak of the response to get ΔF before taking the ratio by F. Increases in $\Delta F/F$ in regions of interest indicated increase in Ca^{2+} concentration.

Immunohistochemistry

For anti-GFAP and NeuN immunohistochemistry after slice calcium imaging experiments (Fig. 2H), the acute slices were fixed with 4% formaldehyde (in PBS) overnight. The fixed slices were then blocked in 10% normal goat serum with 1% triton in PBS (1 hour, room temperature) and stained for rabbit anti-GFAP (1:200, Sigma, G9269) and mouse anti-NeuN (1:250, Millipore, MAB377) overnight (< 4 °C). This was followed by a 3 hour incubation in Alexa Fluor 488 goat anti-rabbit (1:200, Invitrogen, A11034) and Alexa Fluor 405 goat anti-mouse (1:200, Invitrogen, A31553) before being mounted on a glass slide with the Vectashield Hardset mounting media (Vector Labs). The slides were imaged using a confocal microscope (Zeiss LSM 5 Pascal Exciter). For anti-mAChR, anti-GFAP and DAPI immunohistochemistry (Fig. S3A-B), 50 μm fixed slices were prepared (see Acetylcholinesterase histochemistry above). The primary antibodies used were rabbit anti-M1, anti-M2 (1:200, Millipore, AB5164, AB5166) and mouse anti-GFAP (1:400, Sigma, G3893) while the secondary antibodies were Alexa Fluor 488 goat anti-rabbit (1:200, Invitrogen, A11034) and Alexa Fluor 647 goat anti-mouse (1:200, Invitrogen, A21236). The mounting media contained DAPI (H-1500, Vector Labs). For anti-IP_3R2 and anti-

GFAP immunohistochemistry (Fig. 5A), 40 μm fixed slices were prepared. The primary antibodies used were rabbit anti- IP_3R2, (1:20, Millipore, AB3000) and mouse anti-GFAP (1:400, Sigma, G3893) while the secondary antibodies were Alexa Fluor 488 goat anti-rabbit (1:250, Invitrogen, A11034) and Alexa Fluor 633 goat anti-mouse (1:250, Invitrogen, A21236).

Intracellular recording in slices

Glass pipettes (3 – 5 MΩ) were pulled with a Sutter P80 puller (Sutter instruments). Layer 2/3 cells were visualized with a Zeiss Axioplan microscope coupled with an Achroplan 40x water immersion lens, infrared-DIC optics and streampix 4.20 (Norpix) driven infrared Coolsnap cf2 CCD camera (Photometrics). Regular-spiking (RS) excitatory neurons were identified according to the following morphological and electrophysiological characteristics: pyramidal-shaped soma, apical dendrites radially projecting towards the pial and basal dendrites directed downwards and laterally (*55*) and adaptation of spike frequency when stimulated with a constant current (*56*). For BAPTA-experiments, passive astrocytes were identified by their small round soma with thin radiating processes revealed by A594-filling, highly negative membrane potential and passive responses to a series of depolarizing steps. Recordings were performed with an Axopatch 200 amplifier with pClamp software in both the current- and voltage-clamp modes. Analysis was performed with the Clampfit 10.2.0.12 software.

Statistical analyses

Statistical analyses of experiments to assess significance were conducted with two-tailed Student's t-tests. Unpaired t-tests are indicated as t-test in the text. Wilcoxon rank-sum test were used in Fig.6 as the populations are not normally distributed.

3.7.2. Supplementary Figures

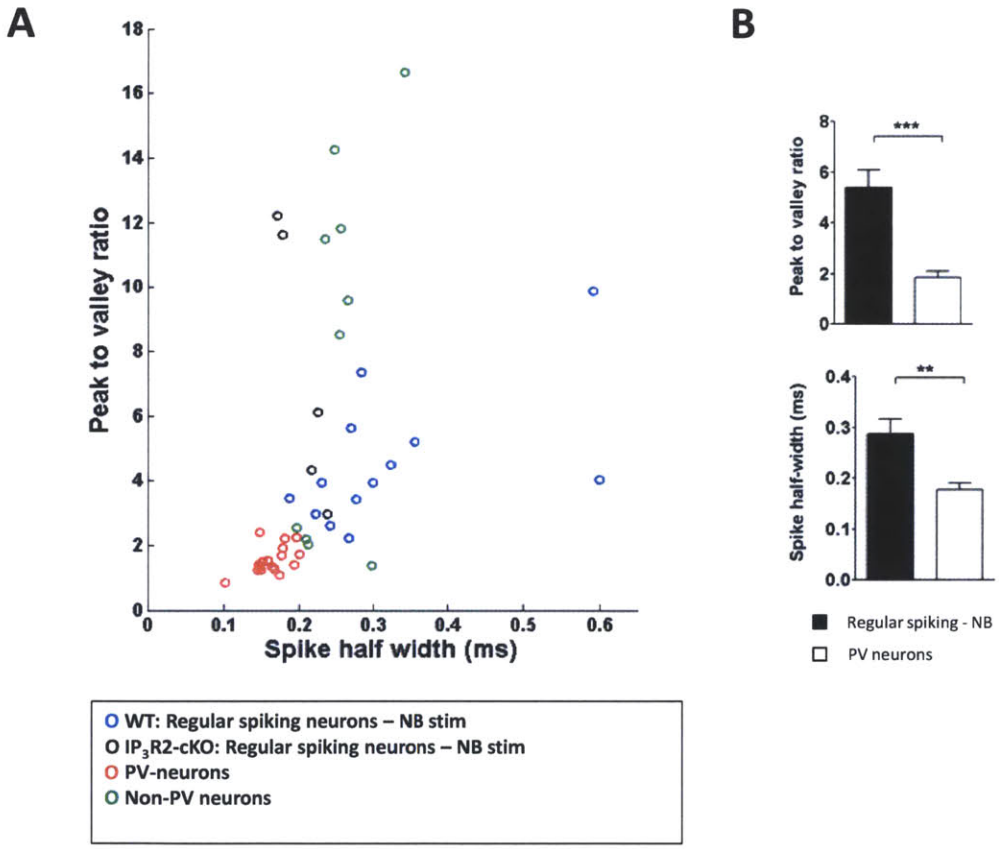

Fig. S1. Electrophysiological properties of neurons studied with cell attached recordings *in vivo* **(A)** Scatter plot of the mean peak to valley ratio of spikes and mean spike half width recorded in individual regular-spiking neurons, and comparison with parvalbumin (PV)-expressing and non PV-expressing neurons studied similarly in PV-Cre mice, where the PV expressing neurons were labeled with RFP (*28*). **(B)** Population average of the mean peak to valley ratio and mean spike half-width in the regular-spiking neurons and PV neurons. ** P<0.001, *** P<0.0001, t-test. Error bars indicate SEM.

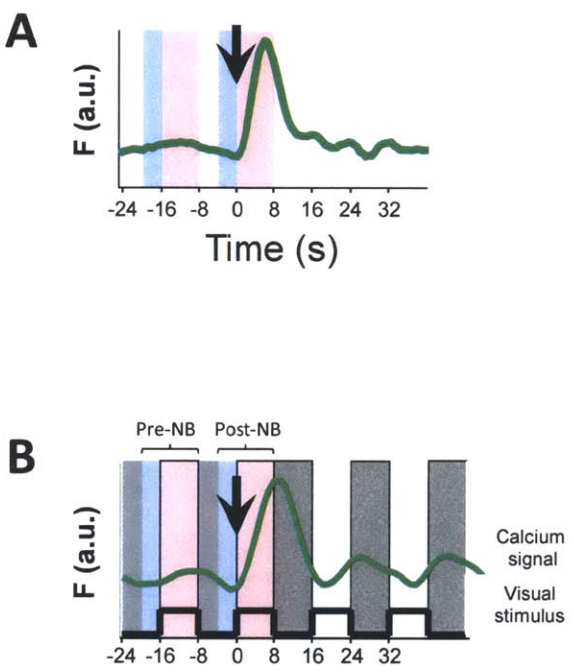

Fig. S2. Schematic showing calculation of post-NB and pre-NB responses, based on time-course of responses in *in vivo* calcium imaging experiments **(A)** without and **(B)** with presentation of visual stimulus. Black line indicates periods where visual stimulation was turned on and off. Pre- and Post-NB responses were calculated in the time windows as indicated using peak fluorescence value (A) in the red time window and mean fluorescence values across timepoints within the blue time window (B) such that Response = (A-B)/B*100. Arrow indicates time point of NB stimulation.

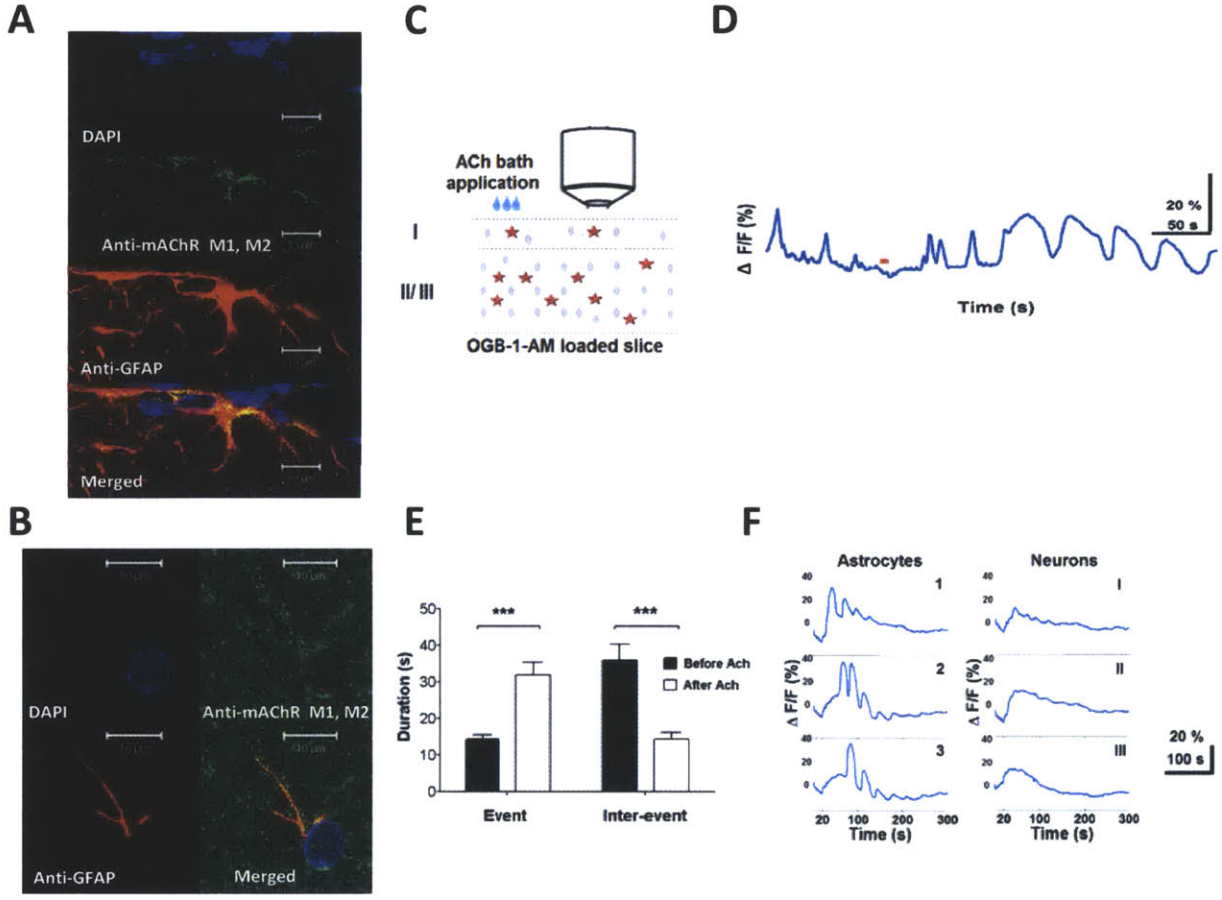

Fig. S3. Triple immunohistochemistry staining of astrocytes with DAPI (nuclear stain), anti-mAChR M1/M2 and anti-GFAP, showing co-localization of muscarinic receptors on astrocytes in **(A)** layer 1, and **(B)** layer 2/3. **(C)** Schematic showing simultaneous imaging of OGB1-AM loaded astrocytes and neurons in layer 2/3 of V1 slices during bath application of ACh (10 mM). ACh concentration remained constant throughout imaging. **(D)** In spontaneously active astrocytes, bath application of ACh induces an increase in frequency and **(E)** duration of spontaneous calcium transients (events) while decreasing the duration between them (inter-events). Events: n = 13 astrocytes, $P<0.001$, paired t-test; Inter-events: n = 12 astrocytes, $P<0.001$, paired t-test. **(F)** ACh induces produces prolonged wave-like calcium increases in simultaneously-imaged astrocytes. A prolonged, slow calcium elevation is evoked in neighboring neurons, simultaneously with the initiation of calcium responses in astrocytes. Time of ACh bath application = 0; responses in this group of cells are initiated about 20s later. The prolonged calcium elevation in neurons resembles the slow depolarization recorded in excitatory neurons by patch clamp.

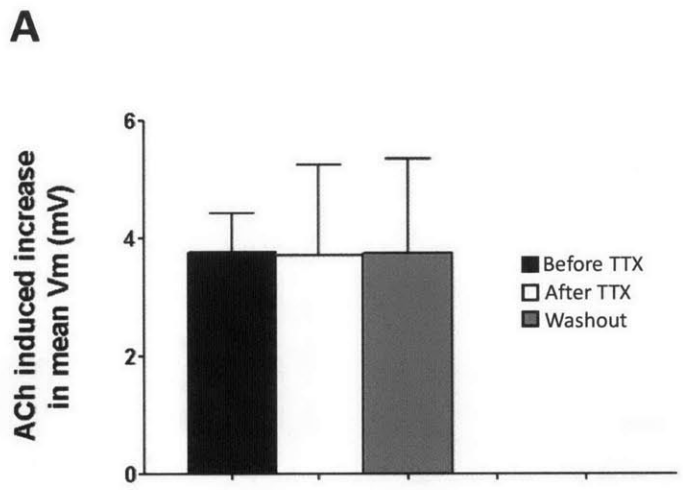

Fig. S4. (A) Population average of ACh-induced increase in mean V_m of neurons before/after bath application and washout of TTX (Before/After TTX: n = 10 neurons, P = 0.976, paired t-test; After TTX/washout: n = 10, n = 4/10 with washout attempted, P = 0.991, t-test, 4 animals).

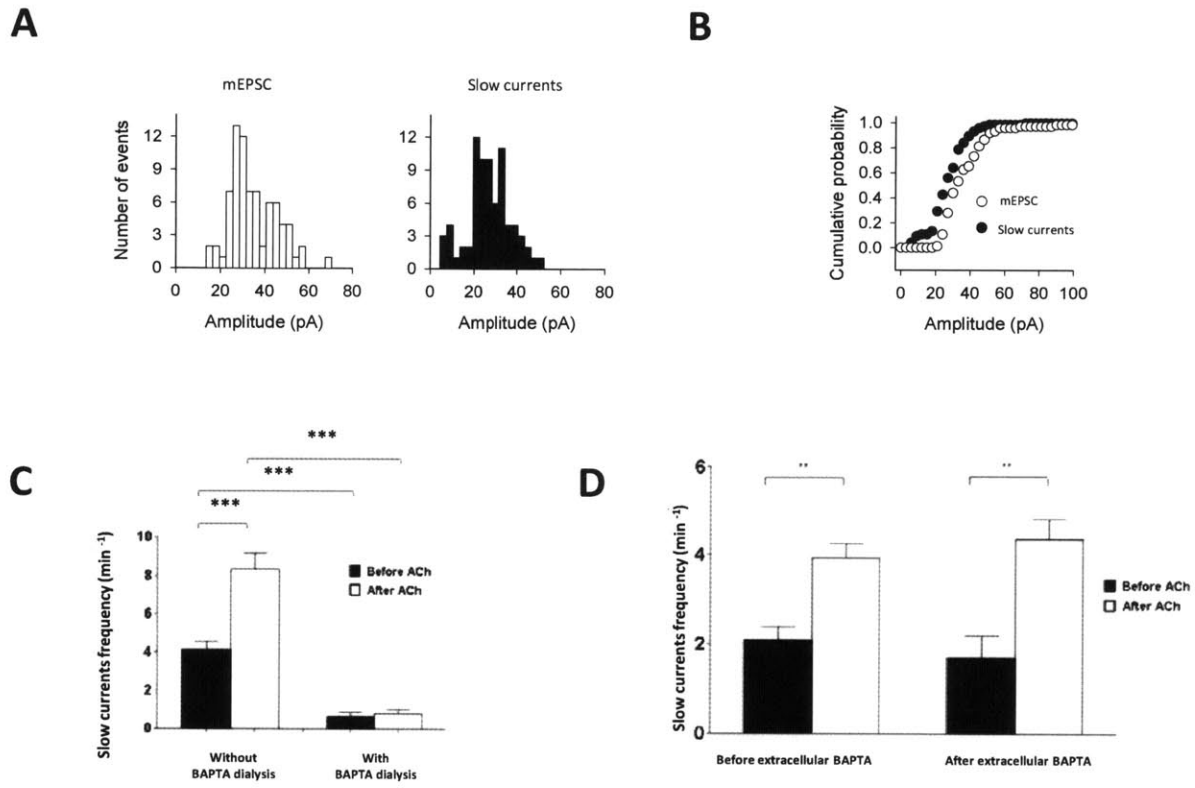

Fig. S5. **(A)** Histograms showing the distributions of mEPSC and slow current amplitudes (bin width = 3 pA). **(B)** Cumulative probability plot of mEPSC and slow current amplitudes from **(A)**. **(C)** Population average of frequency of TTX-insensitive slow currents before and after ACh application in the presence and absence of BAPTA and A594 dialysis of the astrocytes syncytium. In the presence of BAPTA dialysis, the neuronal patch is obtained before and maintained throughout and after BAPTA dialysis (Figure 4D, G) or immediately after BAPTA dialysis. Without BAPTA, Before:After ACh (n = 18, P = 2.43E-06, paired t-test, 9 animals); With BAPTA, Before:After ACh (n = 11, P = 0.143, paired t-test, 8 animals); Before ACh, Without BAPTA:With BAPTA (n = 18, n = 11, P = 3.07E-06 , t-test); After ACh, Without BAPTA:With BAPTA (n = 18 , n = 11, P =1.29E-7, t-test). **(D)** Population average of frequency of TTX-insensitive slow currents evoked by ACh application, before and after extracellular BAPTA puff. Before extracellular BAPTA, Before:After ACh : n = 7 P = 0.0022, paired t-test; After extracellular BAPTA, Before:After ACh : n = 7, n = 6, P = 0.0026, t-test; Before ACh, Before: After extracellular BAPTA: n = 7, P = 0.229, paired t-test; After ACh, Before: After extracellular BAPTA: n = 7, n =6, P = 0.446, t-test, 3 animals.

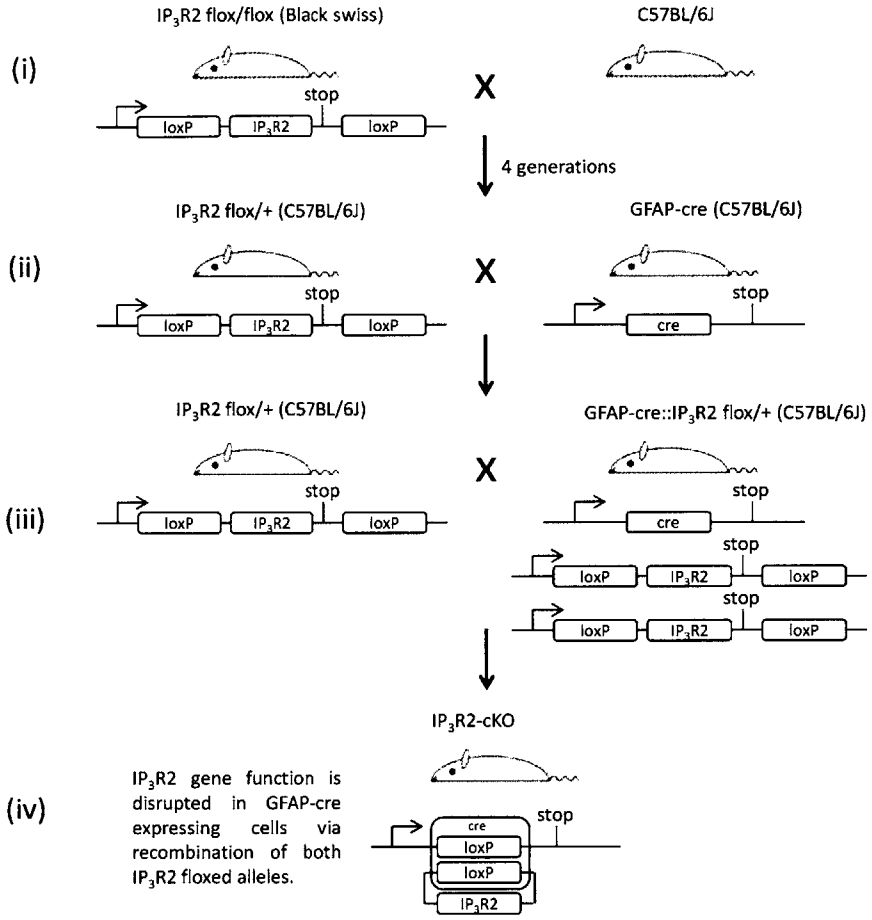

Fig. S6. Schematic diagram that describes the generation of the IP_3R2-cKO mice. See SI Materials and Methods: Mice for further details.

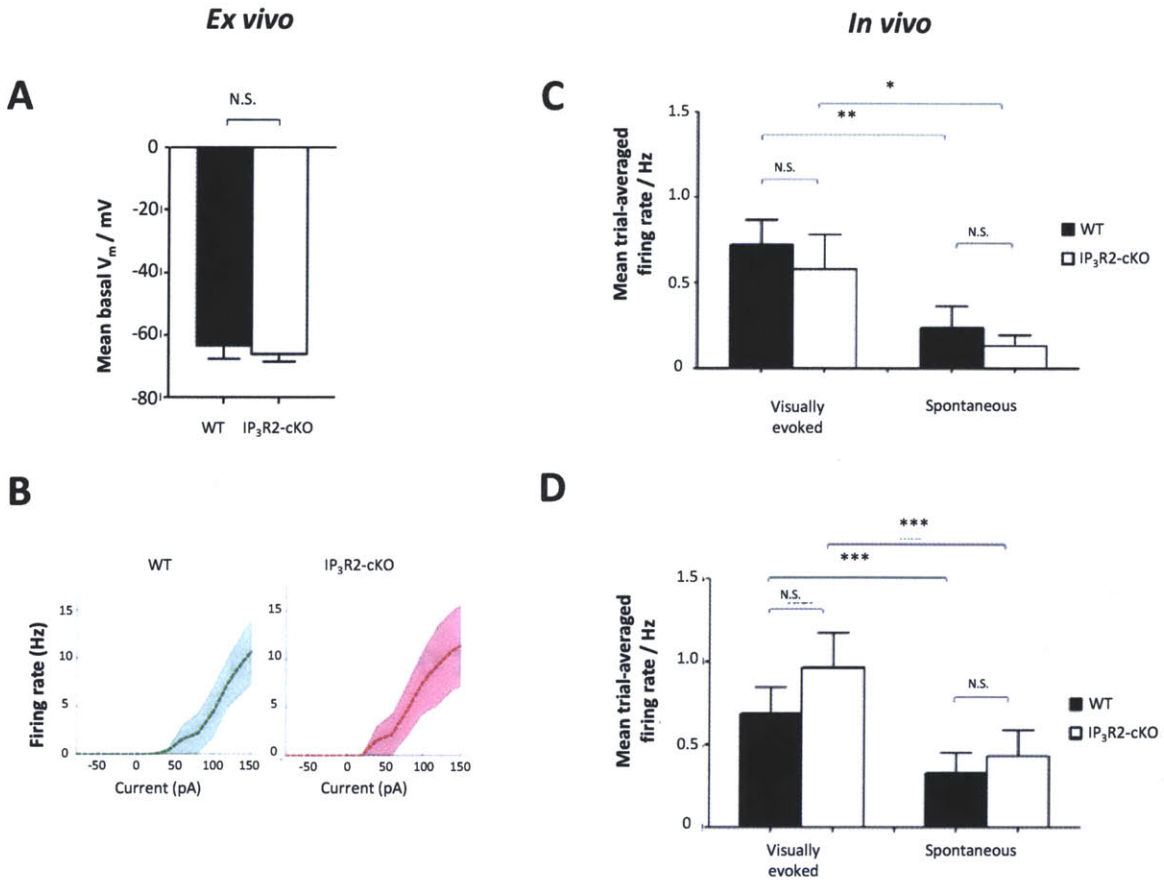

Fig. S7. (A) Mean basal membrane potential (V_m) of neurons recorded in Fig. 5C. P = 0.615, t-test, comparing V_m of WT and IP_3R2-cKO neurons (n = 5 neurons each). **(B)** Mean firing rate-current curve of WT and IP_3R2-cKO neurons recorded in Fig. 5C. **(C)** Mean trial-averaged visually-evoked and spontaneous responses of WT (n = 6 neurons) and IP_3R2-cKO (n = 5 neurons) regular-spiking neurons recorded in Fig. 1E – F, Fig. 5D. P = 0.597, t-test comparing the visually evoked (ON responses) between WT and IP_3R2-cKO; P = 0.476, t-test comparing the spontaneous (OFF responses) between WT and IP_3R2-cKO; P = 0.0028 and P = 0.0460, paired t-test comparing the visually evoked (ON responses) and spontaneous (OFF responses) in WT and IP_3R2-cKO respectively. **(D)** Mean trial-averaged visually-evoked and spontaneous responses of WT (n = 41 neurons) and IP_3R2-cKO (n = 45 neurons) regular-spiking neurons recorded in Fig. 6. P = 0.305, t-test comparing the visually evoked (ON responses) between WT and IP_3R2-cKO; P = 0.593, t-test comparing the spontaneous (OFF responses) between WT and IP_3R2-cKO; P = 0.0002 and P<0.0001, paired t-test comparing the visually evoked (ON responses) and spontaneous (OFF responses) in WT and IP_3R2-cKO respectively.

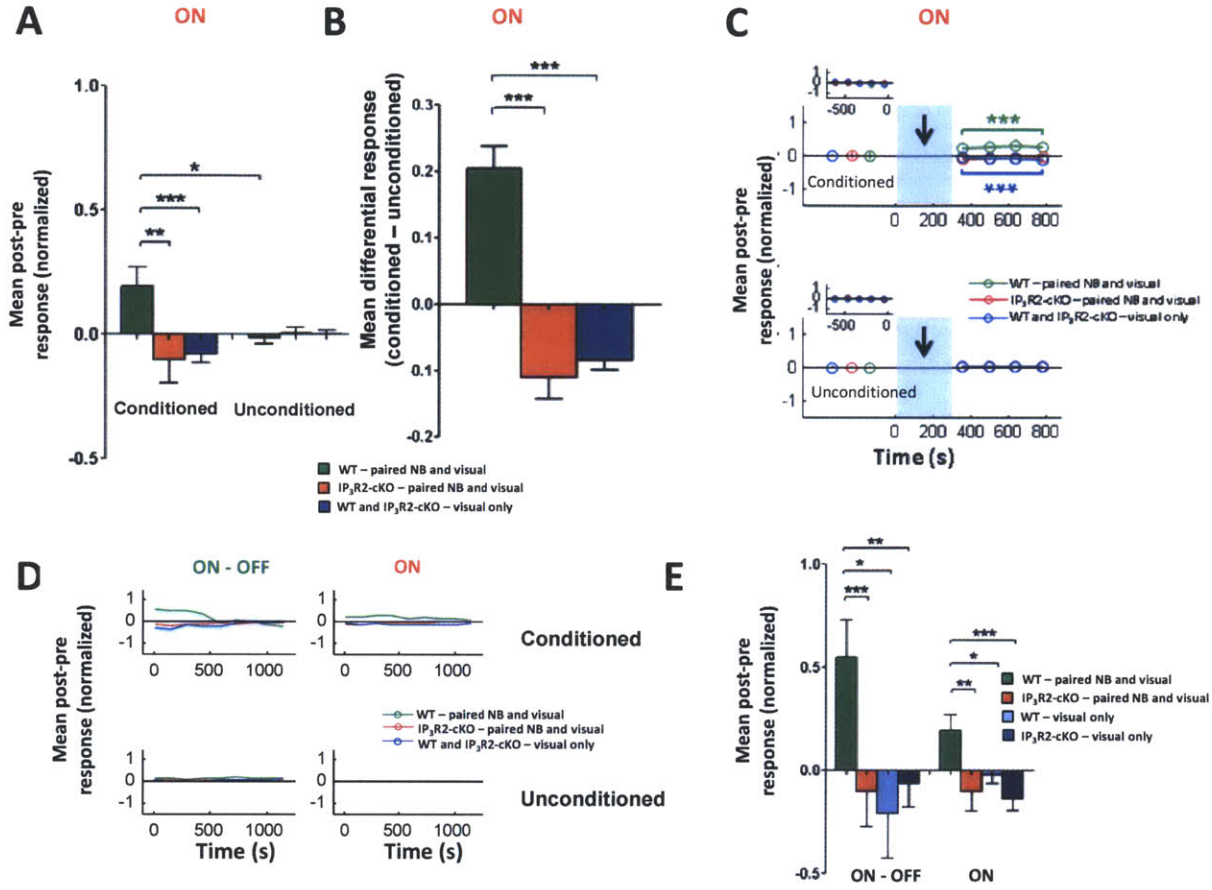

Fig. S8. (A) Population mean of normalized post-pre ON responses at conditioned and unconditioned orientations in WT and IP_3R2-cKO in paired as well as visual only control experiments. **(B)** Mean differential responses (conditioned - unconditioned orientations). *** denotes P<0.001, Wilcoxon rank-sum test. Error bars indicate SEM. **(C)** Time course of mean normalized post-pre, ON responses at conditioned (top) and unconditioned (bottom) orientations. Blue shaded bars with an arrow indicate NB stimulation period. The pre-NB baseline responses were averaged over 4 trials and are shown in the insets. Post-pairing responses at the conditioned orientation were significantly enhanced in WT animals (green). Responses were suppressed in the visual only condition (blue, P < 0.001) and in IP_3R2-cKO animals after pairing (red, P < 0.05). * denotes P <0.05, *** denotes P<0.001, Wilcoxon rank-sum test comparing responses before and after NB pairing. **(D)** Graphs similar to Fig. 6D and Fig. S8C plotted at a longer timescale to show timecourse of recovery of ON and ON-OFF responses. 0 s indicate end of NB stimulation period. **(E)** Population mean of normalized post-pre, ON-OFF and ON responses at conditioned orientations in WT and IP_3R2-cKO animals, under different protocols. See also Fig. 6C, left, SI Materials and Methods: Single unit recording. * denotes P <0.05, ** denotes P<0.01, *** denotes P<0.001, Wilcoxon rank-sum test.

BAPTA

Before BAPTA, Before ACh: After ACh (n = 5, P = 0.0101, paired t-test, 4 animals)
After BAPTA, Before ACh: After ACh (n=5, P = 0.410, paired t-test), 4 animals)
Before ACh, Before:After BAPTA (n = 5, P = 0.0040, paired t-test, 4 animals)
After ACh, Before:After BAPTA (n = 5, P = 0.0059, paired t-test, 4 animals)

Atropine

Before Atropine, Before ACh: After ACh (n = 10, P = 0.0035, paired t-test, 5 animals)
After Atropine, Before ACh: After ACh (n = 10, P = 0.753, paired t-test , 5 animals)
Before ACh, Before:After Atropine (n = 10, P = 0.0797, paired t-test , 5 animals)
After ACh, Before:After Atropine (n = 10, P = 0.0109, paired t-test , 5 animals)

D-APV

Before D-APV, Before ACh: After ACh (n = 10, P = 0.0008, paired t-test , 7 animals)
After D-APV, Before ACh: After ACh (n = 10, P = 0.543, paired t-test, 7 animals)
Before ACh, Before:After D-APV (n = 10, P = 0.0004, paired t-test, 7 animals)
After ACh, Before:After D-APV (n = 10, P = 0.0001, paired t-test, 7 animals)

Table S1. P-values related to Fig. 4G.

	ON	ON-OFF
A_trained : B_trained	0.00220	0.000500
A_trained: C_trained	0.000600	0.00120
A_trained : A_untrained	0.0166	0.00640
B_trained : C_trained	0.422	0.827
B_trained : B_untrained	0.230	0.0563
C_trained : C_untrained	0.0311	0.169
A _untrained: B_untrained	0.813	0.385
A_untrained : C_untrained	0.477	0.248
B_untrained : C_untrained	0.634	0.674

A : WT – NB and visual
B : IP_3R2-cKO – NB and visual
C : WT and IP_3R2-cKO – Visual only

Table S2. P-values related to Fig. 6C, left and Fig. S8A. Wilcoxon rank-sum test was used.

3.8. References

1. C. A. Kitt, C. Höhmann, J. T. Coyle, D. L. Price, Cholinergic innervation of mouse forebrain structures. *The Journal of Comparative Neurology* 341, 117 (1994).
2. J. S. Bakin, N. M. Weinberger, Induction of a physiological memory in the cerebral cortex by stimulation of the nucleus basalis. *Proceedings of the National Academy of Sciences* 93, 11219 (October 1, 1996, 1996).
3. M. P. Kilgard, M. M. Merzenich, Cortical Map Reorganization Enabled by Nucleus Basalis Activity. *Science* 279, 1714 (March 13, 1998, 1998).
4. A. C. Puckett, P. K. Pandya, R. Moucha, W. Dai, M. P. Kilgard, Plasticity in the Rat Posterior Auditory Field Following Nucleus Basalis Stimulation. *Journal of Neurophysiology* 98, 253 (July 1, 2007, 2007).
5. S. Bao, E. F. Chang, J. D. Davis, K. T. Gobeske, M. M. Merzenich, Progressive Degradation and Subsequent Refinement of Acoustic Representations in the Adult Auditory Cortex. *The Journal of Neuroscience* 23, 10765 (November 26, 2003, 2003).
6. R. C. Froemke, M. M. Merzenich, C. E. Schreiner, A synaptic memory trace for cortical receptive field plasticity. *Nature* 450, 425 (2007).
7. D. A. McCormick, D. A. Prince, Mechanisms of action of acetylcholine in the guinea-pig cerebral cortex in vitro. *The Journal of Physiology* 375, 169 (June 1, 1986, 1986).
8. Y. Kawaguchi, Selective Cholinergic Modulation of Cortical GABAergic Cell Subtypes. *Journal of Neurophysiology* 78, 1743 (September 1, 1997, 1997).
9. Z. Xiang, J. R. Huguenard, D. A. Prince, Cholinergic Switching Within Neocortical Inhibitory Networks. *Science* 281, 985 (1998).
10. M. K. Shelton, K. D. McCarthy, Hippocampal Astrocytes Exhibit Ca2+ -Elevating Muscarinic Cholinergic and Histaminergic Receptors In Situ. *Journal of Neurochemistry* 74, 555 (2000).
11. A. Araque, E. D. Martín, G. Perea, J. I. Arellano, W. Buño, Synaptically Released Acetylcholine Evokes Ca2+Elevations in Astrocytes in Hippocampal Slices. *The Journal of Neuroscience* 22, 2443 (April 1, 2002, 2002).
12. G. Perea, A. Araque, Properties of Synaptically Evoked Astrocyte Calcium Signal Reveal Synaptic Information Processing by Astrocytes. *The Journal of Neuroscience* 25, 2192 (March 2, 2005, 2005).
13. Y. Yang *et al.*, Contribution of astrocytes to hippocampal long-term potentiation through release of d-serine. *Proceedings of the National Academy of Sciences* 100, 15194 (December 9, 2003, 2003).
14. G. Perea, A. Araque, Astrocytes Potentiate Transmitter Release at Single Hippocampal Synapses. *Science* 317, 1083 (August 24, 2007, 2007).
15. C. Henneberger, T. Papouin, S. H. R. Oliet, D. A. Rusakov, Long-term potentiation depends on release of d-serine from astrocytes. *Nature* 463, 232 (2010).
16. C. Agulhon, T. A. Fiacco, K. D. McCarthy, Hippocampal Short- and Long-Term Plasticity Are Not Modulated by Astrocyte Ca2+ Signaling. *Science* 327, 1250 (March 5, 2010, 2010).
17. N. Takata *et al.*, Astrocyte Calcium Signaling Transforms Cholinergic Modulation to Cortical Plasticity In Vivo. *The Journal of Neuroscience* 31, 18155 (December 7, 2011, 2011).
18. M. Navarrete *et al.*, Astrocytes Mediate In Vivo Cholinergic-Induced Synaptic Plasticity. *PLoS Biol* 10, e1001259 (2012).
19. A. M. Sillito, J. A. Kemp, Cholinergic modulation of the functional organization of the cat visual cortex. *Brain Research* 289, 143 (1983).

20. P. C. Murphy, A. M. Sillito, Cholinergic enhancement of direction selectivity in the visual cortex of the cat. *Neuroscience* 40, 13 (1991).
21. H. Sato, Y. Hata, H. Masui, T. Tsumoto, A functional role of cholinergic innervation to neurons in the cat visual cortex. *J Neurophysiol* 58, 765 (1987).
22. W. Zinke *et al.*, Cholinergic modulation of response properties and orientation tuning of neurons in primary visual cortex of anaesthetized Marmoset monkeys. *European Journal of Neuroscience* 24, 314 (2006).
23. J. L. Herrero *et al.*, Acetylcholine contributes through muscarinic receptors to attentional modulation in V1. *Nature* 454, 1110 (2008).
24. M. Goard, Y. Dan, Basal forebrain activation enhances cortical coding of natural scenes. *Nat Neurosci* 12, 1444 (2009).
25. V. Dragoi, J. Sharma, M. Sur, Adaptation-Induced Plasticity of Orientation Tuning in Adult Visual Cortex. *Neuron* 28, 287 (2000).
26. J. Schummers, H. Yu, M. Sur, Tuned Responses of Astrocytes and Their Influence on Hemodynamic Signals in the Visual Cortex. *Science* 320, 1638 (2008).
27. G. Buzsaki *et al.*, Nucleus basalis and thalamic control of neocortical activity in the freely moving rat. *The Journal of Neuroscience* 8, 4007 (1988).
28. C. A. Runyan *et al.*, Response Features of Parvalbumin-Expressing Interneurons Suggest Precise Roles for Subtypes of Inhibition in Visual Cortex. *Neuron* 67, 847 (2010).
29. A. Nimmerjahn, F. Kirchhoff, J. N. D. Kerr, F. Helmchen, Sulforhodamine 101 as a specific marker of astroglia in the neocortex in vivo. *Nat Meth* 1, 31 (2004).
30. A. Araque, N. Li, R. T. Doyle, P. G. Haydon, SNARE Protein-Dependent Glutamate Release from Astrocytes. *The Journal of Neuroscience* 20, 666 (January 15, 2000, 2000).
31. P. Bezzi *et al.*, Prostaglandins stimulate calcium-dependent glutamate release in astrocytes. *Nature* 391, 281 (1998).
32. C. M. Anderson, R. A. Swanson, Astrocyte glutamate transport: Review of properties, regulation, and physiological functions. *Glia* 32, 1 (2000).
33. M. A. Di Castro *et al.*, Local Ca2+ detection and modulation of synaptic release by astrocytes. *Nat Neurosci* 14, 1276 (2011).
34. P. Jourdain *et al.*, Glutamate exocytosis from astrocytes controls synaptic strength. *Nat Neurosci* 10, 331 (2007).
35. N. B. Hamilton, D. Attwell, Do astrocytes really exocytose neurotransmitters? *Nat Rev Neurosci* 11, 227 (2010).
36. T. Fellin *et al.*, Neuronal Synchrony Mediated by Astrocytic Glutamate through Activation of Extrasynaptic NMDA Receptors. *Neuron* 43, 729 (2004).
37. G. Rumbaugh, S. Vicini, Distinct Synaptic and Extrasynaptic NMDA Receptors in Developing Cerebellar Granule Neurons. *The Journal of Neuroscience* 19, 10603 (1999).
38. G. Stocca, S. Vicini, Increased contribution of NR2A subunit to synaptic NMDA receptors in developing rat cortical neurons. *The Journal of Physiology* 507, 13 (1998).
39. K. R. Tovar, G. L. Westbrook, The Incorporation of NMDA Receptors with a Distinct Subunit Composition at Nascent Hippocampal Synapses In Vitro. *The Journal of Neuroscience* 19, 4180 (1999).
40. E. Shigetomi, D. N. Bowser, M. V. Sofroniew, B. S. Khakh, Two Forms of Astrocyte Calcium Excitability Have Distinct Effects on NMDA Receptor-Mediated Slow Inward Currents in Pyramidal Neurons. *The Journal of Neuroscience* 28, 6659 (June 25, 2008, 2008).
41. L. A. Holtzclaw, S. Pandhit, D. J. Bare, G. A. Mignery, J. T. Russell, Astrocytes in adult rat brain express type 2 inositol 1,4,5-trisphosphate receptors. *Glia* 39, 69 (2002).

42. J. Petravicz, T. A. Fiacco, K. D. McCarthy, Loss of IP3 Receptor-Dependent Ca2+ Increases in Hippocampal Astrocytes Does Not Affect Baseline CA1 Pyramidal Neuron Synaptic Activity. *The Journal of Neuroscience* 28, 4967 (May 7, 2008, 2008).
43. Q. Zhou, H. W. Tao, M.-m. Poo, Reversal and Stabilization of Synaptic Modifications in a Developing Visual System. *Science* 300, 1953 (June 20, 2003, 2003).
44. H. Jia, N. L. Rochefort, X. Chen, A. Konnerth, Dendritic organization of sensory input to cortical neurons in vivo. *Nature* 464, 1307 (2010).
45. D. Somers, S. Nelson, M. Sur, An emergent model of orientation selectivity in cat visual cortical simple cells. *The Journal of Neuroscience* 15, 5448 (August 1, 1995, 1995).
46. D. Ferster, K. D. Miller, Neural Mechanisms of Orientation Selectivity in the Visual Cortex. *Annual Review of Neuroscience* 23, 441 (2000).
47. J. Schummers, J. Sharma, M. Sur, in *Progress in Brain Research,* R. W. G. V.A. Casagrande, S. M. Sherman, Eds. (Elsevier, 2005), vol. Volume 149, pp. 65-81.
48. M. Benneyworth, Y. Li, A. Basu, V. Bolshakov, J. Coyle, Cell Selective Conditional Null Mutations of Serine Racemase Demonstrate a Predominate Localization in Cortical Glutamatergic Neurons. *Cellular and Molecular Neurobiology*, 1.
49. J. Seigneur, D. Kroeger, D. A. Nita, F. Amzica, Cholinergic Action on Cortical Glial Cells In Vivo. *Cerebral Cortex* 16, 655 (May 2006, 2006).
50. F. K. Paxinos G, *The mouse brain in stereotaxic coordinates*. (New York: Academic Press, 2001), vol. 2nd.
51. X. Li, A. V. Zima, F. Sheikh, L. A. Blatter, J. Chen, Endothelin-1–Induced Arrhythmogenic Ca2+ Signaling Is Abolished in Atrial Myocytes of Inositol-1,4,5-Trisphosphate(IP3)–Receptor Type 2–Deficient Mice. *Circulation Research* 96, 1274 (June 24, 2005, 2005).
52. S. J. Clapcote, N. L. Lazar, A. R. Bechard, G. A. Wood, J. C. Roder, NIH Swiss and Black Swiss Mice Have Retinal Degeneration and Performance Deficits in Cognitive Tests. *Comparative Medicine* 55, 310 (2005).
53. S. Joshi, M. J. Hawken, Loose-patch-juxtacellular recording in vivo--A method for functional characterization and labeling of neurons in macaque V1. *Journal of Neuroscience Methods* 156, 37 (2006).
54. D. H. Brainard, The Psychophysics Toolbox. *Spatial Vision* 10, 433 (1997).
55. J. DeFelipe, I. Fariñas, The pyramidal neuron of the cerebral cortex: Morphological and chemical characteristics of the synaptic inputs. *Progress in Neurobiology* 39, 563 (1992).
56. B. W. Connors, M. J. Gutnick, Intrinsic firing patterns of diverse neocortical neurons. *Trends in Neurosciences* 13, 99 (1990).

Chapter 4: Discussion

4.1. Summary

The research in this thesis sought to understand how ACh can modulate distinct brain functions at a cell-type specific level. Evidence is presented in Chapter 2 and 3 to address the following questions: What are the cortical cell-types involved and how do they interact during cholinergic modulation *in vivo*? Are the roles of ACh-responsive cell-types and their functional interactions preserved across different brain functions? If not, how do their roles and functional interactions change?

In this thesis, we attempt to address these questions in the context of two functions found implicated in cholinergic modulation: information processing and cortical plasticity. It is clear from our findings that different circuits are implicated in these ACh-modulated brain functions. We have found that the cortical inhibitory microcircuit plays a critical role in information processing and alteration of brain states. SOM and PV neurons are the dominant players in this microcircuit and they have opposing influences on PYR neurons. Specifically, the direct facilitation of SOM neurons by ACh leads to both direct inhibition and indirect disinhibition of PV on PYR neurons. The activation of SOM neurons as well as both of these pathways is

important for driving decorrelation between neurons which helps to enhance information processing during cholinergic modulation. Our findings also demonstrate the importance of SOM activation for the ACh-induced alteration of brain states. On the other hand, the induction of cholinergic-modulated stimulus-specific plasticity requires the activation of astrocytes, which can elicit a prolonged facilitatory response in PYR neurons. Based on these findings, it seems that each of the ACh-responsive cell-types have distinct roles across different cholinergic-modulated brain functions.

4.2. Implications

These studies contribute to a growing literature that has elucidated defined functional roles for specific cell types where the selective manipulation of each single cell type in the intact cortical circuitry is possible using optogenetics. Some of these recent studies have shown that PV and/or SOM neurons play important roles in computation (*1-3*), are involved in spatial summation (*4*) and can modulate brain states (*5*). Functional *in vivo* studies on cortical astrocytes using optogenetics has not yet been published although it has been shown that optogenetic activation of astrocytes in the medulla oblongata can contribute to the control of breathing (*6*).

Unlike the above studies, our experiments are performed in a more physiological condition where several distinct cell types are modulated by endogenous release of ACh using optogenetics activation of ChAT-axons or with electrical stimulation of NB. Using optogenetics and knockout mouse models, we were able to elucidate the functional roles of distinct cell types and most importantly their functional interactions during cholinergic modulation of different brain

functions. We have elucidated the functional interactions between several pairs of distinct cell types and have found that the activation of the astrocyte-PYR interaction is sufficient for inducing plasticity while information processing requires more complex activation of SOM-PYR, SOM-PV and PV-PYR interactions. The astrocyte-neuronal interaction seem to occur at a longer time scale than the other neuronal-neuronal interactions, perhaps an explanation to explain why the former modulates the prolonged plasticity while the latter drives the more transient information processing. Knowledge of these interactions revealed from our experimental and computational studies will allow selective manipulation of brain functions in both normal and perhaps for treating diseased brains (e.g. Alzheimer's disease) in the near future.

4.3. Future work

New tools have been made available to allow single cortical cell recording using electrophysiology or two photon calcium imaging in awake, behaving animals (*4, 7-9*). These studies have reported interesting state-dependent differences in the functional properties of single cell types (*8, 9*). It will thus be important to reproduce our work in awake, behaving preparations to understand how the characterized functional roles and their interactions can change. Such experiments will be critical for understanding how cholinergic modulation can facilitate information processing during attentional tasks as well as how attention can alter plasticity during learning (*10, 11*).

One interesting study that is of potential relevance to my thesis work is that on astrocytic modulation of sleep (*12*). My thesis has demonstrated the importance of astrocytes in mediating ACh-induced plasticity while cholinergic output in the cortex has also been shown to vary with both cortical and sleep states (*13*). It is therefore interesting to understand if astrocytes can be involved in sleep modulation through their activation by ACh. In my thesis, I have also demonstrated that a specialized inhibitory microcircuit can induce cortical state changes at a transient timescale. It is therefore also important to understand the mechanisms of how these inhibitory neurons can potentially work with astrocytes at different timescales to modulate brain control of sleep functions.

4.4. References

1. N. R. Wilson, C. A. Runyan, F. L. Wang, M. Sur, Division and subtraction by distinct cortical inhibitory networks in vivo. *Nature* 488, 343 (2012).
2. Bassam V. Atallah, W. Bruns, M. Carandini, M. Scanziani, Parvalbumin-Expressing Interneurons Linearly Transform Cortical Responses to Visual Stimuli. *Neuron* 73, 159 (2012).
3. S.-H. Lee *et al.*, Activation of specific interneurons improves V1 feature selectivity and visual perception. *Nature*, (2012).
4. H. Adesnik, W. Bruns, H. Taniguchi, Z. J. Huang, M. Scanziani, A neural circuit for spatial summation in visual cortex. *Nature* 490, 226 (2012).
5. J. A. Cardin *et al.*, Driving fast-spiking cells induces gamma rhythm and controls sensory responses. *Nature* 459, 663 (2009).
6. A. V. Gourine *et al.*, Astrocytes control breathing through pH-dependent release of ATP. *Science* 329, 571 (2010).
7. C. M. Niell, M. P. Stryker, Modulation of Visual Responses by Behavioral State in Mouse Visual Cortex. *Neuron* 65, 472 (2010).
8. L. J. Gentet *et al.*, Unique functional properties of somatostatin-expressing GABAergic neurons in mouse barrel cortex. *Nature neuroscience* 15, 607 (2012).
9. L. J. Gentet, M. Avermann, F. Matyas, J. F. Staiger, C. C. H. Petersen, Membrane Potential Dynamics of GABAergic Neurons in the Barrel Cortex of Behaving Mice. *Neuron* 65, 422 (2010).
10. J. L. Herrero *et al.*, Acetylcholine contributes through muscarinic receptors to attentional modulation in V1. *Nature* 454, 1110 (2008).
11. D. A. Gutnisky, B. J. Hansen, B. F. Iliescu, V. Dragoi, Attention Alters Visual Plasticity during Exposure-Based Learning. *Current Biology* 19, 555 (2009).
12. M. M. Halassa *et al.*, Astrocytic Modulation of Sleep Homeostasis and Cognitive Consequences of Sleep Loss. *Neuron* 61, 213 (2009).
13. F. Marrosu *et al.*, Microdialysis measurement of cortical and hippocampal acetylcholine release during sleep-wake cycle in freely moving cats. *Brain Research* 671, 329 (1995).